

Transition metal oxide-based electrochromic
materials for energy-saving fenestration and smart
energy storage devices

A thesis

submitted in partial fulfillment of

the requirements for

the Degree of

Doctor of Philosophy

By

Anweshi Dewan

(ID: 20153414)



Department of Physics

Indian Institute of Science Education and Research (IISER),

Pune, India – 411008

*Dedicated to
Baba, Maa and Dida*



भारतीय विज्ञान शिक्षा ँ अनुसंधान संस्थान, पुणे

INDIAN INSTITUTE OF SCIENCE EDUCATION AND RESEARCH (IISER), PUNE

(An Autonomous Institution, Ministry of Human Resource Development, Govt. of India)

Dr. Homi Bhabha Road, Pune – 411 008

CERTIFICATE

This is to certify that the work incorporated in the thesis entitled “[Transition metal oxide-based electrochromic materials for energy-saving fenestration and smart energy storage devices](#)” submitted by Anweshi Dewan has been carried out by the candidate under the supervisions of Dr. Shouvik Datta, Associate Professor, Department of Physics, IISER Pune and Dr. Muhammed Musthafa O. T., Associate Professor, Department of Chemistry and Centre for Energy Science, IISER Pune during the academic year 2015-2022. The work presented here or any part of it has not been included in any other thesis submitted previously for the award of any degree or diploma from any other university or institution.

A blue ink signature of Dr. Muhammed Musthafa O. T.

Signature of Thesis Co-Supervisor
Dr. Muhammed Musthafa O. T.
Associate Professor
Department of Chemistry and
Centre for Energy Science
IISER Pune – 411008

A blue ink signature of Dr. Shouvik Datta.

Signature of Thesis Supervisor
Dr. Shouvik Datta
Associate Professor
Department of Physics
IISER Pune – 411008

Dated: 5th August, 2022



भारतीय विज्ञान शिक्षा ँ अनुसंधान संस्थान, पुणे

INDIAN INSTITUTE OF SCIENCE EDUCATION AND RESEARCH (IISER), PUNE

(An Autonomous Institution, Ministry of Human Resource Development, Govt. of India)

Dr. Homi Bhabha Road, Pune – 411 008

DECLARATION

I hereby declare that the work embodied in the thesis entitled “Transition metal oxide-based electrochromic materials for energy-saving fenestration and smart energy storage devices” represents my ideas in my own words and the experimental results carried out by me and where others’ ideas have been included, I have adequately cited and referenced the original sources. I also declare that I have adhered to all principles of academic honesty and integrity and have not misrepresented or fabricated or falsified any idea/data/fact/source in my submission. I understand that violation of the above will be cause for disciplinary action by the Institute and can also evoke penal action from the sources which have thus not been properly cited or from whom proper permission has not been taken when needed.

Anweshi Dewan

Signature of the student

Mr. Anweshi Dewan

Department of Physics

ID no. – 20153414

IISER Pune – 411008

Dated: 5th August, 2022

Acknowledgement

The most gratifying, but perhaps the most humbling part at the end of the whole process of Ph.D. is to sit down and acknowledge the many debts incurred during the tenure. My words are quite inadequate to explain my gratitude for all of them, who have helped me directly or indirectly during my journey. I must accept that my true acknowledgements are ampler than these few pages.

First and foremost, I must thank my supervisors Dr. Shouvik Datta and Dr. Muhammed Musthafa O. T. for their constant support, insightful suggestions and scholarly criticisms throughout the course of my Ph.D. as well as giving me the full freedom to pursue my research works quite independently. Their enthusiasm, knowledge of science and ethical values will always inspire me for pursuing my future career in science and research. I feel really privileged to get their guidance and undoubtedly I owe a lot to them.

I would also like to pay my sincere gratitude to my RAC member Dr. Nandu. B. Chaurse from the Department of Physics, Savitribai Phule Pune University for his constructive scientific feedbacks and suggestions during my RAC meetings. I want to thank Dr. Remya Narayanan from Department of Environmental Science, Savitribai Phule Pune University for her constant support and valuable scientific inputs to my research from the starting days of my Ph. D.

I would like to convey my deepest regards to our former director Prof. K. N. Ganesh and the current director Prof. Jayant B. Udgaonkar for providing such world-class research infrastructure and outstanding research environments within the institute. I am really thankful to my funding agency DST-INSPIRE for funding me during my Ph.D. tenure. As always at all stages of the work, the help from all the non-teaching staff including Nilesh Sir, Sudhir Sir, Anil Sir, Yathish Sir in terms of technical works and Tushar Sir, Prabhakar Sir, Dhanashree Ma'am, Sayali Ma'am for helping with all administrative procedures, was seemingly great. All the house-keeping staff and technical staff also deserve a big round of thanks for always keeping the research labs in working condition.

I am very much indebted to Sattwick and Soumodip for helping me to clarify different research related issues with constructive criticisms during our numerous verbal exchanges. I would also like to thank my past lab-members, Amit da, Saurabh, Gautam, Deepak, Sumit and present lab-mates, Mohit and Dipti for their support and keeping up the spirit and healthy research atmosphere of the lab.

A big vote of thanks goes to my friends in IISER, who have always complemented my research life by a cheerful environment during the years of my stay in hostel. This is the first and probably the last hostel life during my whole academic journey and it has truly become worth remembering because these people. I specially thank Projjwal, Arijeet, Arnab, Suddha, for being there whenever I felt low and keep on revitalizing me. I am very lucky to have such a nice, supportive and always encouraging senior like Shatruhan bhaiya, I really appreciate his positive attitudes and all his supports during my Ph.D. Rajesh, Prasun, Souptik da, Kartik, Sukanya, Ajith, Imran, Anupam, Anirban da, Nirjhar da, Bani da, Subhendu also deserve a special mention as they also helped me to overcome this long and sometimes tiresome journey in every possible way through their upbeat temperament.

Finally, I cannot convey in words my heartfelt gratitude for my parents for their unstinted support and encouragement to fight all the adversities I faced during my Ph.D. I really owe a lot to them because of their sacrifices and prescient decisions since my childhood. Throughout this journey, I have confronted a lot of difficult situations, which made me a lot more patient and poised and I hope those will inspire me to conquer the upcoming hurdles.

5th August, 2022

Anweshi Dewan

Table of contents

Table of contents

	Thesis Abstract	1-2
	Thesis Synopsis	3-8
Chapter 1	Introduction	9-36
	Abstract	10
1.1	Introduction to smart materials	10
1.2	Types of smart materials	10-11
1.3	Chromogenic and smart glass materials	11-13
1.4	Basic introduction to electrochromism	13-23
1.4.1	History of electrochromism	13-14
1.4.2	Types of electrochromic materials	14
1.4.3	Structure and modes of operation of an electrochromic assembly	14-20
1.4.3.1	Conducting electrodes	15-16
1.4.3.2	Electrolyte layer	16-18
1.4.3.3	Ion storage or counter layer	18
1.4.3.4	Electrochromic layers	18-20
1.4.4	Electrochromism in transition metal oxides	20-22
1.4.5	Application of electrochromic materials	22-23
1.5	Climate change and exigency of alternative energies	23-25
1.5.1	Electrochemical energy storage devices	24-25
1.5.2	Context of smart windows and electrochromic energy storage	25
1.6	Importance of transition metal oxide nanostructures	26
1.7	Aim and scope of the thesis	26-27
1.8	Bibliography	28-36
Chapter 2	Multi-shelled hollow microspheres of NiO for electrochromic smart window	37-53
	Abstract	38
2.1	Introduction	38-39
2.2	Experimental section	39-41
2.2.1	Materials and chemicals	39-40
2.2.2	Synthesis procedure of nickel oxide hollow microspheres	40

Table of contents

2.2.3	Fabrication of electrochromic electrodes	40
2.2.4	Polymer gel electrolyte fabrication	40
2.2.5	Sample characterizations and measurements	40-41
2.3	Results and discussions	42-49
2.3.1	Structure and morphology analysis	42-43
2.3.2	Surface area measurement	43-44
2.3.3	Formation mechanism of NiO multi-shelled hollow microspheres	44
2.3.4	Electrochromic performances	44-47
2.3.5	Electrochemical impedance analysis	47-48
2.3.6	Prototype for electrochromic smart window	48-49
2.4	Conclusion	49
2.5	Bibliography	50-53
Chapter 3	A rechargeable Zn-NiO electrochromic battery	54-78
	Abstract	55
3.1	Introduction	55-56
3.2	Experimental section	56-58
3.2.1	Chemicals and materials	56
3.2.2	Material synthesis	56-57
3.2.3	Preparation of NiO@C films on FTO	57
3.2.4	Sample characterization and measurements	57-58
3.3	Results and discussions	58-74
3.3.1	Structural and morphological characterizations	58-62
3.3.2	Surface area measurements of the samples	62-63
3.3.3	Electrochromic studies	63-66
3.3.4	Scan rate dependent cyclic voltammetry measurement	66-68
3.3.5	Impedance measurements on NiO@C electrodes	68-69
3.3.6	Electrochromic battery measurements	69-74
3.4	Conclusion	74
3.5	Bibliography	75-78
Chapter 4	A multicolored electrochromic asymmetric supercapacitor	79-114
	Abstract	80
4.1	Introduction	80-81

Table of contents

4.2	Experimental section	82-84
4.2.1	Chemicals and materials	82
4.2.2	Material synthesis and electrode fabrication	82-84
4.2.2.1	Synthesis of negative electrode material (V_2O_5)	82
4.2.2.2	Fabrication of V_2O_5 films on FTO	83
4.2.2.3	Synthesis of positive electrode material (PANI)	83
4.2.3	Material characterization and electrochemical measurements	83-84
4.3	Results and discussion	84-108
4.3.1	Negative electrode material (V_2O_5)	84-96
4.3.1.1	Structural and morphological properties	84-87
4.3.1.2	Surface area measurements of the V_2O_5 samples	88
4.3.1.3	Electrochromic studies on V_2O_5 electrodes	89-91
4.3.1.4	Impedance measurement on V_2O_5 electrodes	92-93
4.3.1.5	Scan rate dependent cyclic voltammetry measurement	93-94
4.3.1.6	Electrochromic supercapacitor measurement on V_2O_5 electrode	95-96
4.3.2	Positive electrode material (PANI)	96-101
4.3.2.1	Morphology and material characterization	97-98
4.3.2.2	Electrochemical measurements on PANI electrodes	98-101
4.3.3	Multicolored electrochromic asymmetric supercapacitor	101-108
4.3.3.1	Electrochemical measurements	102-103
4.3.3.2	Spectro-electrochemistry and supercapacitor measurements	103-108
4.4	Conclusion	108-109
4.5	Bibliography	109-114
Chapter 5	Summary and future perspectives	115-119
5.1	Summary	116-117
5.2	Future perspectives	118
5.3	Bibliography	119
	List of publications	120
	Rights and permissions	121

Abstract

Electrochromism is an electrochemical phenomenon where the optical properties of the materials change reversibly and persistently with the externally applied voltages. It has received increasing attention due to its intriguing features and tremendous applications in electronic displays, energy-efficient fenestrations in buildings and smart energy storage devices.[1] In 21st century, with the rising need for energy saving, alternative sources of energy and automated electronic devices with smart features, both smart windows and smart energy storage devices are going to be an indispensable part of future world. Among potential electrochromic materials transition metal oxides (TMOs) have received immense attention from researchers due to their natural abundance and excellent stability. However, they often exhibit poor performance issues such as low optical contrast, low coloration efficiency and slow color switching speeds, majorly due to their inadequate electrical conductivity.[2] Nanostructured TMOs help to overcome these issues to some extent as their high surface to volume ratio can reduce charge diffusion distances.

In commensuration with the recent research works, the main objective of this thesis is to develop TMO nanostructures with significantly improved performance metrics and subsequently integrate these TMO nanostructures to build functional electrochromic smart windows and smart energy storage devices. To start with, anodically coloring NiO is chosen to demonstrate how its electrochromic performance can be boosted by varying its electrochemically accessible surface area. Further, the material is used to fabricate a polymeric gel electrolyte-based prototype device for smart window application.[3] In the next part of the thesis, metal organic framework (MOF) derived carbon embedded porous NiO is synthesized, which is capable of showing better electrochromic performance compared to the prior one. The material is subsequently integrated as a smart positive electrode to construct a rechargeable Zn-NiO electrochromic battery, which demonstrates its state of charge by changing the colour from dark brown (charged) to transparent (discharged).[4] However, the color change, in this case, is monochromatic and in context of the smart energy storage, it is always desirable to have several shades of color to have precise knowledge about the state of charge of energy storage devices. Hence, in the final chapter of this thesis, V₂O₅ is chosen owing to its capability to show both cathodic and anodic coloration. MOF-derived porous V₂O₅ is eventually integrated to a functional multicolored electrochromic asymmetric supercapacitor device with electrochromic polyaniline as the positive electrode.[5]

References

1. R. J. Mortimer, D. R. Rosseinsky, P. M. S. Monk (Eds.), *Electrochromic Materials and Devices*, Wiley-VCH, Weinheim, Germany, 2015.
2. H. Liang, R. Li, C. Li, C. Hou, Y. Li, Q. Zhang, H. Wang, Regulation of carbon content in MOF-derived hierarchical-porous NiO@C films for high-performance electrochromism. *Materials Horizons* 2019, 6 (3), 571-579
3. A. Dewan, S. Haldar, R. Narayanan, Multi-shelled NiO hollow microspheres as bifunctional materials for electrochromic smart window and non-enzymatic glucose sensor. *Journal of Solid State Electrochemistry* 2021, 25 (3), 821-830
4. A. Dewan, S. Sur, R. Narayanan, Musthafa O. T., MOF-Derived Carbon Embedded NiO for an Alkaline Zn–NiO Electrochromic Battery. *ChemElectroChem*, 2022, 9, e202200001
5. A. Dewan, R. Narayanan, M. O. Thotiyl, A multi-chromic supercapacitor of high coloration efficiency integrating a MOF-derived V₂O₅ electrode, *Nanoscale*, 2022, 14, 17372-17384

Synopsis of the dissertation entitled “Transition metal oxide-based electrochromic materials for energy-saving fenestration and smart energy storage devices”

With the rapid development of human race, heedless use of non-renewable energies is causing multiple issues related to pollution, global energy crisis, global warming etc.[1] However, with the rising demand for energy, a promising solution to this problem is to shift towards the use of inexhaustible energy resources such as solar, wind, tidal, geothermal energy etc.[2] Yet, the intermittent availability of these sources often requires energy storage and conversion devices like solar cells, batteries, supercapacitors, fuel cells etc.[3-5] In this scenario, energy saving has also become an indispensable part of modern day life. In developed countries, a major part (20 %-40 %) of the primary energy is expended for interior lighting and air-conditioning in building sectors.[6] Smart windows take a very crucial role in energy saving and have significant potential for abatement of the rising amount of greenhouse gases. Electrochromic smart windows have gained significant attention in this domain as they offer dynamic control over the throughput of sunray and solar heat for building comfort and decoration.[7] Electrochromic devices’ integration with electrochemical energy storage devices paves the path to the fascinating branch of electrochromic energy storage devices, where the modulation of energy storage level of the devices is perceived by the flamboyant changes of their optical states.[8] Electrochromic smart windows with energy storage capability can also serve as back-up power sources in energy-efficient buildings.[9] With modern technological advancement, these devices with smart functionalities will inevitably become an essential part of the futuristic smart electronic devices.[10]

Transitional metal oxides (TMO) have become promising electrode materials for electrochromism and energy storage devices due to their multiple oxidation states, diversity in morphological characteristics, environmentally benign nature, natural abundance, chemical and environmental stability.[11, 12] However, their electrochemical properties are often retarded by poor charge transfer and ion diffusion kinetics.[13] The situation can be substantially improved by using nanostructured TMOs, as they endow TMOs with higher specific surface area and better ion/electron movements by significantly shortening ion diffusion paths.[12] In this context, primary objective of this thesis is to synthesize nanostructures of TMOs (NiO and V₂O₅) with superior electrochemical activities for their applications in electrochromic smart window and smart energy storage devices with an

emphasis on their physical and electrochemical aspects. With this aim, the thesis is divided into the following chapters:

Chapter 1. Introduction: Electrochromic materials are a special type of smart materials, in which the optical properties of the material change reversibly and controllably by the modulation of an external potential. Hence, the start of this chapter briefly addresses different classes of smart materials before plunging into the main topic of discussion. Further, this chapter talks about the archives of this field of ‘electrochromism’. Thereafter, different sections and elements of an electrochromic device have been discussed in detail. Later, the importance of smart windows and electrochromic energy storage devices were reviewed in the context of global energy crisis and technological advancement. Towards the end of the chapter, the aim and scope of the thesis are outlined.

Chapter 2. Multi-shelled hollow microspheres of NiO for electrochromic smart window: This chapter presents the synthesis of NiO multi-shelled hollow microspheres (NiO MS-HMS) by a glucose-based hydrothermal reaction, followed by its use as electrochromic electrodes.

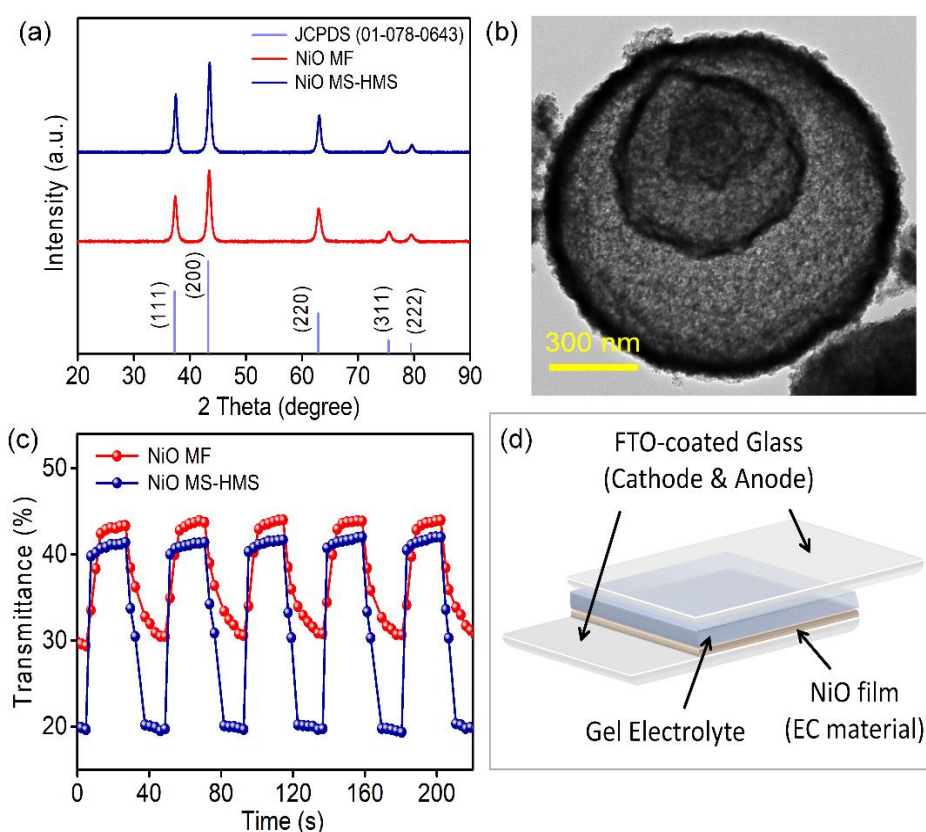


Figure 1: (a) X-ray diffraction patterns of the NiO samples, matched with JCPDS data, (b) Transmission electron microscope (TEM) image showing the existence of multiple shells of NiO MS-HMS, (c) switching time measurement of the samples acquired during in-situ electrochemical UV-Vis spectroelectrochemistry, the experiment was performed using a

LabVIEW-controlled, automated, homebuilt system, (d) Schematic for the prototype of NiO based electrochromic smart window constructed with the aid of polymer-gel electrolyte.

The carbonaceous templates formed from the glucose molecules during the course of the reaction, acted as the templates for the inception of these multiple shells. NiO micro-flakes (NiO MF), synthesized in absence of glucose, offer lesser specific surface area compared to the prior one. Higher specific surface area of NiO MS-HMS improves the interfacial area alongside the charge transfer kinetics leading to superior electrochromic performance. Further, this was utilized to develop a quasi-solid prototype of electrochromic smart window, where KOH-soaked polymer gel was used as the electrolyte. Details of this work can be found in ref [14].

Chapter 3. A rechargeable Zn-NiO electrochromic battery: This chapter explores the synthesis and use of a metal-organic framework (MOF) derived carbon embedded porous NiO as an electrochromic material and later its integration as a positive electrode in a Zn-NiO electrochromic battery. The material functions better in terms of electrochromic performances than NiO MS-HMS, used in the previous work. As the electrodes are cycled in presence of 1 M KOH electrolyte in a three-electrode set-up, there is a reversible switch between the redox couple of Ni^{2+} and Ni^{3+} , which causes the transmission modulation of the electrode.

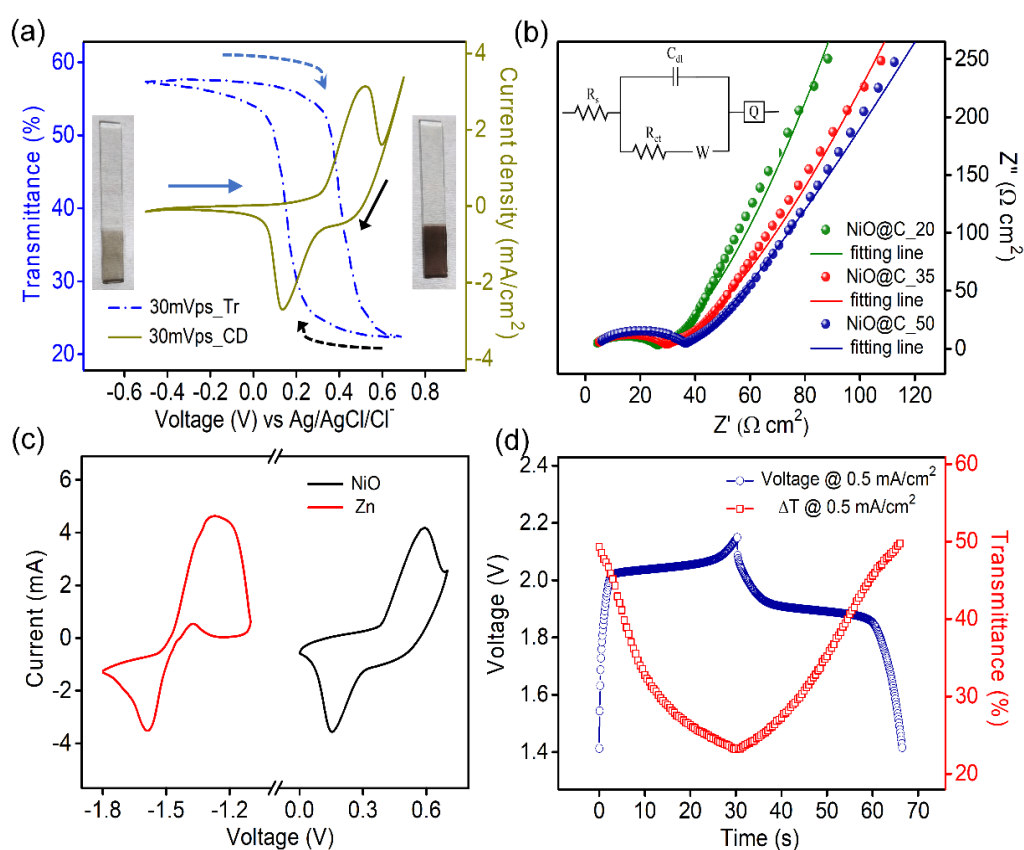


Figure 2: (a) Three-electrode cyclic voltammogram (CV) (solid line) at 30 mVps scan rate along with the in-situ spectro-electrochemistry data (dashed lines) at 525 nm for NiO@C_35 electrode in 1 M KOH electrolyte, (b) EIS study (Nyquist diagrams) for the NiO@C samples and the inset shows the equivalent circuit diagram used for impedance data fitting, (c) CVs showing the stripping and plating of Zn and redox reactions of NiO@C_35 in three-electrode set-up with 1 M KOH + 10 mM ZnAc₂ electrolyte, demonstrating a potential gap of 1.84 V, (d) Galvanostatic charge discharge (GCD) profiles at 0.5 mA/cm² current density and the corresponding change in transmission modulation @525 nm

Depending on the synthesis conditions, three samples were identified and the material with the best electrochromic performance was later integrated into the rechargeable electrochromic battery, alongside a negative Zn electrode. The battery exhibits its state of charge by modulating its optical transparency. It changes from dark brown to colorless as it loses charge. The work can be found with detailed analysis in ref [15].

Chapter 4. A multicolored electrochromic asymmetric supercapacitor: In the previous chapter, a purely monochromatic dynamic change in color of the Zn-NiO electrochromic battery was observed along with the continuous change of its stored energy. However, an electrochromic energy storage device with multiple chromatic states surely offers more control over the intelligent determination of its residual energy.

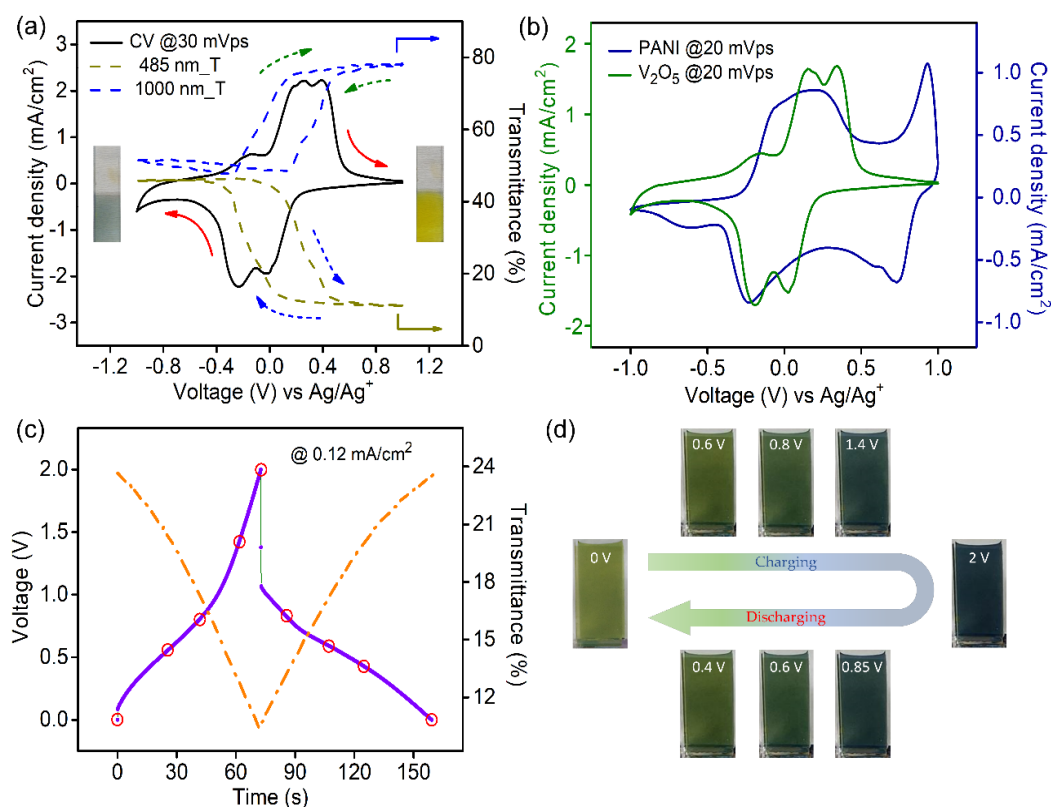


Figure 3: (a) CV data (solid line) of V_2O_5 -1 film at 30 mVps scan rate in 1 M $LiClO_4/PC$ electrolyte along with the in-situ transmission modulation (dashed lines) at 485 nm (dark yellow) and 1000 nm (blue), (b) CV of PANI and V_2O_5 electrodes separately measured in three-electrode set-up in the identical voltage window (± 1 V vs Ag/Ag^+) with 1 M $LiClO_4/PC$ electrolyte at 20 mVps scan rate, (c) GCD profile of MECASC at 0.12 mA/cm² current density and dynamic change in transmission at 580 nm, (d) Photographs of the system at different voltages during charging and discharging as assigned by the red circles in Figure 3c.

Hence, this chapter presents a work based on a multicolored electrochromic asymmetric supercapacitor (MECASC). Primarily, it focuses on the synthesis of a MOF-derived porous V_2O_5 material and its use as an electrochromic material. Later, it illustrates the integration of this material as the negative electrode in the MECASC module, where electrodeposited polyaniline (PANI) electrode was used as the counter electrode. During charging discharging, the device changes back and forth in between its multiple-colored states (yellowish green, dark green, greenish blue, blue and dark blue) and helps to uniquely identify the state of charge of the system.[16]

Chapter 5. Summary and Future perspective: This chapter gives the summary of the whole thesis with an emphasis on the future outlook.

References

- [1] M. Höök, X. Tang, Depletion of fossil fuels and anthropogenic climate change—A review, *Energy Policy*, 52 (2013) 797-809.
- [2] Z. Yang, J. Zhang, M.C.W. Kintner-Meyer, X. Lu, D. Choi, J.P. Lemmon, J. Liu, Electrochemical Energy Storage for Green Grid, *Chem. Rev.*, 111 (2011) 3577-3613.
- [3] M. Winter, R.J. Brodd, What Are Batteries, Fuel Cells, and Supercapacitors?, *Chem. Rev.*, 104 (2004) 4245-4270.
- [4] W. Zuo, R. Li, C. Zhou, Y. Li, J. Xia, J. Liu, Battery-Supercapacitor Hybrid Devices: Recent Progress and Future Prospects, *Adv. Sci.*, 4 (2017) 1600539.
- [5] X. Cao, C. Tan, X. Zhang, W. Zhao, H. Zhang, Solution-Processed Two-Dimensional Metal Dichalcogenide-Based Nanomaterials for Energy Storage and Conversion, *Adv. Mater.*, 28 (2016) 6167-6196.

- [6] N.C. Davy, M. Sezen-Edmonds, J. Gao, X. Lin, A. Liu, N. Yao, A. Kahn, Y.-L. Loo, Pairing of near-ultraviolet solar cells with electrochromic windows for smart management of the solar spectrum, *Nat. Energy*, 2 (2017) 17104.
- [7] C.G. Granqvist, M.A. Arvizu, İ.B. Pehlivan, H.Y. Qu, R.T. Wen, G.A. Niklasson, Electrochromic materials and devices for energy efficiency and human comfort in buildings: A critical review, *Electrochim. Acta*, 259 (2018) 1170-1182.
- [8] Z. Wang, X. Wang, S. Cong, F. Geng, Z. Zhao, Fusing electrochromic technology with other advanced technologies: A new roadmap for future development, *Mater. Sci. Eng. R Rep.*, 140 (2020) 100524.
- [9] G. Cai, P. Darmawan, X. Cheng, P.S. Lee, Inkjet Printed Large Area Multifunctional Smart Windows, *Adv. Energy Mater.*, 7 (2017) 1602598.
- [10] Z. Lu, X. Zhong, X. Liu, J. Wang, X. Diao, Energy storage electrochromic devices in the era of intelligent automation, *Phys. Chem. Chem. Phys.*, 23 (2021) 14126-14145.
- [11] Y. Zhao, X. Li, B. Yan, D. Xiong, D. Li, S. Lawes, X. Sun, Recent Developments and Understanding of Novel Mixed Transition-Metal Oxides as Anodes in Lithium Ion Batteries, *Adv. Energy Mater.*, 6 (2016) 1502175.
- [12] W. Wu, M. Wang, J. Ma, Y. Cao, Y. Deng, Electrochromic Metal Oxides: Recent Progress and Prospect, *Adv. Electron. Mater.*, 4 (2018) 1800185.
- [13] H. Liang, R. Li, C. Li, C. Hou, Y. Li, Q. Zhang, H. Wang, Regulation of carbon content in MOF-derived hierarchical-porous NiO@C films for high-performance electrochromism, *Mater. Horiz.*, 6 (2019) 571-579.
- [14] A. Dewan, S. Haldar, R. Narayanan, Multi-shelled NiO hollow microspheres as bifunctional materials for electrochromic smart window and non-enzymatic glucose sensor, *J. Solid State Electrochem.*, 25 (2021) 821-830.
- [15] A. Dewan, S. Sur, R. Narayanan, M.O. Thotiyl, MOF-Derived Carbon Embedded NiO for an Alkaline Zn–NiO Electrochromic Battery, *ChemElectroChem*, 9 (2022) e202200001.
- [16] A. Dewan, R. Narayanan, M.O. Thotiyl, A multi-chromic supercapacitor of high coloration efficiency integrating a MOF-derived V₂O₅ electrode, *Nanoscale*, 14 (2022) 17372-17384.

Chapter 1

Introduction

- **Abstract**

Smart materials are one particular outcome of the advancement in science and technology. Their response can be engineered in a reversible and controllable way according to our needs. Electrochromic materials come under a particular category of smart materials. This chapter introduces the reader to the term ‘electrochromism’ and its historical research campaigns. Further in this chapter, the structure of the electrochromic devices and different types of electrochromic materials are described in detail, followed by a discussion on the mechanism of transition metal oxides (TMO) based electrochromism and the advantages of using TMOs over other materials as electrochromes. In recent days, with a significant increase in demand for energy; energy saving and storage have become an imperative part of the society. In this context, energy saving electrochromic smart windows and electrochromic energy storage devices have received significant attention from the scientific community. Finally, this chapter narrows down the discussion to the requirement of nanostructured TMOs in electrochemical applications like electrochromism and explores the aim and scope of this thesis.

1.1 Introduction to smart materials

Human evolution is closely interconnected to the manipulation of the environment. Material science utilizes physics, chemistry and engineering as tools to inspect different aspects of individual systems for the discovery and development of new materials. In the 21st century, the progress in modern technologies demands smart and intelligent materials which can change their properties according to our requirements. The properties of the smart materials can be manipulated reversibly and controllably according to the changes in the external stimuli, which may include mechanical stress, pressure, temperature, electric field etc. In the modern era, these materials offer diverse range of applications in various fields.[1]

1.2 Types of smart materials

Smart materials can be classified into two basic categories. The first category includes the materials which undergo reversible changes in their properties (e.g., mechanical, magnetic, chemical, thermal or electrical) as a response to the external stimuli surrounding them, are usually termed as ‘Type 1’ materials. The second category of materials undergoes an energy conversion from one form to another, due to the external perturbations; this class of materials is defined as ‘Type 2’ materials.[2]

Chapter 1

Table 1.1: Different categories of Type 1 smart materials [2]

Type of smart materials	Input	Output
Type 1 Property-changing		
Thermochromic	Temperature difference	Color change
Photochromic	Radiation (Light)	Color change
Mechanochromic	Deformation	Color change
Chemochromic	Chemical concentration	Color change
Gasochromic	Oxidizing or reducing gas	Color change
Electrochromic	Electrical potential difference	Color change
Liquid crystals	Electrical potential difference	Color change
Suspended particle	Electrical potential difference	Color change
Electrorheological	Electrical potential difference	Stiffness/viscosity change
Magnetorheological	Electrical potential difference	Stiffness/viscosity change

Table 1.2: Different categories of Type 2 smart materials [2]

Type of smart materials	Input	Output
Type 2 Energy-exchanging		
Electroluminescent	Electrical potential difference	Light
Photoluminescent	Radiation	Light
Thermoluminescent	Temperature difference	Light
Chemoluminescent	Chemical concentration	Light
Photovoltaic	Radiation (Light)	Electrical potential difference
Type 2 Energy-exchanging (reversible)		
Piezoelectric	Deformation	Electrical potential difference
Pyroelectric	Temperature difference	Electrical potential difference
Thermoelectric	Temperature difference	Electrical potential difference
Magnetostrictive	Magnetic field	Deformation

1.3 Chromogenic and smart glass materials

Chromogenic materials come under the Type 1 smart material category which changes their chromatic states upon exposure to different external perturbants as presented in Table 1. Chromogenic materials are used in mirrors, electronic displays, smart glasses etc. The

Chapter 1

development of chromogenic materials is becoming increasingly important now a days for their applications in wide range of visibly switchable technologies.[3]



Figure 1.1: Typical application of smart glass materials, adapted from ref. [4].

Smart glass or switchable glass (different from the augmented-reality devices worn on our heads which are also called ‘smart glasses’) uses a glazing material that automatically responds to sunlight/temperature or is controlled manually to switch from transparent to opaque or tinted state to regulate the amount of light passes through the glass pane. Depending on the working mechanism, smart glass materials fall into two categories [5] –

(a) Passive smart glass materials – They respond automatically to non-electrical stimuli like ultra-violet (UV) rays (photochromic) or temperature (thermochromic), therefore the optical changes can’t be controlled manually by the user.

(b) Active smart glass materials – These respond to the electrical signals thereby delivering more control to the users. Electrochromic, suspended particle and liquid crystal-based devices come under this category and offer active applications in display screens, window panes etc.

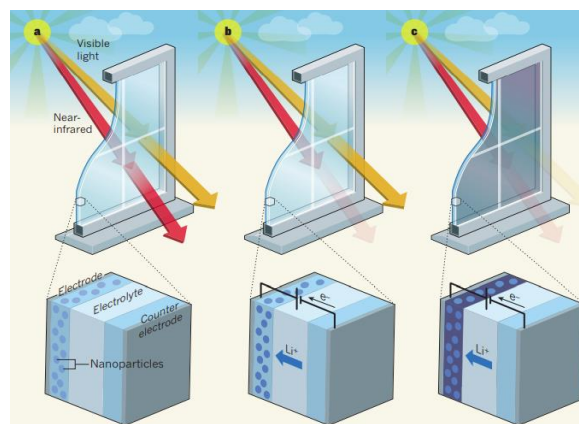


Figure 1.2: Electrochromic smart windows. Upon voltage modulation they controllably and selectively absorb visible and near-infrared radiation. Figure is taken from ref [6].

Compared to passive smart glass materials, the demand for active smart glass materials is always high as the user gets the ability to dynamically control the opacity of the smart glasses according to the requirement. In recent days, Electrochromic materials are the most lucrative and fastest-growing segment among active smart glass materials due to the technological and applicational benefits associated with them. Global electrochromic smart glass market was valued at USD 1.4 billion in 2019 and it is estimated to reach the value of USD 2.6 billion by 2027 at a compound annual growth rate (CAGR) of 9% from 2020-2027.[7]

1.4 Basic introduction to electrochromism

As suggested by the name, these materials change their tint or opacity under the application of potential and thus lend control over the amount of heat and light passing through it. Under the application of voltages, these materials reversibly change their colors using a burst of charge/ions which causes the electrochemical redox reaction in them leading to the change in optical band gap of the material.[8, 9] After reaching a particular level of opacity, electrochromic materials with good optical memory do not require further electricity for maintaining the state.[9, 10]

1.4.1 History of electrochromism

The journey of electrochromism started with tungsten trioxide (WO_3) in 1930, when Kobosew and Nekrassov observed the coloration of WO_3 powders by electrochemical reduction in acidic solution [11] (as cited in ref. [12]). In 1953, an unpublished work by Kraus described the reversible color change of WO_3 film in 0.1 N H_2SO_4 solution.[12] The term “electrochromism” was first coined by Platt in 1961 in his paper, where he observed the electric field-dependent shift in optical spectra for some organic dyes dissolved in organic solvents.[13] Although the electrochromism came to limelight after the seminal works published by S. K. Deb on electrochromism of WO_3 , in 1969 and 1972.[14, 15] Ever since, numerous works have been done by different research groups in different countries. Parallel research was evolving in the Soviet Union and a paper came out in 1974 mentioning an earlier patented work by Malyuk et al in 1963, a work based on niobium oxide films.[16] In mid 1980s, nickel oxide came out to be another important electrochromic oxide.[17, 18] Electrochromic technology was first taken up by big international companies like American Cyanamid Corporation, IBM, Zenith Radio, Canon, RCA, Philips, Brown Boveri etc.[10] for extensive research and further application in information displays. Research in electrochromism got less attention after the rise of liquid crystal displays in late 1970s. But it again rejuvenated, when in 1984

electrochromic oxide materials were widely used in energy-efficient fenestrations, namely smart window technology.[19, 20] Currently, in 21st century the applications of electrochromic technology are not only confined to smart windows or electronic displays, electrochromic films on flexible polymer substrates have advanced their application regime to wearable electronic devices and camouflage attires in defence technology.[21, 22]

1.4.2 Types of electrochromic materials

Electrochromes can be classified into three different families (Type I, Type II and Type III) depending on their physical states upon electrochemical redox reactions. Type I electrochromes remain in electrolyte in soluble form throughout the reaction process and get oxidized at anode or reduced at cathode by an electron transfer reaction to show the color change. Type II electrochromes are soluble in their neutral form, during electron transfer reaction they diffuse towards the electrodes and upon reaction it becomes insoluble and makes colored deposition on electrode surface. Type III electrochromes are insoluble in electrolytes and always remain in solid form throughout the redox process and are usually synthesized or deposited on electrode surface.[23, 24] In this thesis, we have dealt with thin films of TMOs, which come under Type III electrochrome category.

1.4.3 Structure and modes of operation of an electrochromic assembly

An electrochromic device adopts a two-electrode sandwiched structure, consisting of five or more stacked layers. These layers include an electrochromic layer, a counter or ion storage layer, an electrolyte layer sandwiched in between these two layers and two transparent conducting layers on supporting substrates at two extreme ends which serve as the electrical leads.[25] Generally, electrochromic and ion storage layers are mixed conductor type materials that conduct both electrons and ions, the electrolyte is purely an ion conductor and the transparent conducting layers are generally pure electron conductors.[26] In many cases, at the place of ion storage layer another electrochromic material is used.[27, 28] This is the most common configuration of any electrochromic device and it is often called a ‘battery type’ structure.[29] Overall performance of an electrochromic device depends on the selection and the synergistic performances of the constituent components. Usually, in the bleached state of the electrochromic device the ions like Li^+ , OH^- , H^+ reside either in the electrolyte or in the counter electrode layer. When electrical field is switched on, the ions migrate through the electrolyte to reach the electrochromic active layer and the intercalated ions cause Faradaic reaction to change the oxidation state and the optical properties.

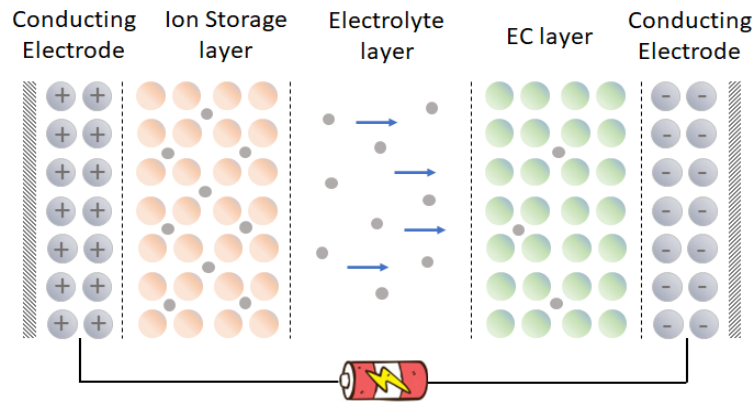


Figure 1.3: Cross-section of a multi-layered electrochromic assembly

Electrochromic devices can operate in two different modes, namely transmission mode and reflection mode. In transmission mode, both the conducting electrodes of the device are transparent and depending upon the opacity of the electrochromic layer, the device dynamically controls the light intensity passing through it. This mode is generally used in smart window applications.[30] Whereas in reflection mode, one of the conducting layers is replaced by a metallic layer like gold, silver, aluminium, platinum or alloys based on platinum or rhodium; which acts as the conducting reflective layer and controls the light intensity.[31] Reflective devices may also have metallic working electrodes with a coating of electrochromic material on top of it, with a transparent conducting electrode working as a counter electrode.[32] This mode is useful for electronic display devices and rear-view mirrors of cars.

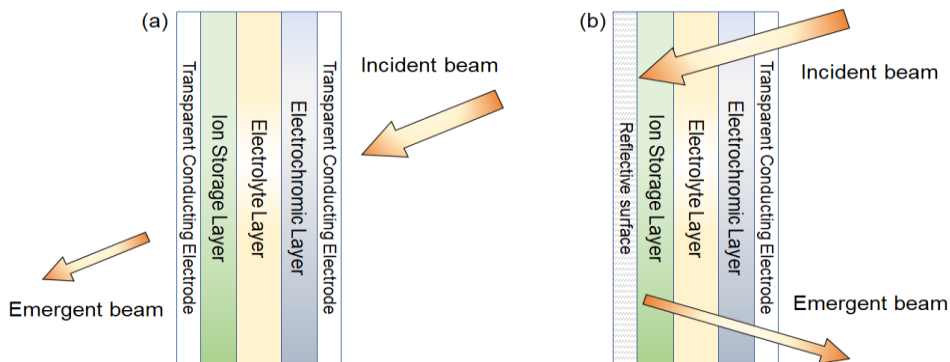


Figure 1.4: Working modes of an electrochromic device (a) transmittance mode, (b) reflection mode

1.4.3.1 Conducting electrodes

These electrodes allow the transfer of electrons during the electrochromic process, usually coated with electrically conducting material on top of a substrate. In reflective type electrochromic devices, the rear conducting electrode is replaced by polished metallic layers as discussed earlier. For transmission type of electrochromic devices, both the electrodes

should be optically transparent across the visible range of the solar spectrum. Usually, glass or flexible polymer materials such as polyethylene terephthalate (PET), polycarbonate, polyimide, polydimethylsiloxane (PDMS) etc. are used as substrates.[24] These substrates are coated with highly doped wide bandgap oxide materials like $\text{In}_2\text{O}_3:\text{Sn}$ (ITO), $\text{In}_2\text{O}_3:\text{Zn}$, $\text{SnO}_2:\text{F}$ (FTO), $\text{SnO}_2:\text{Sb}$, $\text{ZnO}:\text{X}$ (where X stands for Al, Ga, In, Si, B) etc, which are the transparent conducting layers.[26] Many of these oxides can have resistivity as low as 2.5×10^{-4} to $7 \times 10^{-4} \Omega\text{cm}$. [33-35] ITO is a heavily used material in this context due to its wide electrochemical window and high conductivity.

Due to high production costs and health-related concerns of ITO,[36] metal and carbon-based transparent conducting films are being developed. Metals possess nearly two orders higher electrical conductivity compared to conducting metal oxides, which causes the thickness of the metal film to be quite lesser than that of a conducting oxide with similar electrical conductivity, alongwith maintaining the optical transparency. Use of metal films under an electrochromic layer helps to avoid the activation energy barrier between the electrochromic film and the conducting oxide layer.[26] Metal meshes or nanowires of copper, silver on glass or polymer substrate can also give desired performance in terms of electrical conductivity and optical transparency.[37] Carbonaceous materials such as graphene,[38, 39] carbon nanotubes[40, 41] etc. have emerged as very potential candidates as transparent conductors. Apart from their high transparency in the visible and infrared region, and electrical conductivity, these materials are very light-weight and stretchable, which make them suitable for applications in flexible devices.

Among other alternatives, transparent organic conducting polymers like poly(3,4-ethylenedioxythiophene)-poly(styrene sulfonate) (PEDOT:PSS) are available there which can be produced at very low cost and show high electrical conductivity, flexibility and transparency; but in terms of stability these can't match the materials described earlier.[42]

1.4.3.2 Electrolyte layer

Electrolyte plays the role of the ion source and acts as the ion conductor in electrochemical systems. It is insulating for the passage of electrons to avoid short circuits. To get optimized performance from an electrochromic device, the choice of the electrolyte should depend on different key factors like viscosity, working potential window, ionic conductivity, volatility, stability etc. and the electrolyte should be optically transparent.[43, 44] Generally, electrolytes can be in solid, liquid or gel forms and can be categorized into four different classes

– liquid electrolytes, ceramic electrolytes, polymer electrolytes and inorganic solid electrolytes.[45-49]

Liquid electrolytes are produced by dissolving different alkali metal salts like lithium perchlorate (LiClO_4), sodium sulfate (Na_2SO_4), lithium hexafluorophosphate (LiPF_6), zinc chloride (ZnCl_2) in aqueous medium or in polar organic solvents.[50-53] Some well-known organic solvents are dimethylformamide (DMF), propylene carbonate (PC), acetonitrile (ACN) etc. Acidic and alkaline electrolytes are also used as liquid electrolytes.[54, 55] Although, low viscosity of the liquid electrolytes provides very high ionic conductivity which significantly improves electrochromic performances, these face major hindrances in commercial world because of their messy handling, leakage issues etc.

Inorganic solid electrolytes like doped lithium borate (LiBO_2), doped and undoped lithium niobate (LiNbO_3), lithium phosphorous oxynitride (LiPON) etc are mechanically more robust, stable compared to liquid electrolytes and accomplish the role of protective layer in electrochromic devices.[56-58] But ionic mobility and flexibility are the main issues in these electrolytes.

Currently, polymer-based electrolytes are getting more attention because of their prolonged open circuit memory, flexibility and uniform color transitions. Polymer-based electrolytes can be classified into four types – gel or semi-solid polymer electrolytes, solid polymer electrolytes, polyelectrolytes and composite polymer electrolytes. Solid polymer electrolytes are salts e.g., LiClO_4 , LiPF_4 , LiPF_6 etc. dissolved in polar viscoelastic polymer matrices. Most common polymer hosts, used in electrochromic devices are poly(methyl methacrylate) (PMMA), poly(vinylidene fluoride) (PVDF), polyethylene oxide (PEO) etc.[43] In gel polymer electrolytes, some solvents or plasticizers such as propylene carbonate (PC), diethyl carbonate (DEC), ethylene carbonate (EC), dimethyl carbonate (DMC) etc. are incorporated within these polymer matrices for increasing the ionic conductivity by dissociating of the added salts.[24, 48] Overall, polymer gel electrolytes are of great interest as it provides a decent ionic conductivity as well as better flexibility to the system. Polyelectrolytes are different from solid and gel polymer electrolytes. These are polymers with their polymeric backbones covalently bonded with functional groups that carry ionic entities. Polyelectrolytes and polymer electrolytes are different in their ion mobilities. In polyelectrolytes, anions are attached to the polymer backbone, so ionic results only due to cationic mobility. Whereas, in polymer electrolytes both cations and anions are mobile.[44] A

few common polyelectrolytes are polystyrene sulfonate and polyacrylic acids.[24] Composite polymer electrolytes are prepared by adding ionic liquids or inorganic oxides to polymer gel electrolytes, which enhance the electrochemical properties and mechanical stabilities of the gel electrolyte.[59]

1.4.3.3 Ion storage or counter layer

Ion storage layer in electrochromic devices does the charge balancing while the oxidation or reduction reactions occur at the working electrode. There are certain conditions for the choice of an ion storage layer. Firstly, if the counter electrode layer of an electrochromic device is a second electrochrome, it should work in the complementary regime in terms of color change of that of the electrochromic layer and the second is that the counter layer's charge capacity should match that of the electrochromic layer. Different metal oxides, conducting polymers, viologens or redox active materials are used in the counter electrode as an ion storage layer. Use of an appropriate counter layer helps to maintain the performance of an electrochromic device.[60]

1.4.3.4 Electrochromic layers

An electrochromic layer changes its optical properties during redox processes, accordingly we get to see its effects in device applications. In an electrochromic device, electrochromic layers can be integrated as both working and counter electrodes. The electrochromic layer with stronger coloration between them is named as primary electrochrome and the other one is called as secondary electrochrome. Depending on coloration process, electrochromic materials can be classified into two types, they are as follows –

- (i) *Anodically coloring* - Anodically coloring materials such as nickel oxide (NiO), Prussian blue (PB), iridium oxide (IrO₂) etc. present coloration in their oxidized state
- (ii) *Cathodically coloring* - Cathodically coloring materials e.g., WO₃, molybdenum trioxide (MoO₃), PEDOT, titanium oxide (TiO₂) etc. are colored in reduced form.

Most of the electrochromes fall into these two categories, where their optical state changes between transmissive to colored states. But there are other materials that switch their chromatic state between two or more colors like vanadium pentoxide (V₂O₅), these are referred to as poly-electrochromic or multi-chromic materials. Since the start of the journey of electrochromism with WO₃, different classes of electrochromic materials have come out with a wide range from the organic to inorganic molecules.

(a) Viologens – Viologens are small organic molecules precisely, di-quaternized 4,4'-bipyridyl salts, with a generic formula $(C_5H_4NR)_2^{n+}(X^-)_n$. They have three stable redox states – (i) dicationic form which is colorless and the most stable state, (ii) radical cation state, produced via one-electron reduction of the dicationic state, which shows intense violet-blue coloration and (iii) di-reduced neutral form with weak yellow-brown color.[61] All the states are complemented by the charge balancing X^- anion. Paraquat is a well-known viologen used as herbicide, in which alkyl 'R' is methyl group.

(b) Conjugated polymers – These are macro-molecular organic chains with backbones made up of alternating single and double bonds through which they can conduct charges, as a result they are also referred to as conducting polymers. Their extended structure allows the delocalization of charges during redox reactions.[62] Conducting polymers that received most attention regarding electrochromism are polyaniline (PANI), polythiophenes, polypyrroles, PEDOT etc.

(c) Metal phthalocyanines – The metal in metal phthalocyanines can be either transition metals like zirconium, molybdenum etc. or rare earth elements like lutetium, americium, neodymium, europium etc. Based on the presence of metal atoms, electrochromic metal phthalocyanines can be of two types, either transition metal phthalocyanines or lanthanide-based phthalocyanine complexes. Many of these materials show multiple shades while undergoing redox reactions which are associated with metal to ligand charge transfer processes.[24] The most common metal phthalocyanine is lutetium bis(phthalocyanine) $(Lu(Pc)_2)$.

(d) Metal hexacyanometallates – These are a group of mixed valance materials bearing the generic formula $M^a_x[M^b(CN)_6]_z$, where M^a and M^b are the transition metal ions with different valance states. The most popular metal hexacyanometallates is prussian blue (PB), also known as iron(III) hexacyanoferrate(II) $(Fe^{III}_4[Fe^{II}(CN)_6]_3)$. In PB, intra-valence charge transfer occurs between Fe^{III} and Fe^{II} ions.

(e) Transition metal oxides – The most explored materials in this field of electrochromism from the beginning are the TMOs. Electrochromism in TMOs appears due to optical inter-valance charge transfer subjected to redox reaction. A few well-known electrochromic oxides are NiO, WO_3 , TiO_2 , MnO_2 , V_2O_5 etc. These materials are naturally abundant, environmentally benign and display very good environmental, chemical and thermal stabilities compared to other electrochromes.[24] Hence, in terms of commercial applications, these materials are highly

feasible and cost-effective. This thesis is primarily based on the electrochromism of TMOs and especially that of NiO and V₂O₅.

1.4.4 Electrochromism in transition metal oxides

Metal oxides with transition metal centres show electrochromism. The mechanism of electrochromism in TMOs varies from one to another. Most of the TMOs take an octahedral crystal structure. Redox reactions change the valency of the metal centres and optical intervalence charge transfer (IVCT) between metal centres takes place, which causes the color change in these materials. The whole process is associated with the insertions or extractions of ions which do the charge balancing into the respective lattice sites.[24]

Depending on coloration electrochromic oxides can be divided into two classes – first, the oxides that show coloration upon cation extraction or anion insertion that is anodically coloring electrochromic oxides and second cathodically coloring materials that show coloration upon cation insertion, Figure 1.5 presents the corresponding transition metals. Vanadium based oxides are intermediate types which show both cathodic and anodic coloration.[26] Oxides of nickel (Ni), tungsten (W), iridium (Ir) and molybdenum (Mo) show most intense colorations and are used as primary electrochromes, whereas the other TMOs that show less coloration ability are employed as counter layers or secondary electrochromes.[23]

ELECTROCHROMIC OXIDES:

H																				He
Li	Be											B	C	N	O	F	Ne			
Na	Mg											Al	Si	P	S	Cl	Ar			
K	Ca	Sc	Ti	V	Cr	Mn	Fe	Co	Ni	Cu	Zn	Ga	Ge	As	Se	Br	Kr			
Rb	Sr	Y	Zr	Nb	Mo	Tc	Ru	Rh	Pd	Ag	Cd	In	Sn	Sb	Te	I	Xe			
Cs	Ba	La	Hf	Ta	W	Re	Os	Ir	Pt	Au	Hg	Tl	Pb	Bi	Po	At	Rn			
Fr	Ra	Ac																		

	Cathodic coloration
	Anodic coloration

Figure 1.5: Periodic table of elements excluding lanthanoid and actinoid series, where transition metals at different shaded boxes, produce either cathodically or anodically coloring oxides. Figure is taken from ref [26]

A few criteria are required to be fulfilled to reveal electrochromism in TMOs. First and foremost, the material should be redox active i.e., the bonding of that structure should allow the electron gain or loss. Secondly, at the time of redox coloration the charge gained should be dispersed via electron hopping which is often considered to be a small polaronic motion, associated with an ionic movement. Finally, IVCT should cause the color change of the redox

active material. IVCT occurs between homonuclear atoms at different sites with different oxidation states in single-metal oxides, or between heteronuclear atoms in binary-metal oxides which produces the change in absorption of the material in the electromagnetic spectrum associated with the color change.[23]

Most TMOs are constituted of MO_6 octahedra with a central transition metal atom M neighboured by six equidistant oxygen atoms. These building units arrange in an edge-sharing or corner-sharing manner to make the unified structure. During redox reactions, ions either reside on the surfaces of these octahedra or intercalate into their vacant spaces.[12] Octahedral symmetry is essential for the novel electronic features of TMOs. Due to crystal fields, d orbitals of transition metals split and form bands conventionally designated as e_g and t_{2g} . Oxygen 2p band is separated from them by an energy gap.[26]

The leftmost band diagram scheme is suitable for cathodically coloring materials such as H_xWO_3 ($x < 0.5$). For pure WO_3 , O2p band is completely filled and d band is totally empty which causes a wide bandgap for the material, making it transparent. But intercalation of ions and electrons partially fills the t_{2g} band causing an optical absorption for the material.[26]

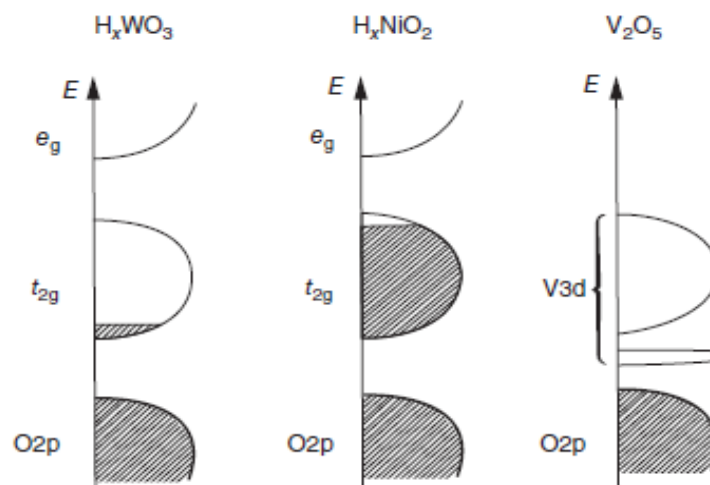


Figure 1.6: Schematic band diagrams of different TMOs, figure taken from ref [26]

Second band diagram is convenient for anodically coloring oxides like NiO_x ($x > 1$) or hydrous NiO which consists of edge-sharing NiO_6 octahedra. The edge-sharing arrangement creates some octahedral deformation in the crystal structure. Pure NiO possesses an unoccupied t_{2g} band. Intercalation of electrons and ions almost completely fills the states of t_{2g} level and the band gap i.e., the difference between e_g and t_{2g} levels becomes large enough to make the material transparent.[63]

The last panel presents the band diagram of V_2O_5 which shows both cathodic and anodic coloration. The crystal structure of V_2O_5 is constituted of either highly distorted VO_6 octahedra or most appropriately square pyramidal VO_5 units. Significant deviation from octahedral structure causes a narrow split off d band in the band gap which gets filled by electron and ion injection during redox reactions and promotes the optical band gap widening. This unique characteristic of band structure attributes to its anodic and cathodic coloration.[29]

1.4.5 Application of electrochromic materials

Ever since the discovery of electrochromic materials, electrochromic technology has been implemented in various fields of research and development. Apart from the applications of electrochromic materials in electronic information displays, smart windows, self-dimming mirrors etc., recently the fusion of electrochromic technology with other advanced technologies has given a strong impetus to its further development in the fields of wearable electronic devices like e-skins and sensors, smart windows with temperature control technologies for indoor comfort, energy harvesting and smart energy storage applications etc.[64]

- Electrochromic technology combined with wearable device technology give rise to wearable electrochromic fabrics which have a great future in smart cloths, military uniforms with adaptable camouflage technology for use in defence, implantable displays, electronic skins (e-skins), skin-patch biosensor etc.[65, 66]
- Fusion of electrochromism with sensing technology enables the direct determination of sensing information by naked eye. This offers potential applications in electrochromic biosensors, electrochromic chemosensors, electrochromic gas sensors, electrochromic mechanical sensors (e-skin) etc.[65, 67, 68]
- Traditional electrochromic windows were mostly developed for modulating the radiation of visible wavelength regions, but heating is mainly caused due to near-infrared radiation. Currently the dual-band electrochromism allows us to independently control the visible and infrared radiation of the solar spectrum; thus, providing us with four distinct operational modes for the smart window namely – (i) bright and warm, (ii) dark and warm, (iii) bright and cool and (iv) dark and cool mode.[69-71]
- Conventional electrochromic devices need external energy sources like batteries, supercapacitors for their color switching. But, the integration of energy harvesting systems

such as solar cells or nanogenerators with electrochromic modules makes it a self-powered system, eliminating the dependence on external energy sources.[72, 73]

- Electrochromic devices and electrochemical energy storage devices possess similar features in terms of working principle, material properties, device configuration etc., which allows the casting of electrochromic materials as an active layer in batteries or supercapacitors. This combination namely, an electrochromic energy storage device shows its state of charge by a dynamic change in its color, giving it the status of a smart energy storage device.[74]

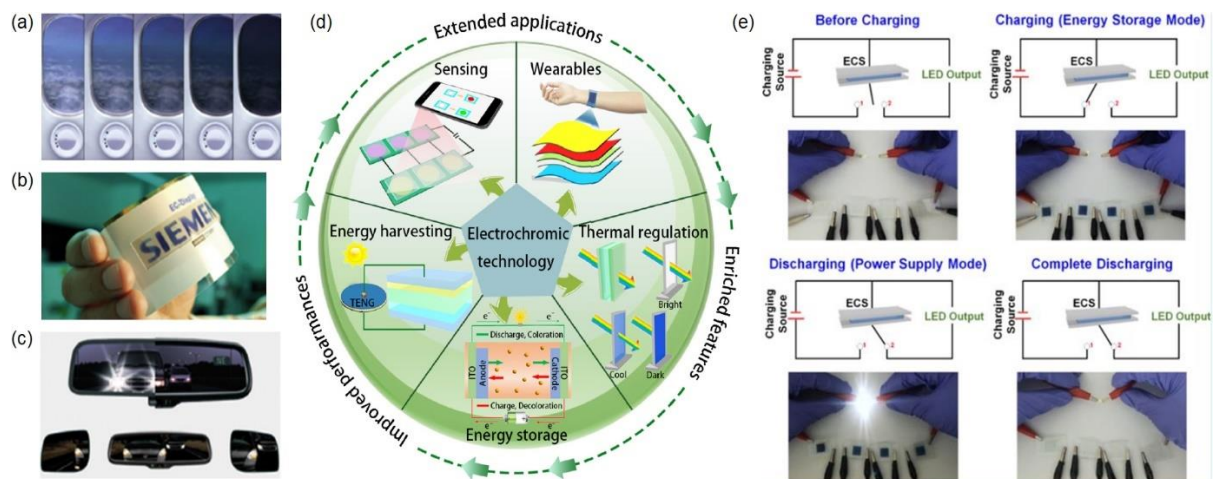


Figure 1.7: Applications of electrochromic materials - (a) electrochromic window installed in a Boeing aircraft manufactured by Smart Tint®, (b) flexible electrochromic label produced by Siemens®, (c) auto-dimming rear and side view mirrors of an automobile designed by Gentex®, (Figure 1.7a, 1.7b, 1.7c are reproduced as presented in Figure 1.3 in ref [10]) and (d) schematic illustrating different applications of electrochromic technology combined with new advanced technologies. Figure is taken from ref [64]. (e) Working of a WO₃ based electrochromic supercapacitor device, that displays blue color in its charged state and becomes transparent after discharging. Figure is taken from ref [75].

1.5 Climate change and exigency of alternative energies

The growth of modern civilization and its increasing energy demand has primarily been supported by non-renewable energy sources like natural gas, fossil fuels etc. But, the dearth of fossil fuels and impending calamities like global warming and climate change, due to the unrestrained usage of these resources, has become alarming issues in 21st century. Hence, current world is shifting towards the usage of sustainable energy from renewable energy sources like sunlight, wind, water, geothermal resources and biomass. Significant efforts are being put into the development of an emission-free low-carbon society.[76] A report by European Commission asserts that by 2050, 55-75% of the entire energy consumption would

be supplied by renewable energies, which was less than 10% back in 2010.[77] Regardless of having numerous advantages over non-renewable energy sources, the intermittent nature of renewable energy sources hinders the sufficient supply of energy to different sectors. This imbalance between demand and availability of energy propels the development of electrochemical energy storage and conversion devices.

1.5.1 Electrochemical energy storage devices

In general, electrochemical energy devices like batteries, supercapacitors, fuel cells, water electrolyzers etc. maintain a sustainable energy supply with low pollution and zero emission to the environment. These devices overcome the temporal and geographical fluctuations of renewable energy sources to meet the energy requirement in energy sectors. Fuel cells and water electrolyzers are electrochemical energy conversion systems where energy is converted from one form to another. Besides, batteries and supercapacitors are electrochemical energy storage systems that store electrical energy by different charge storage mechanisms.[78]

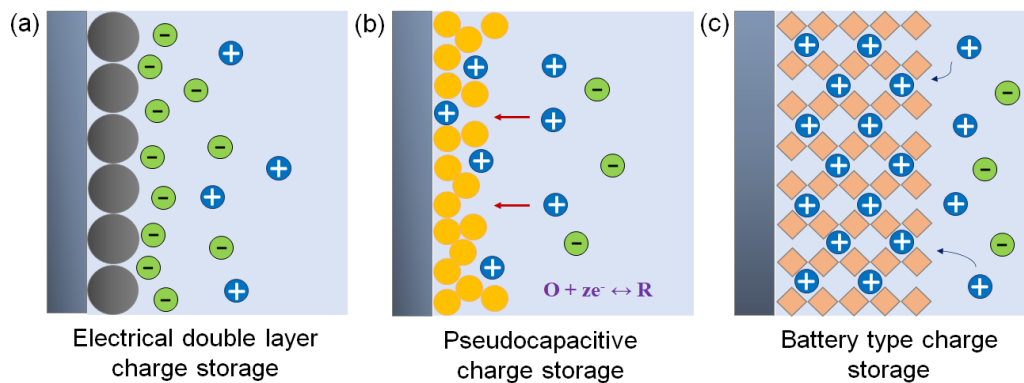


Figure 1.8: Different charge storage mechanisms in electrochemical ESDs

Typically, in batteries the electrochemical process is based on Faradaic reactions governed by diffusion through the bulk electrode material, which is often slow and leads to high energy density. Whereas supercapacitors store charge by surface-controlled adsorption process by forming an electrical double layer, which leads to high power density. This doesn't involve any redox reaction and is often referred to as electrical double layer capacitors (EDLC). There is another class of materials known as pseudocapacitive materials which exhibit surface-controlled Faradaic reactions. But they are different from battery materials as their redox reactions are quite faster and not governed by bulk diffusion.[79] These materials can achieve high power density like supercapacitors and their energy density can be higher than EDLC. Battery materials engineered at nanoscales can show pseudocapacitive properties with higher

power density because materials with such small dimensions can adsorb ions on their surfaces and create short diffusion lengths for ions.[80] As a result, nanostructured materials like TMOs, nitrides, carbides etc usually exhibit pseudocapacitive properties.[81, 82]

1.5.2 Context of smart windows and electrochromic energy storage

In concurrence with the worldwide effort of energy storage and saving, smart windows have become a key element for the architectural design of energy-efficient buildings. In current days, energy consumption in buildings in the developed countries is almost 20%-40% of their net primary energy.[83, 84] The energy consumption in buildings strongly depends on the windows, as during daytime building gets a substantial amount of sunlight and heat energy through windows. Along with extra decoration effects, the use of smart windows maintains indoor lighting and comfort by modulating the amount of sunlight passing through and significantly reducing the electricity consumption by the air conditioners. Thermochromic or photochromic materials can be used as glazing materials in smart windows, but electrochromic smart windows provide dynamic control to their tints and better durability over the other technologies.[85, 86]

Conventional electrochromic smart windows require external voltages for their transition from colored to bleached state and vice versa, causing additional electricity consumption. However, recent development in science and technology enables further integration of novel functionalities with smart window technology. Due to highly alike structure and working principle of energy storage devices and electrochromic smart windows, both can be incorporated into a single platform. The energy storage functionalities with electrochromic smart window technology help to minimize the requirement of external voltages in conventional electrochromic smart windows, as these modules show self-coloration or self-bleaching features by exhausting the consumed energy.[87-89] These devices arranged in smart grid structures in green buildings can maintain the sunshine during daytime and work as a back-up power source to light up the building and power up other electronic gadgets after sunset.[90, 91] From another viewpoint, inception of these futuristic devices, namely electrochromic energy storage devices embark on the intelligent automation of energy storage devices. Electrochromic energy storage devices display their energy storage level by changing color intensity and allow the dynamic monitoring of the device's state of charge in an interactive and intelligent manner and simultaneously protect the device from over-charging or over-discharging.

1.6 Importance of transition metal oxide nanostructures

Electrochemical performances of TMOs are often hindered by poor charge and ion transfer, which restrains them from extensive applications. The silver lining to this issue is the nanostructures of TMOs, as they offer very small charge diffusion paths at least in one dimension and very high specific surface area compared to their bulk counterpart. Large surface area permits fast charge transport at the electrode-electrolyte interface causing high electrochemical activity of the material, which promises enhanced electrochromic performance of the TMOs.[92] Extensive research has been performed by different groups of researchers around the globe on refinement of nanostructured TMOs' electrochemical performances, either by obtaining different synthesis procedures,[93, 94] or by making various nanocomposites.[95-98]

1.7 Aim and scope of the thesis

Out of various TMOs; this thesis mainly deals with NiO and V₂O₅, which are quite well-known as electrode materials in the fields of electrochromism,[52, 99-103] and smart energy storage devices.[104-109] Primary objective of this thesis is to synthesize nanostructures of NiO and V₂O₅ with superior electrochemical activities for their use as electrode materials in electrochromic smart window and electrochromic energy storage devices applications with an emphasis to explore their physical and electrochemical features. As discussed in the previous section due to low electrical conductivity, electrochromic performances of TMOs often face challenges like low optical contrast, poor coloration efficiency, inferior response speeds between their chromatic states etc.,[110] which requires further improvement for their integration in practical device applications. To address these problems, this thesis is split into the following chapters:

Chapter 1 starts with a brief introduction to different types of smart materials. The discussion further narrows down to the description of electrochromic materials which fall under a subsection of chromogenic smart materials. Major points related to electrochromic materials and devices are highlighted in this chapter. The remaining part of this chapter is focused on the need for alternative energy resources in the context of energy crisis and climate change and the importance of electrochromic smart windows and electrochromic energy storage devices is emphasized in this context. In the end, the chapter describes the need for TMO nanostructures in this research field and briefly discusses the objectives and extent of the thesis.

Chapter 1

Chapter 2 explores how the tuning of morphology and surface area affects the electrochromic properties of NiO, a well-known anodically coloring TMO. In this chapter, multi-shelled hollow NiO microsphere sample was synthesized in a template-based synthesis technique in presence of glucose and the electrochromic properties were compared and contrasted with NiO micro-flake sample which was prepared in the absence of glucose. Later in this work, multi-shelled hollow NiO microspheres were employed as an electrode material in a polymer gel electrolyte based quasi-solid electrochromic device for smart window application.

Chapter 3 investigates the feasibility of using metal organic framework (MOF) derived NiO over NiO MS-HMS sample as an electrode material for its use as an electrochromic material. Carbon-embedded porous structure of NiO makes it a better performing material than the former. The electrochromic performances and other electrochemical properties of the MOF-derived NiO samples were investigated thoroughly to obtain the most optimized one in terms of performance metrics. It was subsequently used as a positive electrode material to construct a rechargeable Zn-NiO electrochromic battery, which is capable of flaunting its state of charge by a color change from dark brown (charged) to colorless (discharged).

Chapter 4 details a work based on V₂O₅. The chapter begins with the synthesis of MOF-derived porous V₂O₅ material which as an electrochromic electrode, demonstrated descent performance with multiple chromatic states. The material was further integrated as a smart negative electrode in a multicolored electrochromic asymmetric supercapacitor module with conducting polyaniline (PANI) as its positive counterpart. Multiple hues enable more control over the visual determination of the state of charge of the device, compared to the previous work of electrochromic Zn-NiO battery, where the change in color of the device was purely monochromatic.

Chapter 5 summarizes the whole thesis work and emphasizes the future outlook.

1.8 Bibliography

- [1] J. Mishra, Smart Materials-Types SS and their Application: A Review, *Int. J. Mech. Prod. Eng.*, 5 (2007).
- [2] D.M. Addington, D.L. Schodek, Types and characteristics of smart materials, *Smart Materials and New Technologies: For the Architecture and Design Professions*, Architectural Press, Elsevier, 2005, pp. 79-108.
- [3] C.M. Lampert, Chromogenic smart materials, *Mater. today*, 7 (2004) 28-35.
- [4] <https://www.better-glass.com/pdlc-switchable-glass/pdlc-smart-switchable-glass.html>
- [5] A. Corning, Smart Glass Opens a Window to New Applications, 2022, <https://www.radiantvisionsystems.com/blog/smart-glass-opens-window-new-applications>.
- [6] B.A. Korgel, Composite for smarter windows, *Nature*, 500 (2013) 278-279.
- [7] A. Choudhary, E. Prasad, Electrochromic Glass Market by Application (Windows, Mirror, and Display) and End-User Industry (Construction, Automotive, Aerospace, and Others): Global Opportunity Analysis and Industry Forecast, 2020–2027, 2020, <https://www.alliedmarketresearch.com/electrochromic-glass-market>.
- [8] R.J. Mortimer, Electrochromic materials, *Chem. Soc. Rev.*, 26 (1997) 147-156.
- [9] D.R. Rosseinsky, R.J. Mortimer, Electrochromic Systems and the Prospects for Devices, *Adv. Mater.*, 13 (2001) 783-793.
- [10] M.H. Chua, T. Tang, K.H. Ong, W.T. Neo, J.W. Xu, Introduction to Electrochromism, in: J.W. Xu, M.H. Chua, K.W. Shah (Eds.) *Electrochromic Smart Materials: Fabrication and Applications*, The Royal Society of Chemistry, 2019, pp. 1-21.
- [11] N. Kobosew, N. Nekrassov, *Electrochem.*, 36 (1930) 529-544.
- [12] C.G. Granqvist, *Handbook of inorganic electrochromic materials*, Elsevier (1995).
- [13] J.R. Platt, Electrochromism, a Possible Change of Color Producing in Dyes by an Electric Field, *J. Chem. Phys.*, 34 (1961) 862-863.
- [14] S.K. Deb, A novel electrophotographic system, *Appl. Opt. Suppl.*, 8 (1969) 192-195.
- [15] S.K. Deb, Optical and photoelectric properties and colour centres in thin films of tungsten oxide, *Philos. Mag.*, 27 (1973) 801-822.
- [16] L.S. Palatnik, Y.I. Malyuk, V.V. Belozherov, An X-ray diffraction study of the mechanism of reversible electrochemical dielectric \leftrightarrow semiconductor transformations in Nb_2O_5 , *Dokl. Chem. Technol.*, 215 (1974) 68-71.

- [17] J.S.E.M. Svensson, C.G. Granqvist, Electrochromic hydrated nickel oxide coatings for energy efficient windows: Optical properties and coloration mechanism, *Appl. Phys. Lett.*, 49 (1986) 1566-1568.
- [18] W. Estrada, A.M. Andersson, C.G. Granqvist, Electrochromic nickel-oxide-based coatings made by reactive dc magnetron sputtering: Preparation and optical properties, *J. Appl. Phys.*, 64 (1988) 3678-3683.
- [19] C.M. Lampert, Electrochromic materials and devices for energy efficient windows, *Sol. Energy Mater.*, 11 (1984) 1-27.
- [20] J.S.E.M. Svensson, C.G. Granqvist, Electrochromic tungsten oxide films for energy efficient windows, *Sol. Energy Mater.*, 11 (1984) 29-34.
- [21] C. Yan, W. Kang, J. Wang, M. Cui, X. Wang, C.Y. Foo, K.J. Chee, P.S. Lee, Stretchable and Wearable Electrochromic Devices, *ACS Nano*, 8 (2014) 316-322.
- [22] G. Yang, J. Ding, B. Yang, X. Wang, C. Gu, D. Guan, Y. Yu, Y.-M. Zhang, S.X.-A. Zhang, Highly stretchable electrochromic hydrogels for use in wearable electronic devices, *J. Mater. Chem. C*, 7 (2019) 9481-9486.
- [23] P. Monk, R. Mortimer, D. Rosseinsky, *Electrochromism and Electrochromic Devices*, Cambridge University Press, Cambridge, (2007).
- [24] W.T. Neo, M.H. Chua, J.W. Xu, *Fundamentals of Electrochromic Materials and Devices*, in: J.W. Xu, M.H. Chua, K.W. Shah (Eds.) *Electrochromic Smart Materials: Fabrication and Applications*; Smart Materials Series, The Royal Society of Chemistry 2019, pp. 22-50.
- [25] E.L. Runnerstrom, A. Llordés, S.D. Lounis, D.J. Milliron, Nanostructured electrochromic smart windows: traditional materials and NIR-selective plasmonic nanocrystals, *Chem. Commun.*, 50 (2014) 10555-10572.
- [26] C.-G. Granqvist, *Electrochromic metal oxides: an introduction to materials and devices*, in: R.J. Mortimer, D.R. Rosseinsky, P.M.S. Monk (Eds.) *Electrochromic Materials and Devices*, Wiley-VCH Verlag GmbH, Weinheim, Germany, 2015, pp. 3-40.
- [27] Í.B. Pehlivan, R. Marsal, E. Pehlivan, E.L. Runnerstrom, D.J. Milliron, C.G. Granqvist, G.A. Niklasson, Electrochromic devices with polymer electrolytes functionalized by SiO₂ and In₂O₃:Sn nanoparticles: Rapid coloring/bleaching dynamics and strong near-infrared absorption, *Sol. Energy Mater. Sol. Cells*, 126 (2014) 241-247.
- [28] P.-W. Chen, C.-T. Chang, T.-F. Ko, S.-C. Hsu, K.-D. Li, J.-Y. Wu, Fast response of complementary electrochromic device based on WO₃/NiO electrodes, *Sci. Rep.*, 10 (2020) 8430.

- [29] C.G. Granqvist, Oxide electrochromics: An introduction to devices and materials, *Sol. Energy Mater. Sol. Cells*, 99 (2012) 1-13.
- [30] N.L. Sbar, L. Podbelski, H.M. Yang, B. Pease, Electrochromic dynamic windows for office buildings, *Int. J. Sustain. Built Environ.*, 1 (2012) 125-139.
- [31] F.G.K. Baucke, K. Bange, T. Gambke, Reflecting electrochromic devices, *Displays*, 9 (1988) 179-187.
- [32] Z. Wang, X. Wang, S. Cong, J. Chen, H. Sun, Z. Chen, G. Song, F. Geng, Q. Chen, Z. Zhao, Towards full-colour tunability of inorganic electrochromic devices using ultracompact fabry-perot nanocavities, *Nat. Commun.*, 11 (2020) 302.
- [33] Y. Wu, C.H.M. Marée, R.F. Haglund, J.D. Hamilton, M.A. Morales Paliza, M.B. Huang, L.C. Feldman, R.A. Weller, Resistivity and oxygen content of indium tin oxide films deposited at room temperature by pulsed-laser ablation, *J. Appl. Phys.*, 86 (1999) 991-994.
- [34] M.S. Farhan, E. Zalnezhad, A.R. Bushroa, A.A.D. Sarhan, Electrical and optical properties of indium-tin oxide (ITO) films by ion-assisted deposition (IAD) at room temperature, *Int. J. Precis. Eng. Manuf.*, 14 (2013) 1465-1469.
- [35] L.-M. Wang, C.-Y. Wang, C.-R. Jheng, S.-J. Wu, C.-K. Sai, Y.-J. Lee, C.-Y. Chiang, B.-Y. Shew, Characteristics of low-resistivity aluminum-doped zinc oxide films deposited at room temperature by off-axis radio-frequency sputtering on flexible plastic substrates, *Appl. Phys. A*, 122 (2016) 731.
- [36] K.J. Cummings, M.A. Virji, J.Y. Park, M.L. Stanton, N.T. Edwards, B.C. Trapnell, B. Carey, A.B. Stefaniak, K. Kreiss, Respirable indium exposures, plasma indium, and respiratory health among indium-tin oxide (ITO) workers, *Am. J. Ind. Med.*, 59 (2016) 522-531.
- [37] H. Wu, D. Kong, Z. Ruan, P.-C. Hsu, S. Wang, Z. Yu, T.J. Carney, L. Hu, S. Fan, Y. Cui, A transparent electrode based on a metal nanotrough network, *Nat. Nanotechnol.*, 8 (2013) 421-425.
- [38] E.O. Polat, O. Balcı, C. Kocabas, Graphene based flexible electrochromic devices, *Sci. Rep.*, 4 (2014) 6484.
- [39] W.-R. Lian, Y.-C. Huang, Y.-A. Liao, K.-L. Wang, L.-J. Li, C.-Y. Su, D.-J. Liaw, K.-R. Lee, J.-Y. Lai, Flexible Electrochromic Devices Based on Optoelectronically Active Polynorbornene Layer and Ultratransparent Graphene Electrodes, *Macromolecules*, 44 (2011) 9550-9555.

- [40] M. Nikolou, A.L. Dyer, T.T. Steckler, E.P. Donoghue, Z. Wu, N.C. Heston, A.G. Rinzler, D.B. Tanner, J.R. Reynolds, Dual n- and p-Type Dopable Electrochromic Devices Employing Transparent Carbon Nanotube Electrodes, *Chem. Mater.*, 21 (2009) 5539-5547.
- [41] K. Yanagi, R. Moriya, Y. Yomogida, T. Takenobu, Y. Naitoh, T. Ishida, H. Kataura, K. Matsuda, Y. Maniwa, Electrochromic Carbon Electrodes: Controllable Visible Color Changes in Metallic Single-Wall Carbon Nanotubes, *Adv. Mater.*, 23 (2011) 2811-2814.
- [42] A. Elschner, W. Lövenich, Solution-deposited PEDOT for transparent conductive applications, *MRS Bulletin*, 36 (2011) 794-798.
- [43] A.L.S. Eh, X. Lu, P.S. Lee, Advances in Polymer Electrolytes for Electrochromic Applications, in: R.J. Mortimer, D.R. Rosseinsky, P.M.S. Monk (Eds.) *Electrochromic Materials and Devices*, John Wiley & Sons, 2015, pp. 289-310.
- [44] V.K. Thakur, G. Ding, J. Ma, P.S. Lee, X. Lu, Hybrid Materials and Polymer Electrolytes for Electrochromic Device Applications, *Adv. Mater.*, 24 (2012) 4071-4096.
- [45] W.H. Meyer, Polymer Electrolytes for Lithium-Ion Batteries, *Adv. Mater.*, 10 (1998) 439-448.
- [46] A. Gonçalves, C. Costa, S. Pereira, N. Correia, M.M. Silva, P.C. Barbosa, L.C. Rodrigues, I. Henriques, R. Martins, E. Fortunato, Study of electrochromic devices with nanocomposites polymethacrylate hydroxyethylene resin based electrolyte, *Polym. Adv. Technol.*, 23 (2012) 791-795.
- [47] A. Manuel Stephan, K.S. Nahm, Review on composite polymer electrolytes for lithium batteries, *Polymer*, 47 (2006) 5952-5964.
- [48] R.C. Agrawal, G.P. Pandey, Solid polymer electrolytes: materials designing and all-solid-state battery applications: an overview, *J. Phys. D: Appl. Phys.*, 41 (2008) 223001.
- [49] N.A. Choudhury, S. Sampath, A.K. Shukla, Hydrogel-polymer electrolytes for electrochemical capacitors: an overview, *Energy Environ. Sci.*, 2 (2009) 55-67.
- [50] F. Huguenin, M. Ferreira, V. Zucolotto, F.C. Nart, R.M. Torresi, O.N. Oliveira, Molecular-Level Manipulation of V₂O₅/Polyaniline Layer-by-Layer Films To Control Electrochromogenic and Electrochemical Properties, *Chem. Mater.*, 16 (2004) 2293-2299.
- [51] A. Zimmer, M. Tresse, N. Stein, D. Horwat, C. Boulanger, Towards enhanced durability of electrochromic WO₃ interfaced with liquid or ceramic sodium-based electrolytes, *Electrochim. Acta*, 360 (2020) 136931.

- [52] X. Ju, F. Yang, X. Zhu, X. Jia, Zinc Ion Intercalation/Deintercalation of Metal Organic Framework-Derived Nanostructured NiO@C for Low-Transmittance and High-Performance Electrochromism, *ACS Sustainable Chem. Eng.*, 8 (2020) 12222-12229.
- [53] K. Xu, Electrolytes and Interphases in Li-Ion Batteries and Beyond, *Chem. Rev.*, 114 (2014) 11503-11618.
- [54] Y. Abe, S.-H. Lee, C.E. Tracy, J.R. Pitts, S.K. Deb, Electrochromic Properties of Sputtered Ni Oxide Thin Films in Acidic KCl+H₂SO₄ Aqueous Solutions, *Electrochem. Solid-State Lett.*, 9 (2006) J31.
- [55] Z. Li, Z. Yu, W. Wang, J. Hou, L. Gao, X. Gu, G. Su, Nickel oxide film with tertiary hierarchical porous structure and high electrochromic performance and stability, *Mater. Chem. Phys.*, 269 (2021) 124738.
- [56] P.V. Ashrit, F.E. Girouard, V.-V. Truong, Fabrication and testing of an all-solid state system for smart window application, *Solid State Ion.*, 89 (1996) 65-73.
- [57] S.J. Yoo, J.W. Lim, Y.-E. Sung, Improved electrochromic devices with an inorganic solid electrolyte protective layer, *Sol. Energy Mater. Sol. Cells*, 90 (2006) 477-484.
- [58] X. Yu, J.B. Bates, G.E. Jellison, F.X. Hart, A Stable Thin-Film Lithium Electrolyte: Lithium Phosphorus Oxynitride, *J. Electrochem. Soc.*, 144 (1997) 524-532.
- [59] Y.-F. Gong, X.-K. Fu, S.-P. Zhang, Q.-L. Jiang, Preparation of a Star Network PEG-based Gel Polymer Electrolyte and Its Application to Electrochromic Devices, *Chin. J. Chem.*, 25 (2007) 1743-1747.
- [60] D. Eric Shen, A.M. Österholm, J.R. Reynolds, Out of sight but not out of mind: the role of counter electrodes in polymer-based solid-state electrochromic devices, *J. Mater. Chem. C*, 3 (2015) 9715-9725.
- [61] L. Striepe, T. Baumgartner, Viologens and Their Application as Functional Materials, *Chem. Eur. J.*, 23 (2017) 16924-16940.
- [62] A. Kraft, Electrochromism: a fascinating branch of electrochemistry, *ChemTexts*, 5 (2018) 1.
- [63] C.G. Granqvist, M.A. Arvizu, İ.B. Pehlivan, H.Y. Qu, R.T. Wen, G.A. Niklasson, Electrochromic materials and devices for energy efficiency and human comfort in buildings: A critical review, *Electrochim. Acta*, 259 (2018) 1170-1182.
- [64] Z. Wang, X. Wang, S. Cong, F. Geng, Z. Zhao, Fusing electrochromic technology with other advanced technologies: A new roadmap for future development, *Mater. Sci. Eng. R Rep.*, 140 (2020) 100524.

- [65] S. Santiago-Malagón, D. Río-Colín, H. Azizkhani, M. Aller-Pellitero, G. Guirado, F.J. del Campo, A self-powered skin-patch electrochromic biosensor, *Biosens. Bioelectron.*, 175 (2021) 112879.
- [66] H.-H. Chou, A. Nguyen, A. Chortos, J.W.F. To, C. Lu, J. Mei, T. Kurosawa, W.-G. Bae, J.B.H. Tok, Z. Bao, A chameleon-inspired stretchable electronic skin with interactive colour changing controlled by tactile sensing, *Nat. Commun.*, 6 (2015) 8011.
- [67] Y. Wang, L. Zhang, K. Cui, C. Xu, H. Li, H. Liu, J. Yu, Solar driven electrochromic photoelectrochemical fuel cells for simultaneous energy conversion, storage and self-powered sensing, *Nanoscale*, 10 (2018) 3421-3428.
- [68] H. Kai, W. Suda, S. Yoshida, M. Nishizawa, Organic electrochromic timer for enzymatic skin patches, *Biosens. Bioelectron.*, 123 (2019) 108-113.
- [69] M. Barawi, G. Veramonti, M. Epifani, R. Giannuzzi, T. Sibillano, C. Giannini, A. Rougier, M. Manca, A dual band electrochromic device switchable across four distinct optical modes, *J. Mater. Chem. A*, 6 (2018) 10201-10205.
- [70] P. Yilmaz, M. Magni, S. Martinez, R.M. Gonzalez Gil, M. Della Pirriera, M. Manca, Spectrally Selective PANI/ITO Nanocomposite Electrodes for Energy-Efficient Dual Band Electrochromic Windows, *ACS Appl. Energy Mater.*, 3 (2020) 3779-3788.
- [71] C.J. Dahlman, Y. Tan, M.A. Marcus, D.J. Milliron, Spectroelectrochemical Signatures of Capacitive Charging and Ion Insertion in Doped Anatase Titania Nanocrystals, *J. Am. Chem. Soc.*, 137 (2015) 9160-9166.
- [72] X. Yang, G. Zhu, S. Wang, R. Zhang, L. Lin, W. Wu, Z.L. Wang, A self-powered electrochromic device driven by a nanogenerator, *Energy Environ. Sci.*, 5 (2012) 9462-9466.
- [73] Y. Zhong, Z. Chai, Z. Liang, P. Sun, W. Xie, C. Zhao, W. Mai, Electrochromic Asymmetric Supercapacitor Windows Enable Direct Determination of Energy Status by the Naked Eye, *ACS Appl. Mater. Interfaces*, 9 (2017) 34085-34092.
- [74] P. Yang, P. Sun, W. Mai, Electrochromic energy storage devices, *Mater. Today*, 19 (2016) 394-402.
- [75] T.Y. Yun, X. Li, S.H. Kim, H.C. Moon, Dual-Function Electrochromic Supercapacitors Displaying Real-Time Capacity in Color, *ACS Appl. Mater. Interfaces*, 10 (2018) 43993-43999.
- [76] <https://www.edfenergy.com/for-home/energywise/renewable-energy-sources>
- [77] World Energy Outlook/Global Energy Trends, International Energy Agency (2012).

- [78] M. Winter, R.J. Brodd, What Are Batteries, Fuel Cells, and Supercapacitors?, *Chem. Rev.*, 104 (2004) 4245-4270.
- [79] P. Simon, Y. Gogotsi, B. Dunn, Where Do Batteries End and Supercapacitors Begin?, *Science*, 343 (2014) 1210-1211.
- [80] A.S. Aricò, P. Bruce, B. Scrosati, J.-M. Tarascon, W. van Schalkwijk, Nanostructured materials for advanced energy conversion and storage devices, *Nature Mater.*, 4 (2005) 366-377.
- [81] M. Sathiya, A.S. Prakash, K. Ramesha, J.M. Tarascon, A.K. Shukla, V₂O₅-Anchored Carbon Nanotubes for Enhanced Electrochemical Energy Storage, *J. Am. Chem. Soc.*, 133 (2011) 16291-16299.
- [82] V. Augustyn, P. Simon, B. Dunn, Pseudocapacitive oxide materials for high-rate electrochemical energy storage, *Energy Environ. Sci.*, 7 (2014) 1597-1614.
- [83] L. Pérez-Lombard, J. Ortiz, C. Pout, A review on buildings energy consumption information, *Energy Build.*, 40 (2008) 394-398.
- [84] W.J. Hee, M.A. Alghoul, B. Bakhtyar, O. Elayeb, M.A. Shameri, M.S. Alrubaih, K. Sopian, The role of window glazing on daylighting and energy saving in buildings, *Renew. Sustain. Energy Rev.*, 42 (2015) 323-343.
- [85] N.C. Davy, M. Sezen-Edmonds, J. Gao, X. Lin, A. Liu, N. Yao, A. Kahn, Y.-L. Loo, Pairing of near-ultraviolet solar cells with electrochromic windows for smart management of the solar spectrum, *Nat. Energy*, 2 (2017) 17104.
- [86] J. Wang, L. Zhang, L. Yu, Z. Jiao, H. Xie, X.W. Lou, X. Wei Sun, A bi-functional device for self-powered electrochromic window and self-rechargeable transparent battery applications, *Nat. Commun.*, 5 (2014) 4921.
- [87] W. Zhang, H. Li, M. Al-Hussein, A.Y. Elezzabi, Electrochromic Battery Displays with Energy Retrieval Functions Using Solution-Processable Colloidal Vanadium Oxide Nanoparticles, *Adv. Optical Mater.*, 8 (2020) 1901224.
- [88] H. Li, C.J. Firby, A.Y. Elezzabi, Rechargeable Aqueous Hybrid Zn²⁺/Al³⁺ Electrochromic Batteries, *Joule*, 3 (2019) 2268-2278.
- [89] S.B. Singh, D.T. Tran, K.-U. Jeong, N.H. Kim, J.H. Lee, A Flexible and Transparent Zinc-Nanofiber Network Electrode for Wearable Electrochromic, Rechargeable Zn-Ion Battery, *Small*, 18 (2022) 2104462.
- [90] G. Cai, P. Darmawan, X. Cheng, P.S. Lee, Inkjet Printed Large Area Multifunctional Smart Windows, *Adv. Energy Mater.*, 7 (2017) 1602598.

- [91] B. Wang, M. Cui, Y. Gao, F. Jiang, W. Du, F. Gao, L. Kang, C. Zhi, H. Luo, A Long-Life Battery-Type Electrochromic Window with Remarkable Energy Storage Ability, *Sol. RRL*, 4 (2020) 1900425.
- [92] S. Xiong, P.S. Lee, X. Lu, Nanostructures in electrochromic materials, in: R.J. Mortimer, D.R. Rosseinsky, P.M.S. Monk (Eds.) *Electrochromic materials and devices*, Wiley-VCH Verlag GmbH, Weinheim, Germany, 2015, pp. 251-288.
- [93] T. Guo, M.-S. Yao, Y.-H. Lin, C.-W. Nan, A comprehensive review on synthesis methods for transition-metal oxide nanostructures, *CrystEngComm*, 17 (2015) 3551-3585.
- [94] S. Yadav, N. Rani, K. Saini, A review on transition metal oxides based nanocomposites, their synthesis techniques, different morphologies and potential applications, *IOP Conf. Ser.: Mater. Sci. Eng.*, 1225 (2022) 012004.
- [95] R. Elakkiya, G. Maduraiveeran, Two-Dimensional Earth-Abundant Transition Metal Oxides Nanomaterials: Synthesis and Application in Electrochemical Oxygen Evolution Reaction, *Langmuir*, 36 (2020) 4728-4736.
- [96] A.S. Agnihotri, A. Varghese, M. Nidhin, Transition metal oxides in electrochemical and bio sensing: a state-of-art review, *Appl. Surf. Sci. Adv.*, 4 (2021) 100072.
- [97] M. Zheng, H. Tang, L. Li, Q. Hu, L. Zhang, H. Xue, H. Pang, Hierarchically Nanostructured Transition Metal Oxides for Lithium-Ion Batteries, *Adv. Sci.*, 5 (2018) 1700592.
- [98] W. Wu, M. Wang, J. Ma, Y. Cao, Y. Deng, Electrochromic Metal Oxides: Recent Progress and Prospect, *Adv. Electron. Mater.*, 4 (2018) 1800185.
- [99] D. Ma, G. Shi, H. Wang, Q. Zhang, Y. Li, Hierarchical NiO microflake films with high coloration efficiency, cyclic stability and low power consumption for applications in a complementary electrochromic device, *Nanoscale*, 5 (2013) 4808-4815.
- [100] S. Pereira, A. Gonçalves, N. Correia, J. Pinto, L. Pereira, R. Martins, E. Fortunato, Electrochromic behavior of NiO thin films deposited by e-beam evaporation at room temperature, *Sol. Energy Mater. Sol. Cells*, 120 (2014) 109-115.
- [101] Z. Tong, J. Hao, K. Zhang, J. Zhao, B.-L. Su, Y. Li, Improved electrochromic performance and lithium diffusion coefficient in three-dimensionally ordered macroporous V₂O₅ films, *J. Mater. Chem. C*, 2 (2014) 3651-3658.
- [102] Y.-S. Hsiao, C.-W. Chang-Jian, W.-L. Syu, S.-C. Yen, J.-H. Huang, H.-C. Weng, C.-Z. Lu, S.-C. Hsu, Enhanced electrochromic performance of carbon-coated V₂O₅ derived from a metal-organic framework, *Appl. Surf. Sci.*, 542 (2021) 148498.

- [103] C. Xiong, A.E. Aliev, B. Gnade, K.J. Balkus, Fabrication of Silver Vanadium Oxide and V_2O_5 Nanowires for Electrochromics, *ACS Nano*, 2 (2008) 293-301.
- [104] G. Cai, X. Wang, M. Cui, P. Darmawan, J. Wang, A.L.-S. Eh, P.S. Lee, Electrochromo-supercapacitor based on direct growth of NiO nanoparticles, *Nano Energy*, 12 (2015) 258-267.
- [105] S. Zhou, S. Wang, S. Zhou, H. Xu, J. Zhao, J. Wang, Y. Li, An electrochromic supercapacitor based on an MOF derived hierarchical-porous NiO film, *Nanoscale*, 12 (2020) 8934-8941.
- [106] J. Wang, X. Huo, M. Guo, M. Zhang, A review of NiO-based electrochromic-energy storage bifunctional material and integrated device, *J. Energy Storage*, 47 (2022) 103597.
- [107] S. Zhang, S. Chen, Y. Luo, B. Yan, Y. Gu, F. Yang, Y. Cao, Large-scale preparation of solution-processable one-dimensional V_2O_5 nanobelts with ultrahigh aspect ratio for bifunctional multicolor electrochromic and supercapacitor applications, *J. Alloys Compd.*, 842 (2020) 155882.
- [108] L. Zhao, J. Kuang, W. Zhuang, J. Chao, W. Liao, X. Fu, C. Li, L. Ye, H. Liu, Studies on transmittance modulation and ions transfer kinetic based on capacitive-controlled 2D V_2O_5 inverse opal film for electrochromic energy storage application, *Nanotechnology*, 33 (2021) 054001.
- [109] L. Wang, M. Guo, J. Zhan, X. Jiao, D. Chen, T. Wang, A new design of an electrochromic energy storage device with high capacity, long cycle lifetime and multicolor display, *J. Mater. Chem. A*, 8 (2020) 17098-17105.
- [110] H. Liang, R. Li, C. Li, C. Hou, Y. Li, Q. Zhang, H. Wang, Regulation of carbon content in MOF-derived hierarchical-porous NiO@C films for high-performance electrochromism, *Mater. Horiz.*, 6 (2019) 571-579.

Chapter 2

*Multi-shelled hollow microspheres of NiO
for electrochromic smart window*

Declaration: The work has been published in the following journal:

J. Solid State Electrochem. 25, 821-830 (2021). Copyright. Springer Nature.

- **Abstract**

Multi-shelled nickel oxide (NiO) hollow spheres were synthesized by a facile glucose mediated hydrothermal route. The carbonaceous microspheres formed under reaction conditions were utilized as sacrificial templates for the formation of multi-shells. The shells with hollow interiors were formed via a single pyrolysis step. The geometry of the self-supported multi-shelled architecture provides enhanced specific surface area, which ensures the intimate contact of the electrolyte to the active Faradaic sites of the material to enhance ionic diffusion. In this work, we employed two NiO materials, as electrochromic materials, formed in presence and absence of glucose. As anticipated, NiO multi-shelled hollow microspheres exhibit a superior modulation of optical transmission, faster coloration and bleaching times and yield a coloration efficiency higher than that of NiO microflakes sample, which was synthesized in the absence of glucose. Further, the sample with superior electrochromic performances was utilized to make a quasi-solid-state electrochromic device with the aid of a gel electrolyte, that is capable of showing reversible color change from dark brown to transparent.

2.1 Introduction

Almost over the past two decades, transition metal oxides and hydroxides have drawn attention owing to their fascinating properties and several technological applications. Among them, nickel oxide (NiO) is of prime choice due to its low cost, ease of synthesis, excellent electrochemical performances, and obvious environmentally benign nature.[1-3] It has been widely used in lithium-ion batteries,[4-6] supercapacitors,[7-9] bio-sensing applications,[10-12] electrochromic devices[13-17] etc.

There are several reports on NiO deployed as an electrode material in electrochromic application [18, 19] and it has been noticed that the electrochromic performance of a material hugely depends on the synthesis procedure, morphology and conductivity of the material.[18, 20, 21] To better the overall electrochemical performance of the electrode materials, the best way is to enhance its surface area by tuning the morphology. Until now, different synthesis techniques have been explored to obtain a different morphology of NiO, such as nanosheets,[22] nanowires[23] and microspheres[24] to get improved performances. A variety of micro/nanostructures of NiO have been fabricated via sol-gel method,[25] chemical

precipitation,[26] electrodeposition,[27] chemical deposition,[28] pulsed laser deposition,[29] hydrothermal methods [30] etc. Among all these methods, the widely explored synthesis route is the hydrothermal technique because of its uncomplicated experimental conditions. Jiang et al. reported the synthesis of NiO nanorods of a 25–65-nm diameter nickel foam substrate via an in situ hydrothermal process.[31] Azimirad and co-workers showed how the reaction temperature can affect the morphology. They synthesized NiO nanoparticles, nanorods, and nanoworms at different hydrothermal temperatures (100 °C, 140 °C, 180 °C, and 220 °C respectively) for 12 h.[32] Mishra et al. demonstrated the hydrothermal growth of dense mesoporous NiO nanostructures on FTO substrates.[10] Zhao et al. reported the formation of NiO micro/nanoflowers by a hydrothermal route and analysed the role of different concentrations of potassium persulfate, which was acting as a structure-directing agent.[20] Ci et al. prepared NiO hollow microspheres through a solvothermal method using ethanol and water mixture as a mixed solvent in the presence of sodium dodecyl sulfate.[24] However, the challenge is to synthesize NiO with high surface area, which is one of the key factors for electrochemical applications.

In this work, we obtained a glucose-based facile hydrothermal route for the synthesis of NiO multi-shelled hollow microspheres (NiO MS-HMS). Another sample with flake-like morphology, namely NiO microflakes (NiO MF), was synthesized under similar hydrothermal conditions but in absence of glucose. The morphologies of these materials are highly correlated with the charge transfer kinetics which affects their electrochemical properties. Herein, we have studied the potential of both NiO samples as electrochromic materials in detail. As electrochromic electrodes, NiO MS-HMS sample manifests better performances in terms of higher optical modulation, coloration efficiency and faster switching times. Hence, it was further used in the fabrication of the polymer gel electrolyte based smart window prototype.

2.2 Experimental section

2.2.1 Materials and chemicals

Nickel nitrate ($\text{Ni}(\text{NO}_3)_2 \cdot 6\text{H}_2\text{O}$), D-(+)-glucose, and urea ($\text{CO}(\text{NH}_2)_2$) were obtained from Merck. Transparent $\text{SnO}_2:\text{F}$ (FTO)-coated glass substrates (sheet resistance 15 Ω/sq) were purchased from Sigma-Aldrich. Acrylamide ($\text{CH}_2\text{CHCONH}_2$), bis-acrylamide ($\text{C}_7\text{H}_{10}\text{N}_2\text{O}_2$), and ammonium persulfate ($(\text{NH}_4)_2\text{S}_2\text{O}_8$) were procured from Alfa Aesar. All the chemicals were of analytical grade and used without any further purification. FTO substrates were washed with soap solution, and later cleaned with water, acetone, and isopropanol respectively.

Throughout the experiment, milli-Q water (Millipore Direct Q3 system) was used for preparing all aqueous solutions.

2.2.2 Synthesis procedure of nickel oxide hollow microspheres

$\text{Ni}(\text{NO}_3)_2 \cdot 6\text{H}_2\text{O}$, urea, and glucose were dissolved in 80 mL of milli-Q water at a molar ratio of 1:3.7:1.5 and stirred vigorously to ensure proper mixing. The obtained solution was transferred to a 100-mL Teflon-lined stainless-steel autoclave and the subsequent hydrothermal reaction was kept in a vacuum oven at 160 °C for 24 h. After cooling to room temperature, the as-formed brown precipitate was collected by centrifugation and thoroughly washed with an ample amount of milli-Q water and dried in an oven at 60 °C. For the formation of NiO MS-HMS, the as-obtained precipitate was calcined at 400 °C in ambient atmosphere for 3 h. The same protocol was employed for the formation of the NiO MF but in the absence of glucose.

2.2.3 Fabrication of electrochromic electrodes

5 mg of NiO MS-HMS/NiO MF sample was dispersed in 5 mL of milli-Q water. A homogeneous suspension was obtained after 10 min of ultrasonic agitation. To fabricate electrodes, 600 μL of the as-prepared suspension were drop-casted on FTO for electrochromic applications. The films were kept in an oven at 80 °C for 3 h to ensure better adhesion of the films with the substrates.

2.2.4 Polymer gel electrolyte fabrication

Acrylamide (0.7 g) and bis-acrylamide (10.5 mg) were dissolved in milli-Q water (6.3 mL). The mixture was degassed for 10 mins, then ammonium persulfate (2.8 mg) was added to the precursor solution. Hence, the obtained colourless solution was heated at 80 °C until a constant weight was attained for the xerogel.[33] The xerogel was soaked in 1 M KOH solution for 12 h to allow for the bulging of the polymer matrix with the electrolyte. Thus, the obtained quasi-solid electrolyte was a colourless, transparent polymeric gel.

2.2.5 Sample characterizations and measurements

The morphology of the samples was investigated by a field emission scanning electron microscope (FESEM, Zeiss Ultra Plus) and a transmission electron microscope (TEM, JEOL JEM-2200FS operating at 220 kV). Powder X-ray diffraction measurement was conducted using a Bruker D8 Advanced X-ray diffractometer with $\text{CuK}\alpha$ radiation (1.54 Å). Raman spectroscopy was carried out in a LabRAMHR 800 (HORIBA Jobin Yvon) instrument, equipped with an Ar ion laser (532 nm) operating at 10% power. Adsorption measurement was

Chapter 2

performed using a Micromeritics 3-Flex pore and surface area analyser. Samples were evacuated under 10^{-4} – 10^{-5} Torr vacuum at 120 °C for 12 h. The electrochemical measurements were performed using the PARSTAT 2273 instrument. The FTO substrates prepared by drop-casting NiO MF/NiO MSHMS samples were used as the working electrodes; platinum mesh and Ag/AgCl/Cl⁻ electrode (saturated KCl) were used as counter and reference electrodes respectively. 1 M KOH solution was used as the electrolyte for electrochromic characterizations. Optical transmission spectra were recorded with a Shimadzu UV-3600 plus UV-Vis-NIR spectrophotometer.

Kinetics measurements for the electrochromic electrodes were performed by an automated, homebuilt system consisting of a quartz-tungsten-halogen (QTH) lamp from Newport, a monochromator (Princeton Instruments SP2500), a Si photodetector (FDS 1010), and a custom-made LabVIEW-controlled unit for data acquisition consisting of an LCR meter (Agilent E4980A), lock-in amplifier (SR850) and low-noise current preamplifier (SR570) attached to a computer system.

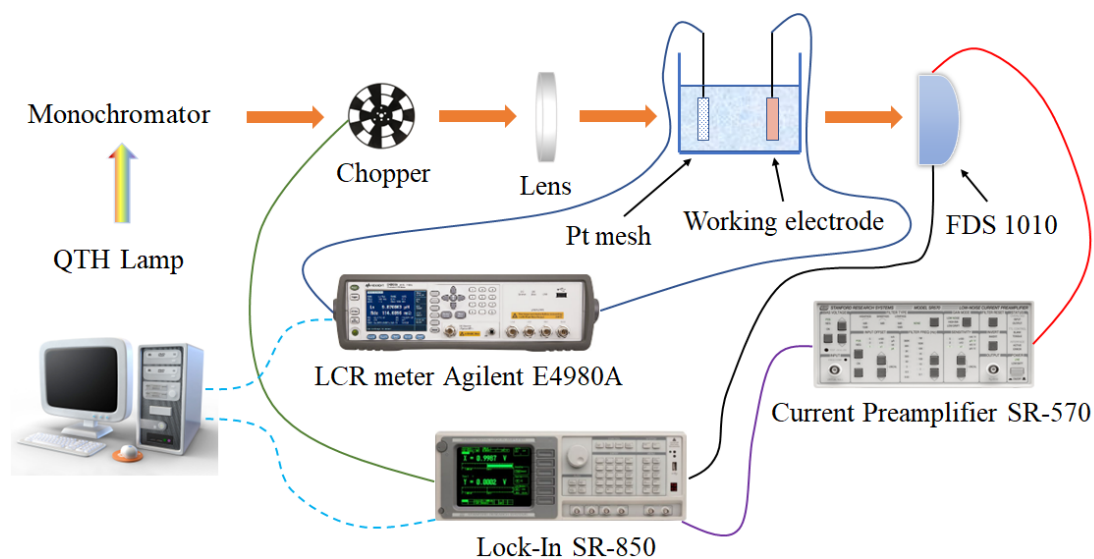


Figure 2.1: A sketch of the experimental set-up for doing kinetics measurement

The optical signal detection was performed using a lock-in based detection technique. Light of a particular wavelength was selected from a QTH white light source by passing it through a monochromator, to fall on the electrode. The potentials were applied to the platinum mesh and the working electrode by an LCR meter. Transmitted light intensity was detected using a Si photodiode. The generated photocurrent was amplified by a current preamplifier before its detection in Lock-in. Finally, the automated data acquisition was carried out using LabVIEW programming.

2.3 Results and discussions

2.3.1 Structure and morphology analysis

The crystal structure and phase purity were investigated by XRD. Figure 2.2a shows that all the observed diffraction peaks of NiO MF and NiO MS-HMS can be perfectly indexed to the face-centered cubic NiO phase (JCPDS no. 01-078-0643) diffraction peaks at 37.26° , 43.3° , 62.9° , 75.44° , and 79.43° , indexed as (111), (200), (220) (311), and (222) crystal planes NiO respectively. Raman data of the samples (Figure 2.2b) shows two peaks at 503 cm^{-1} and 1054 cm^{-1} , corresponding to the one phonon (LO) mode and two phonon (2LO) modes of NiO, respectively.[34]

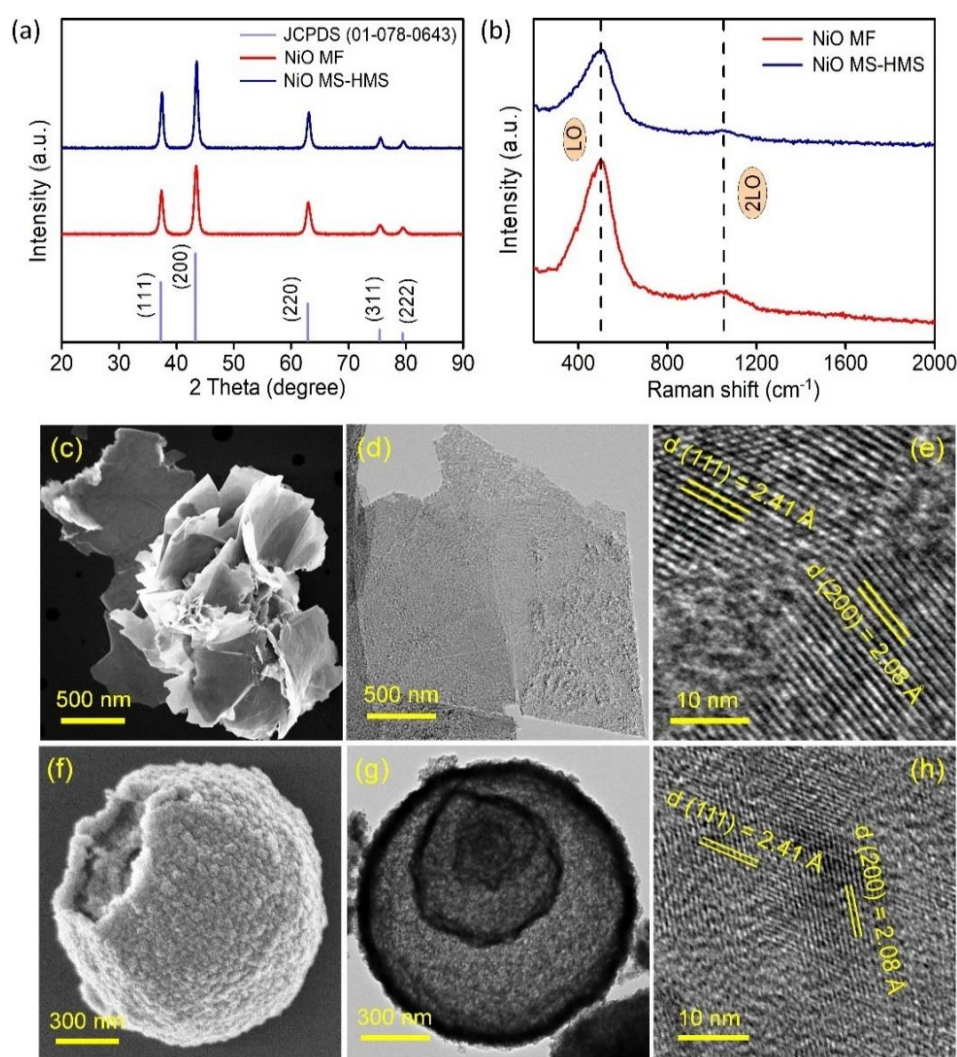


Figure 2.2: (a) XRD data and (b) Raman spectra of NiO MF and NiO MS-HMS samples; FESEM, TEM and HRTEM images of (c)-(e) NiO MF and (f)-(h) NiO MS-HMS samples

The morphology of the as-prepared samples was analysed by FESEM and TEM techniques (Figure 2.2c-h). As displayed in Figure 2.2c, the sample, synthesized in the absence

of glucose, has a flake-like morphology with an average size of $\sim 1\text{--}2\ \mu\text{m}$. The TEM image presented in Figure 2.2d confirms the flake-like morphology. On the other hand, the obtained NiO MS-HMS sample (Figure 2.2f) is mostly comprised of aggregated primary NiO nanoparticles, has diameter of $\sim 0.5\text{--}2\ \mu\text{m}$ and possesses a hollow interior with wall thickness of $\sim 70\text{--}80\ \text{nm}$. The presence of inner shells within the sphere is visible in the FESEM image and it is well-supported by its TEM image (Figure 2.2g), which clearly shows the presence of hollow interior and the inner shells with thickness of around $70\ \text{nm}$. The HRTEM images of NiO MF (Figure 2.2e) and NiO MS-HMS (Figure 2.2h) samples illustrate visible lattice fringes with the d spacings of about $2.08\ \text{\AA}$ and $2.41\ \text{\AA}$, corresponding to (200) and (111) lattice planes of the face-centered cubic NiO structure respectively.

2.3.2 Surface area measurement

Following this interesting morphology, surface area measurements were carried out for both of the samples. N_2 adsorption-desorption at $77\ \text{K}$ resulted in type III isotherm for both samples, shown in Figure 2.3a and 2.3d. The specific surface areas and total pore areas of NiO MF and NiO MS-HMS samples were $127.26\ \text{m}^2/\text{g}$ and $165.47\ \text{m}^2/\text{g}$ respectively, as obtained by Brunauer-Emmett-Teller (BET) fitting.

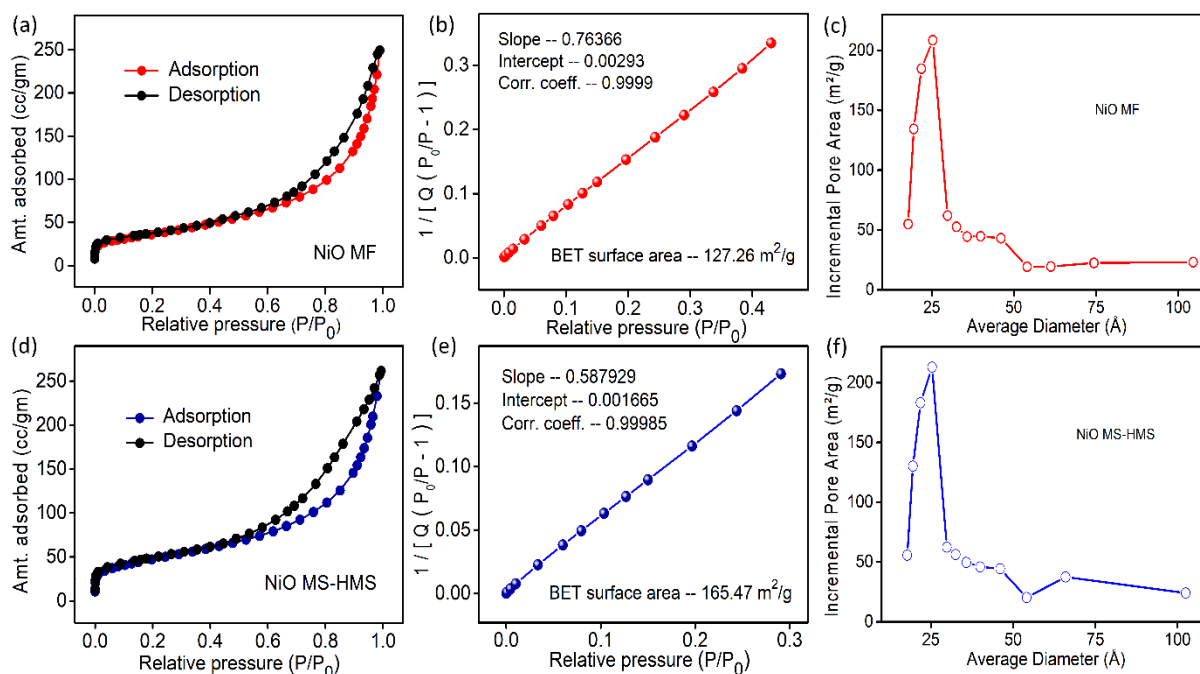


Figure 2.3: N_2 adsorption isotherms at $77\ \text{K}$, BET fitting data and pore size distribution data of (a)-(c) NiO MF and (d)-(f) NiO MS-HMS powder samples respectively

It can be seen from Figure 2.3c and Figure 2.3f that both of these two materials porosity distribution lie between $2\text{--}75\ \text{\AA}$. Although both materials have almost similar porosity

distributions; pore area corresponding to pore diameter 66 Å is higher in NiO MS-HMS sample and the total pore volume for NiO MS-HMS is 104.07 m²/gm, also higher than that of NiO MF, which has a total pore volume of 85.17 m²/gm. Thus, adequate differences in specific surface area and total pore area were observed, that affect the overall electrochromic performances.

2.3.3 Formation mechanism of NiO multi-shelled hollow microspheres

A multi-step process is involved in the formation of the NiO MS-HMS. A schematic illustration of the formation of the material is presented in Figure 2.4. Under hydrothermal conditions, the glucose present in the reaction undergoes polymerization followed by carbonization and finally ends up with the formation of carbon microspheres followed by a dehydration reaction. Dehydration takes place between the hydrophilic –OH and =C=O groups present on the surface of the carbon microspheres, formed by the non-dehydrated or incompletely dehydrated glucose and the nickel oxide hydrate, produced by the hydrolysis of a nickel precursor. This leads to the formation of Ni(OH)_x nuclei on top of the carbon microsphere—a core-shell structure. Urea facilitates the alkaline medium for the formation of Ni(OH)_x. At this point, the hydrophilic groups present on the newly formed structure again react with the –OH groups present in dehydrated and polymerized glucose preceding the formation of another shell of carbon on the exterior of the Ni(OH)_x layer. Further dehydration reaction between the hydrophilic groups present on this carbonaceous sphere and nickel oxide hydrate induces the evolution of a second Ni(OH)_x layer. Eventually, we get a multilayer growth of Ni(OH)_x and carbonaceous particles. During calcination, the carbon is combusted into CO₂, and the Ni(OH)_x is transformed to NiO. The carbonaceous sphere acts as a sacrificial template for the formation of multi-shelled hollow microspheres of NiO.[35, 36]

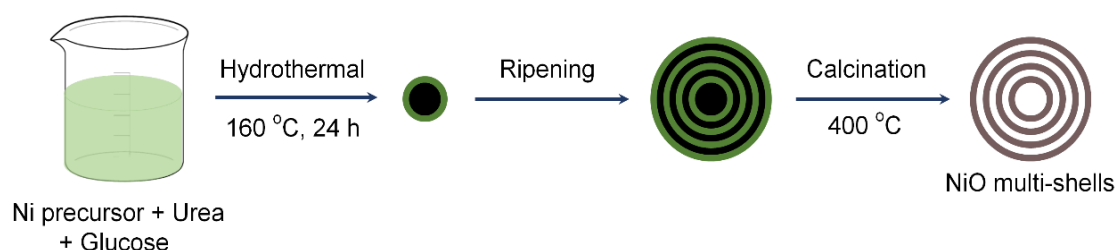


Figure 2.4: Schematic illustration of the formation mechanism of NiO MS-HMS using carbonaceous template

2.3.4 Electrochromic performances

The electrochromic properties of NiO electrodes were measured after they were subjected to a few cycles of cyclic voltammograms (CV) in 1 M KOH solution. CVs of the

samples at a scan rate of 100 mVps are presented in Figure 2.5. During the anodic and cathodic scan, intercalation and deintercalation of the OH⁻ ion lead to the oxidation and reduction of NiO and the oxidation states switch between Ni²⁺/Ni³⁺ and Ni³⁺/Ni²⁺ couples respectively.

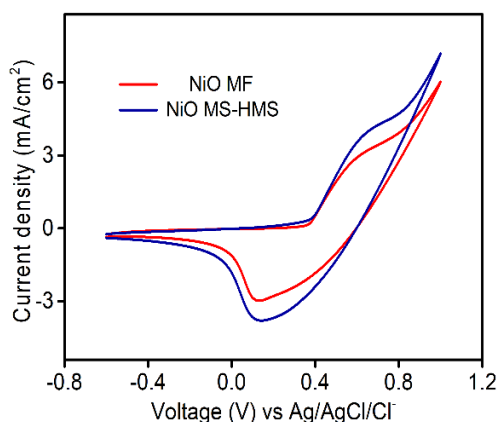


Figure 2.5: CVs of the samples in 1 M KOH at 100 mVps scan rate with Pt mesh as counter and Ag/AgCl/Cl⁻ as reference electrode

Thus, NiO can change its optical properties according to the following reaction [37] –



The coloration process is associated with the oxidation of the NiO layer and hence the formation of NiOOH. Similarly, the reduction of the NiOOH layer to NiO leads to the bleaching of the film.

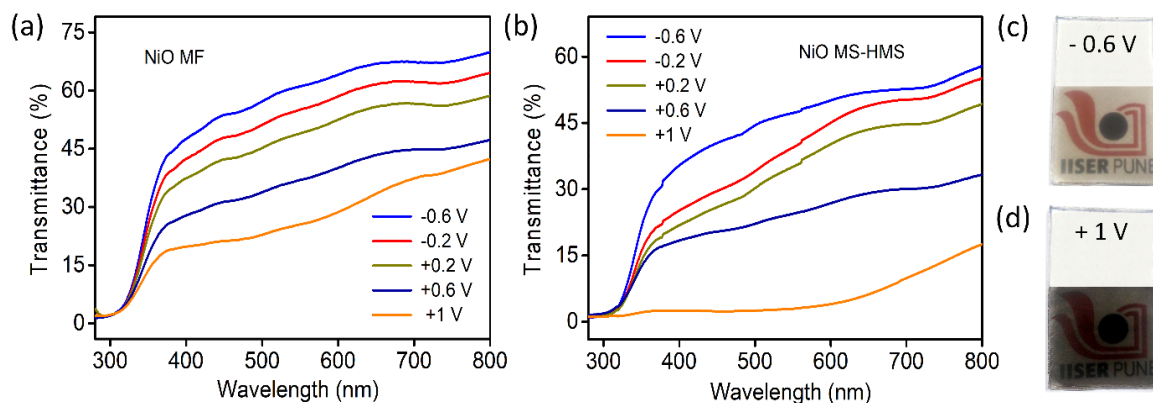


Figure 2.6: Transmission spectra of (a) NiO MF and (b) NiO MS-HMS films at different voltages; digital photographs of NiO MS-HMS film at its (c) bleached and (d) colored state

Ex-situ transmission measurement was performed within a wavelength range of 280–800 nm and a bias window of –0.6 V to +1 V. Transmission spectra of the samples under the application of different voltages are shown in Figure 2.6. Transmission modulation (defined as the difference between the colored and bleached state transmissions of an electrochromic film) reaches its maximum value of ~ 47% at 600 nm wavelength for NiO MS-HMS film (Figure

2.6b), which was significantly greater than that of the NiO MF film, which shows ~ 36% transmission modulation at 600 nm (Figure 2.6a). The films exhibit maximum coloration at the potential of +1 V (vs Ag/AgCl/Cl⁻) (dark brown) and it gets bleached at -0.6 V (vs Ag/AgCl/Cl⁻) (transparent). Photographs of a typical NiO MS-HMS film at its bleached and colored states are presented in Figure 2.6c-d.

Coloration efficiency (CE) for an electrochromic material is defined as the ratio of the change in optical density (ΔOD) and the intercalated charge per unit area of the film (Q), where change in optical density is given by $\Delta OD = \log(T_b/T_c)$; T_b and T_c denote the transmittance at the bleached and colored state of the films at a particular wavelength [38] ($\lambda = 600$ nm in this case). Estimated ΔOD of the NiO MS-HMS electrode is ~ 3.14 times greater than that of the other sample. Calculated CE for a NiO MS-HMS electrode at 600 nm is 85.3 cm²/C, which is significantly higher compared to the CE of NiO MF sample (36 cm²/C).

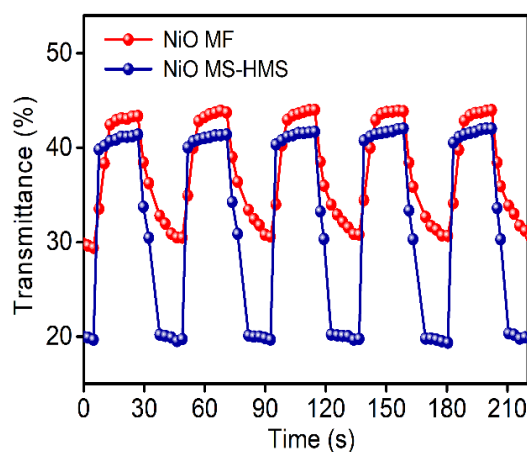


Figure 2.7: Switching response of the NiO MF and NiO MS-HMS films at 600 nm by applying +1 V and -0.6 V

Switching time is another crucial analytical property of electrochromic materials. It is the time, required to reach 90% of the total optical modulation.[39] For this measurement, optical transmission of the films at 600 nm was measured as a function of time by applying switching voltages between +1 V and -0.6 V (Figure 2.7). Coloration and bleaching response times for NiO MS-HMS are 6.7 sec and 2.7 sec, respectively, which are significantly faster than those of the NiO MF samples, which show a switching time of 12.7 sec and 6.1 sec. Larger specific surface area of NiO MS-HMS sample significantly increases the contact between the sample and the electrolyte which boosts ion intercalation and deintercalation in the material, leading to these faster temporal spectral responses under alternating potentials. Bleaching times are faster than the coloration times in transmission metal oxides, such as MoO₃, NiO, and WO₃

because, in bleaching cycle, the back emf (electromotive force) acts in the same direction of applied bias, and therefore a higher driving force is available for electron ejection.[40] In the present study, the coloration bleaching kinetic profile remains unchanged for many cycles. Our materials' electrochromic performances in terms of switching time (coloration and bleaching) and coloration efficiency (CE) are compared with the reported ones and presented in Table 2.1.

Table 2.1: Comparison of electrochromic performances of our samples with reported ones

Samples	Switching times (sec)		CE (cm ² /C)	References
	Coloration	Bleaching		
Porous NiO/RGO	7.2	6.7	76	Cai et al.[18]
Porous NiO	9.1	13.3	45	Cai et al.[18]
NiO _{4.75} film	-	-	23	Uplane et al.[19]
NiO nanoflake film	12.2	7.4	33.9	Cai et al.[41]
TiO ₂ /NiO core-shell nanorod array	6.8	14.8	60.6	Cai et al.[41]
Co-doped NiO nanoflake array	5.4	3.4	47.69	Zhang et al.[42]
NiO micro/nano flowers	1.3	3.2	49.8	Zhao et al.[20]
Electrodeposited NiO films	5.7	7.4	49	Browne et al.[43]
NiO MF	12.7	6.1	36	This work
NiO MS-HMS	6.7	2.7	85.3	This work

2.3.5 Electrochemical impedance analysis

The electrochemical impedance spectroscopy (EIS) further confirms that NiO MS-HMS is a better performer than NiO MF with quicker charge transfer kinetics. An EIS experiment was performed over a frequency range of 10 mHz to 20 kHz at an open circuit voltage superimposed with an AC voltage of 10 mV. Nyquist plots of the samples are (Figure 2.8) comprised of two partial semicircles; a small semicircle at high frequency is shown in the inset of Figure 2.8. The first point at the high frequency region is associated with the series resistance (R1) of the electrolytes and the electrical contact of the working electrode. The small semicircle at the high-frequency region is the characteristic of the charge transfer resistance (R2) at the electrolyte and counter electrode (Pt mesh) interface. The second semicircle corresponds to the charge transfer resistance (R3) at the working electrode and the electrolyte interface, which emerges due to the difference in conductivity between the sample (NiO

MF/NiO MS-HMS) and the aqueous electrolyte (KOH).[44] The obtained impedance spectra and the fitted parameters provided in Table 2.2 clearly show that the charge transfer resistance of NiO MS-HMS is significantly lower than that of NiO MF. The hollow structures of NiO MS-HMS provide a larger reaction surface that can accelerate the ion transport and hence possess lesser charge transfer resistance establishing the material as a better performer for electrochromic application.

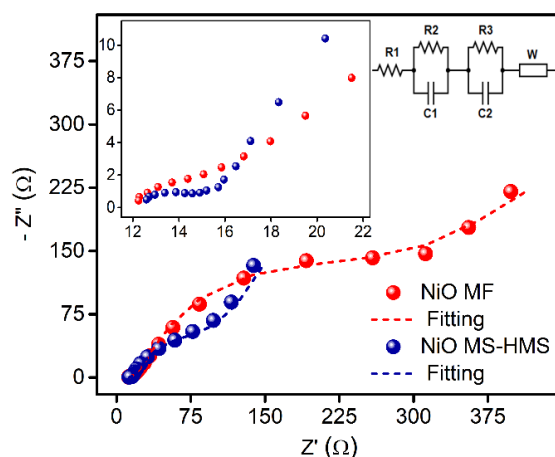


Figure 2.8: Electrochemical impedance spectra of the films in 1 M KOH (vs Ag/AgCl/Cl⁻)

Thus, we have utilized this material for fabricating a prototype for the electrochromic smart window with the aid of polymer gel electrolyte.

Table 2.2: Fitted circuit resistive elements for Electrochemical Impedance Spectra

Sample	R1 (Ω)	R2 (Ω)	R3 (Ω)
NiO MF	12.36	2.565	123.25
NiO MS-HMS	12.65	0.649	32.19

2.3.6 Prototype for electrochromic smart window

Synthesis of the gel electrolyte is described in the experimental section. Photograph of the 1 M KOH-based free-standing gel electrolyte is shown in Figure 2.9a. We have sandwiched the gel electrolyte between the NiO MS-HMS film and a transparent FTO, which acted as the counter electrode to assemble the quasi-solid-state electrochromic smart window. Figure 2.9b presents the schematic of the device. The photographs of the module at its bleached (-0.8 V) and colored state ($+1$ V) are illustrated in Figure 2.9c-d respectively.

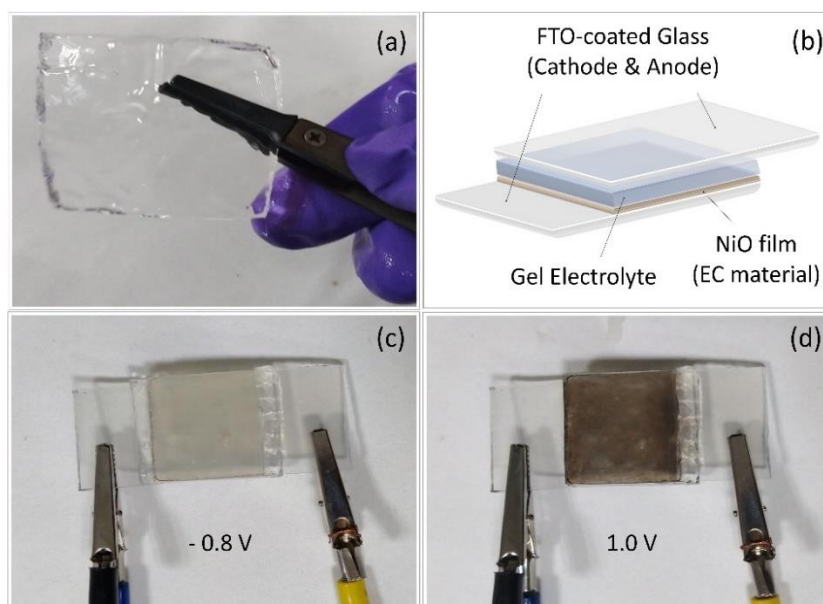


Figure 2.9: (a) Photograph of the free-standing gel-electrolyte, (b) schematic illustration of the device; photograph of the device at (c) -0.8 V and (d) $+1$ V applied potential

2.4 Conclusion

NiO MS-HMS was successfully synthesized by the glucose mediated hydrothermal reaction. The presence of glucose plays a key role in the formation of carbonaceous templates for the successive growth of multiple shells. As an electrode material for electrochromic application, NiO MS-HMS flaunts an all-round better performance in comparison to NiO MF. The morphology of NiO MS-HMS provides enhanced specific surface area for charge transfer reactions, which becomes highly beneficial for electrochemical applications. It presents superior electrochromic performances in terms of higher optical modulation, coloration efficiency and faster switching responses than that of NiO MF films. NiO MS-HMS electrode was further integrated into a quasi-solid-state electrochromic device, which displays a distinctive color change. In a nutshell, the material NiO MS-HMS, that we have synthesized in this work through a simple, cost-effective route, plays a crucial role in electrochromic applications with fast charge transfer kinetics, which makes it a competent candidate for electrochromic smart windows.

2.5 Bibliography

- [1] C.G. Granqvist, Handbook of inorganic electrochromic materials, Elsevier (1995).
- [2] N.S. Spinner, A. Palmieri, N. Beauregard, L. Zhang, J. Campanella, W.E. Mustain, Influence of conductivity on the capacity retention of NiO anodes in Li-ion batteries, *J. Power Sources*, 276 (2015) 46-53.
- [3] D. Mao, J. Yao, X. Lai, M. Yang, J. Du, D. Wang, Hierarchically Mesoporous Hematite Microspheres and Their Enhanced Formaldehyde-Sensing Properties, *Small*, 7 (2011) 578-582.
- [4] M.-Y. Cheng, Y.-S. Ye, T.-M. Chiu, C.-J. Pan, B.-J. Hwang, Size effect of nickel oxide for lithium ion battery anode, *J. Power Sources*, 253 (2014) 27-34.
- [5] G.H. Yue, Y.C. Zhao, C.G. Wang, X.X. Zhang, X.Q. Zhang, Q.S. Xie, Flower-like Nickel Oxide Nanocomposites Anode Materials for Excellent Performance Lithium-ion Batteries, *Electrochim. Acta*, 152 (2015) 315-322.
- [6] H. Liu, G. Wang, J. Liu, S. Qiao, H. Ahn, Highly ordered mesoporous NiO anode material for lithium ion batteries with an excellent electrochemical performance, *J. Mater. Chem.*, 21 (2011) 3046-3052.
- [7] I. Sohail, Z. Hussain, A.N. Khan, K. Yaqoob, Synthesis and characterization of electrodeposited NiO thin film on electrode grade carbon plate for supercapacitor applications, *Mater. Res. Express*, 4 (2017) 116412.
- [8] Z. Zhang, Q. Gao, H. Gao, Z. Shi, J. Wu, M. Zhi, Z. Hong, Nickel oxide aerogel for high performance supercapacitor electrodes, *RSC Adv.*, 6 (2016) 112620-112624.
- [9] S. Vijayakumar, S. Nagamuthu, G. Muralidharan, Supercapacitor Studies on NiO Nanoflakes Synthesized Through a Microwave Route, *ACS Appl. Mater. Interfaces*, 5 (2013) 2188-2196.
- [10] S. Mishra, P. Yogi, P.R. Sagdeo, R. Kumar, Mesoporous Nickel Oxide (NiO) Nanopetals for Ultrasensitive Glucose Sensing, *Nanoscale Res. Lett.*, 13 (2018) 16.
- [11] M.H. Raza, K. Movlaee, Y. Wu, S.M. El-Refaei, M. Karg, S.G. Leonardi, G. Neri, N. Pinna, Tuning the NiO Thin Film Morphology on Carbon Nanotubes by Atomic Layer Deposition for Enzyme-Free Glucose Sensing, *ChemElectroChem*, 6 (2019) 383-392.
- [12] S.M. El-Refaei, M.M. Saleh, M.I. Awad, Tolerance of glucose electrocatalytic oxidation on NiO_x/MnO_x/GC electrode to poisoning by halides, *J. Solid State Electrochem.*, 18 (2014) 5-12.

- [13] D.S. Dalavi, R.S. Devan, R.S. Patil, Y.-R. Ma, M.-G. Kang, J.-H. Kim, P.S. Patil, Electrochromic properties of dandelion flower like nickel oxide thin films, *J. Mater. Chem. A*, 1 (2013) 1035-1039.
- [14] Y. Chen, Y. Wang, P. Sun, P. Yang, L. Du, W. Mai, Nickel oxide nanoflake-based bifunctional glass electrodes with superior cyclic stability for energy storage and electrochromic applications, *J. Mater. Chem. A*, 3 (2015) 20614-20618.
- [15] F. Lin, D. Nordlund, T.-C. Weng, R.G. Moore, D.T. Gillaspie, A.C. Dillon, R.M. Richards, C. Engtrakul, Hole Doping in Al-Containing Nickel Oxide Materials To Improve Electrochromic Performance, *ACS Appl. Mater. Interfaces*, 5 (2013) 301-309.
- [16] F. Lin, D. Nordlund, T.-C. Weng, D. Sokaras, K.M. Jones, R.B. Reed, D.T. Gillaspie, D.G.J. Weir, R.G. Moore, A.C. Dillon, R.M. Richards, C. Engtrakul, Origin of Electrochromism in High-Performing Nanocomposite Nickel Oxide, *ACS Appl. Mater. Interfaces*, 5 (2013) 3643-3649.
- [17] Q. Liu, Q. Chen, Q. Zhang, Y. Xiao, X. Zhong, G. Dong, M.-P. Delplancke-Ogletree, H. Terryn, K. Baert, F. Reniers, X. Diao, In situ electrochromic efficiency of a nickel oxide thin film: origin of electrochemical process and electrochromic degradation, *J. Mater. Chem. C*, 6 (2018) 646-653.
- [18] G.-f. Cai, J.-p. Tu, J. Zhang, Y.-j. Mai, Y. Lu, C.-d. Gu, X.-l. Wang, An efficient route to a porous NiO/reduced graphene oxide hybrid film with highly improved electrochromic properties, *Nanoscale*, 4 (2012) 5724-5730.
- [19] M.M. Uplane, S.H. Mujawar, A.I. Inamdar, P.S. Shinde, A.C. Sonavane, P.S. Patil, Structural, optical and electrochromic properties of nickel oxide thin films grown from electrodeposited nickel sulphide, *Appl. Surf. Sci.*, 253 (2007) 9365-9371.
- [20] C. Zhao, F. Du, J. Wang, Flower-like nickel oxide micro/nanostructures: synthesis and enhanced electrochromic properties, *RSC Adv.*, 5 (2015) 38706-38711.
- [21] M.Z. Sialvi, R.J. Mortimer, G.D. Wilcox, A.M. Teridi, T.S. Varley, K.G.U. Wijyantha, C.A. Kirk, Electrochromic and Colorimetric Properties of Nickel(II) Oxide Thin Films Prepared by Aerosol-Assisted Chemical Vapor Deposition, *ACS Appl. Mater. Interfaces*, 5 (2013) 5675-5682.
- [22] H. Xiao, S. Yao, H. Liu, F. Qu, X. Zhang, X. Wu, NiO nanosheet assembles for supercapacitor electrode materials, *Prog. Nat. Sci: Mater. Int.*, 26 (2016) 271-275.
- [23] N. Liu, J. Li, W. Ma, W. Liu, Y. Shi, J. Tao, X. Zhang, J. Su, L. Li, Y. Gao, Ultrathin and Lightweight 3D Free-Standing Ni@NiO Nanowire Membrane Electrode for a Supercapacitor

with Excellent Capacitance Retention at High Rates, *ACS Appl. Mater. Interfaces*, 6 (2014) 13627-13634.

[24] S. Ci, T. Huang, Z. Wen, S. Cui, S. Mao, D.A. Steeber, J. Chen, Nickel oxide hollow microsphere for non-enzyme glucose detection, *Biosens. Bioelectron.*, 54 (2014) 251-257.

[25] N.N.M. Zorkipli, N.H.M. Kaus, A.A. Mohamad, Synthesis of NiO Nanoparticles through Sol-gel Method, *Procedia Chem.*, 19 (2016) 626-631.

[26] F.L. Zhu, Y.S. Meng, Preparation and Characterization of NiO Nanowires via Single-Phase Precipitation, *Adv. Mater. Res.*, 668 (2013) 331-334.

[27] B.R. Cruz-Ortiz, M.A. Garcia-Lobato, E.R. Larios-Durán, E.M. Múzquiz-Ramos, J.C. Ballesteros-Pacheco, Potentiostatic electrodeposition of nanostructured NiO thin films for their application as electrocatalyst, *J. Electroanal. Chem.*, 772 (2016) 38-45.

[28] M.L. Huang, C.D. Gu, X. Ge, X.L. Wang, J.P. Tu, NiO nanoflakes grown on porous graphene frameworks as advanced electrochemical pseudocapacitor materials, *J. Power Sources*, 259 (2014) 98-105.

[29] S.S. Nkosi, B. Yalisi, D.E. Motaung, J. Keartland, E. Sideras-Haddad, A. Forbes, B.W. Mwakikunga, Antiferromagnetic–paramagnetic state transition of NiO synthesized by pulsed laser deposition, *Appl. Surf. Sci.*, 265 (2013) 860-864.

[30] H. Chai, X. Chen, D. Jia, S. Bao, W. Zhou, Flower-like NiO structures: Controlled hydrothermal synthesis and electrochemical characteristic, *Mater. Res. Bull.*, 47 (2012) 3947-3951.

[31] Y. Jiang, Z. Jia, W. Zhang, H. Suo, In Situ Hydrothermal Synthesis of Nickel Oxide Nanostructures by Thermal Decomposition and its Electrochemical Property, *J. Inorg. Organomet. Polym. Mater.*, 23 (2013) 1043-1047.

[32] S. Safa, R. Hejazi, M. Rabbani, R. Azimirad, Hydrothermal synthesis of NiO nanostructures for photodegradation of 4-nitrophenol, *Desalin. Water Treat.*, 57 (2016) 21982-21989.

[33] R. Narayanan, M. Deepa, A.K. Srivastava, Förster resonance energy transfer and carbon dots enhance light harvesting in a solid-state quantum dot solar cell, *J. Mater. Chem. A*, 1 (2013) 3907-3918.

[34] G. Anandha Babu, G. Ravi, T. Mahalingam, M. Kumaresavanji, Y. Hayakawa, Influence of microwave power on the preparation of NiO nanoflakes for enhanced magnetic and supercapacitor applications, *Dalton Trans.*, 44 (2015) 4485-4497.

- [35] H. Wu, Y. Wang, C. Zheng, J. Zhu, G. Wu, X. Li, Multi-shelled NiO hollow spheres: Easy hydrothermal synthesis and lithium storage performances, *J. Alloys Compd.*, 685 (2016) 8-14.
- [36] L. Chu, M. Li, Z. Wan, L. Ding, D. Song, S. Dou, J. Chen, Y. Wang, Morphology control and fabrication of multi-shelled NiO spheres by tuning the pH value via a hydrothermal process, *CrystEngComm*, 16 (2014) 11096-11101.
- [37] K.K. Purushothaman, G. Muralidharan, The effect of annealing temperature on the electrochromic properties of nanostructured NiO films, *Sol. Energy Mater. Sol. Cells*, 93 (2009) 1195-1201.
- [38] Y. Lu, L. Liu, D. Mandler, P.S. Lee, High switching speed and coloration efficiency of titanium-doped vanadium oxide thin film electrochromic devices, *J. Mater. Chem. C*, 1 (2013) 7380-7386.
- [39] Q. Huang, S. Cao, Y. Liu, Y. Liang, J. Guo, R. Zeng, J. Zhao, B. Zou, Boosting the Zn²⁺-based electrochromic properties of tungsten oxide through morphology control, *Sol. Energy Mater. Sol. Cells*, 220 (2021) 110853.
- [40] R. Narayanan, A. Dewan, D. Chakraborty, Complimentary effects of annealing temperature on optimal tuning of functionalized carbon–V₂O₅ hybrid nanobelts for targeted dual applications in electrochromic and supercapacitor devices, *RSC Adv.*, 8 (2018) 8596-8606.
- [41] G. Cai, J. Tu, D. Zhou, L. Li, J. Zhang, X. Wang, C. Gu, Constructed TiO₂/NiO Core/Shell Nanorod Array for Efficient Electrochromic Application, *J. Phys. Chem. C*, 118 (2014) 6690-6696.
- [42] J.-h. Zhang, G.-f. Cai, D. Zhou, H. Tang, X.-l. Wang, C.-d. Gu, J.-p. Tu, Co-doped NiO nanoflake array films with enhanced electrochromic properties, *J. Mater. Chem. C*, 2 (2014) 7013-7021.
- [43] M.P. Browne, H. Nolan, N.C. Berner, G.S. Duesberg, P.E. Colavita, M.E.G. Lyons, Electrochromic nickel oxide films for smart window applications, *Int. J. Electrochem. Sci*, 11 (2016) 6636-6647.
- [44] L. Tao, Z. Huo, Y. Ding, Y. Li, S. Dai, L. Wang, J. Zhu, X. Pan, B. Zhang, J. Yao, M.K. Nazeeruddin, M. Grätzel, High-efficiency and stable quasi-solid-state dye-sensitized solar cell based on low molecular mass organogelator electrolyte, *J. Mater. Chem. A*, 3 (2015) 2344-2352.

Chapter 3

*A rechargeable Zn-NiO
electrochromic battery*

Declaration: The work has been published in the following journal:

ChemElectroChem, 9, e202200001 (2022). Copyright. Wiley-VCH.

- **Abstract**

In this era of intelligent automation, smart energy storage devices are highly sought after due to their capability to reveal their state of charge by a visual color change. In principle, this is typically obtained by integrating electrochromic materials which demonstrate a change in optical band gap during redox reactions as electrodes in batteries/supercapacitors. In this work, metal organic framework (MOF) derived carbon embedded NiO (NiO@C) has been used as the electrochromic material which demonstrates high coloration efficiency and very fast switching speeds between its chromatic states compared to the previous work based on NiO multi-shelled hollow microspheres. Here, carbon embedded porous structure improves the charge transfer kinetics of NiO significantly and makes MOF-derived NiO@C a potential candidate to be integrated as a smart positive electrode in an alkaline zinc (Zn) battery to construct a rechargeable Zn-NiO electrochromic battery, which visually displays its energy storage level by changing its color from dark brown (charged state) to colorless (discharged state), making it a potential candidate for smart window and smart energy storage applications.

3.1. Introduction

Currently, the most studied electrochromic materials include organic molecules such as viologens, conducting polymers, Prussian Blue and transition metal oxides (TMO). Among TMOs, nickel oxide (NiO) is comprehensively studied because of its high theoretical capacity, natural abundance and low structural deformation.[1, 2] Yet, NiO-based electrodes suffer from poor electrochemical performances such as slower switching times, low conductivity, low coloration efficiency etc. So, it's required to effectively develop NiO material with higher electrical conductivity with faster ion diffusion kinetics. Carbonaceous materials like reduced graphene oxide, carbon nanotubes incorporated NiO have been already synthesized for improved electrochemical applications.[3, 4] Recently, in template-based synthesis, metal organic frameworks (MOF) have been used to synthesize NiO.[5, 6]

MOFs are a promising class of organic-inorganic hybrid crystalline materials, composed of metal ion centers and organic linkers with large structural and chemical diversities. These materials come up with very high surface area and tunable pore dimensions. A few MOFs with redox active organic ligands have been utilized as electrochromic materials.[7-9] Yet, the application of most of the MOFs is still limited in this field because of

their redox inactive nature. However, MOFs being crystalline in nature, possess a nice long range ordered structure with uniform pores. Thus, recently MOFs have been exploited as sacrificial templates to derive several carbon embedded transition metal-based nanostructures including NiO.[10-14]

In this work, an electrochromic rechargeable battery is presented to visually illustrate the feasibility of energy storage and retrieval in a single module. NiO based electrochromic devices and energy storage devices have highly alike working principle, which allows us to integrate both into a single platform. Carbon-embedded NiO samples (NiO@C) are prepared from a reported Ni-MOF in a subsequent 2-step pyrolysis process. Carbon embedded porous structure of the materials enables easier access to the active Faradaic sites and assists facile ion intercalation/deintercalation to ensure better all-round electrochemical performances. NiO electrodes are prepared on transparent conducting FTO substrates in a binder-free spray coating technique. The electrochromic characterizations of the synthesized materials are performed thoroughly in an alkaline medium of 1 M KOH in a three-electrode set-up. This MOF-derived NiO@C is introduced as a positive electrode material to fabricate an economically viable smart Zn-NiO battery by incorporating a mixed alkaline electrolyte system consisting of 1 M KOH and 10 mM ZnAc₂. To the best of our knowledge, this is the first report of a rechargeable Zn-NiO electrochromic battery.

3.2. Experimental section

3.2.1. Chemicals and materials

Nickel chloride (NiCl₂·6H₂O), p-benzenedicarboxylic acid (PTA), N,N-dimethylformamide (DMF), Zn foil, zinc acetate (ZnAc₂), potassium hydroxide (KOH) beads were procured from Alfa Aesar. Transparent SnO₂:F (FTO) coated glass substrates (sheet resistance 15 Ω sq⁻¹) were purchased from Sigma Aldrich. All the chemicals were of analytical grade and used as purchased. FTO substrates were cleansed with soap solution, and later washed with isopropanol, ethanol and copious amount of water respectively under ultrasonic treatment. Throughout the experiments, for the preparation of all aqueous solutions, reagent grade mili-Q water with 18.2 MΩ cm resistivity (Millipore Direct Q3 system) was used.

3.2.2. Material synthesis

Ni MOF was synthesized by a solvothermal reaction according to the report of Yang et al.[15] Typically, 166 mg of PTA was dissolved in 5 ml of DMF at room temperature under constant stirring. Then, 10 ml aqueous solution of NiCl₂·6H₂O (356.54 mg) was added to the

above solution very slowly. The mixture was then stirred for 1 h continuously, later transferred to a 40 ml teflon lined stainless steel autoclave and kept in an oven at 120°C for 24 h. After the reactor cooled down to room temperature, the precipitate was collected by centrifugation and washed with DMF and ethanol several times before drying the final product in air for 12 h at 70 °C to obtain the Ni-MOF powder. Based on the report of Liang et al,[16] a two-step pyrolysis procedure was followed to convert the MOF powder to NiO@C. Light green colour Ni-MOF powder was transferred to a ceramic crucible and kept in a tube furnace at 400 °C for 1 h under Ar-H₂ (97-3) gas flow, the heating rate was 5 °C min⁻¹. Afterwards, the sample was subjected to another heat treatment under air at the same temperature for different time durations (20 min, 35 min, 50 min) to obtain the desired products denoted as NiO@C_20, NiO@C_35 and NiO@C_50 respectively.

3.2.3. Preparation of NiO@C films on FTO

All films in this work were fabricated on FTO by spray coating technique. Prior to spray coating, spraying solutions were made by dispersing the samples in isopropanol and the substrates were masked with scotch tape to fix the area of the electroactive material. Then, the dispersion was sprayed on FTO kept at 70 °C on top of a hot plate with a commercially available airbrush (ANMSALES AB-130) using N₂ as a carrier gas at a constant pressure. The distance between the FTO and the airbrush nozzle was ~ 12 cm and the nozzle diameter of the airbrush was ~ 0.3 mm. After each spray, an appropriate time was given to dry the FTO.

3.2.4. Sample characterization and measurements

The morphology of the samples was observed by field emission scanning electron microscope (FESEM, Zeiss Ultra Plus) and transmission electron microscope (TEM, JEOL JEM-2200FS operating at 220 kV). Powder X-ray diffraction (XRD) patterns were recorded in Bruker D8 Advanced X-ray diffractometer with Cu K α radiation (1.54 Å). Raman spectroscopy was carried out in LabRAM HR 800 (HORIBA Jobin Yvon) instrument, equipped with a He-Ne Laser (632 nm) operating at 10% power. Thermogravimetric (TGA) and differential scanning calorimetry (DSC) analyses were performed in a Mettler Toledo TGA/DSC 1STARe system between 30 to 800 °C temperature in presence of air. X-ray photoelectron spectroscopy (XPS) measurements of V₂O₅ samples were carried out using monochromatic and micro-focused AlK α radiation with an energy of 1486.6 eV (Thermo Kalpha+ spectrometer). BET Surface area measurement was performed using Quantachrome NOVAtouch LX¹ instrument at liquid N₂ temperature (77 K). Prior to the measurement, all

samples were heated under vacuum at 100 °C for 12 h to remove impurities. The electrochemical measurements were performed using the CH instrument (CHI760E). For in-situ spectroelectrochemistry measurements, an Ocean Optics system comprised of a Deuterium-Halogen lightsource (DH-2000-BAL), optical fibers (200 μm core diameter) and a spectrometer (FLAME-T-XR1-ES) had been used. For all three-electrode measurements, FTO plates spray coated with NiO@C were used as working electrodes, platinum wire and Ag/AgCl/Cl⁻ (1 M KCl) were employed as the counter and reference electrodes respectively.

3.3. Results and discussions

3.3.1. Structural and morphological characterizations

Figure 3.1a shows that the XRD pattern of as synthesized Ni-MOF powder matches well with the reported simulated pattern (CCDC 638866).[15] Prior to the pyrolysis of the sample, thermal decomposition behaviour of Ni MOF was monitored through the TGA/DSC measurement presented in Figure 3.1b. Initial weight loss between 30-150 °C was primarily ascribed to the loss of solvated water molecules. The weight loss between 150-430 °C was assigned to the thermal decomposition of the Ni-MOF to yield NiO,[17] the strong endothermic peak at ~ 410 °C in the DSC curve indicates towards the rapid change in the material during the formation of NiO.

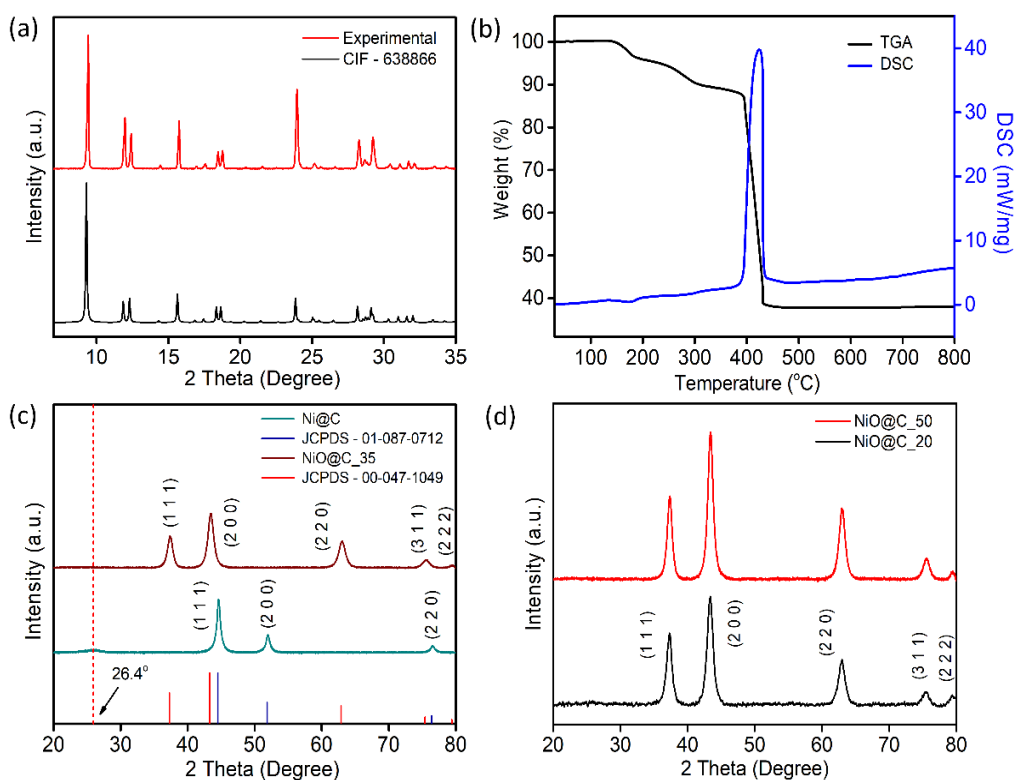


Figure 3.1: (a) XRD pattern of the as-synthesized Ni-MOF and the reported data of CIF – 638866, (b) TGA and DSC data of Ni MOF, (c) XRD pattern of the annealed samples, Ni@C and NiO@C_35, (d) XRD data of NiO@C_20 and NiO@C_50 samples

Figure 3.1c shows the XRD data of Ni@C (Ar-H₂ annealed sample, dark cyan graph) and the two-step annealed sample i.e., NiO@C_35 (wine red graph). The XRD pattern of Ni@C sample matches well with the JCPDS card no.- 01-087-0712. It confirms the presence of face centered cubic metallic Ni phase, along with a small hump at 26.4° in the data, showing the presence of graphitized carbon (corresponding to the (002) crystal plane) in the sample, generated due to the carbonization of the organic ligands. All the peaks belonging to MOF vanished after the pyrolysis. All the observed diffraction peaks of the twice annealed sample can be perfectly matched to the face centered cubic NiO phase (JCPDS no.- 01-047-1049), indicating a good crystallinity of the material. The diffraction peaks at 37.26°, 43.3°, 62.9°, 75.44°, and 79.43° corresponds to the (111), (200), (220), (311) and (222) crystal planes of NiO respectively. XRD patterns of the other two samples (NiO@C_20 and NiO@C_50) can be found in Figure 3.1d.

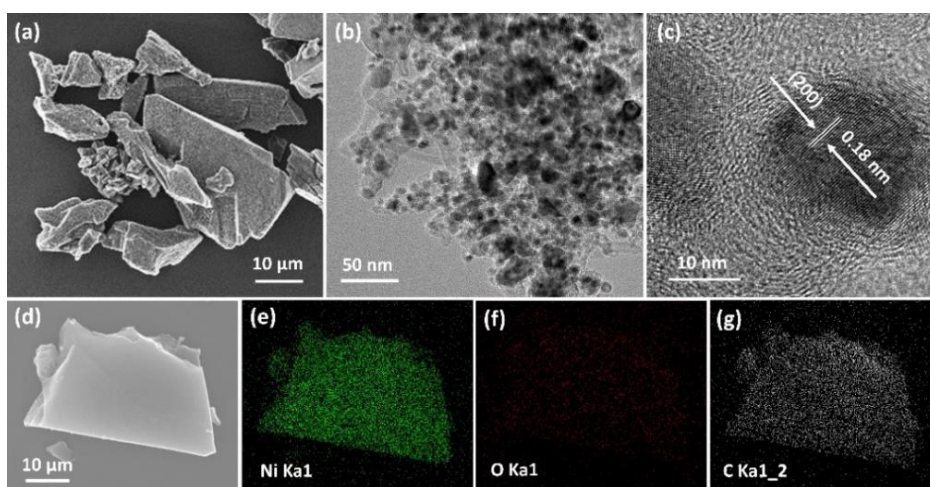


Figure 3.2: (a) SEM, (b) TEM, (c) HRTEM image and (d)-(g) the elemental mapping data for Ni@C sample

The morphological and structural characterizations of the materials were performed using SEM and TEM techniques. Carbon distributions over the samples were examined by energy dispersive X-ray (EDX) study. FESEM and TEM images presented in Figure 3.2a and 3.2b respectively, show the morphology of the Ar-H₂ annealed Ni@C sample. Porous structure of the sample with nickel (Ni) nanoparticles embedded in graphitized carbon layer is evident from the HRTEM image given in Figure 3.2c. It illustrates the lattice fringes with a spacing of 0.18 nm that corresponds to the crystal plane of Ni (200) and circular lattice fringes generated

from the graphitized carbon present in the sample. This is well supported by the EDX mapping data shown in Figure 3.2e-3.2g of Ni@C, where the region of interest is shown in Figure 3.2d.

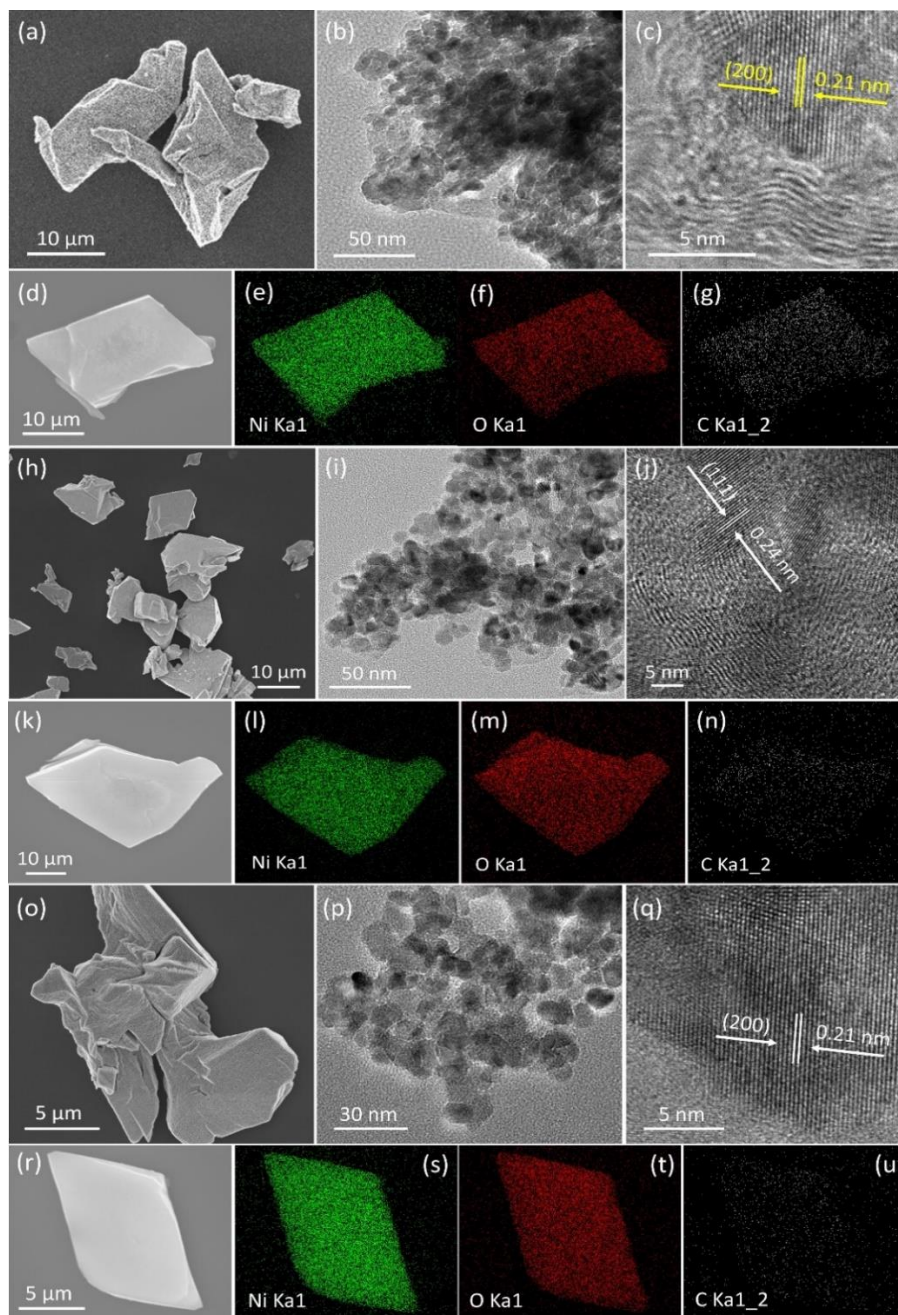


Figure 3.3: FESEM, TEM, HRTEM images and the elemental mapping images for NiO@C samples; (a)-(g) NiO@C₂₀, (h)-(n) NiO@C₃₅ and (o)-(u) NiO@C₅₀

Figure 3.3 shows the microstructures of NiO@C samples which are mainly composed of NiO nanoparticles. TEM images of these doubly annealed samples in Figure 3.3b, 3.3i and 3.3p illustrate that, NiO nanoparticles possess a particle size of ~ 10-20 nm. HRTEM images in Figure 3.3c, 3.3j and 3.3q exhibit the presence of typical lattice fringes with 0.21 nm and 0.24 nm spacings corresponding to (200) and (111) lattice planes of NiO, surrounded by

circular lattice fringes ($d = 0.34$ nm) of carbon. Existence of carbon in the samples is confirmed by the elemental mapping data (Figure 3.3e to 3.3g is of NiO@C₂₀, Figure 3.3l to 3.3n of NiO@C₃₅ and Figure 3.3s to 3.3u is of NiO@C₅₀) and it can be realized that with increasing annealing time gradually the carbon content in the sample decreases.

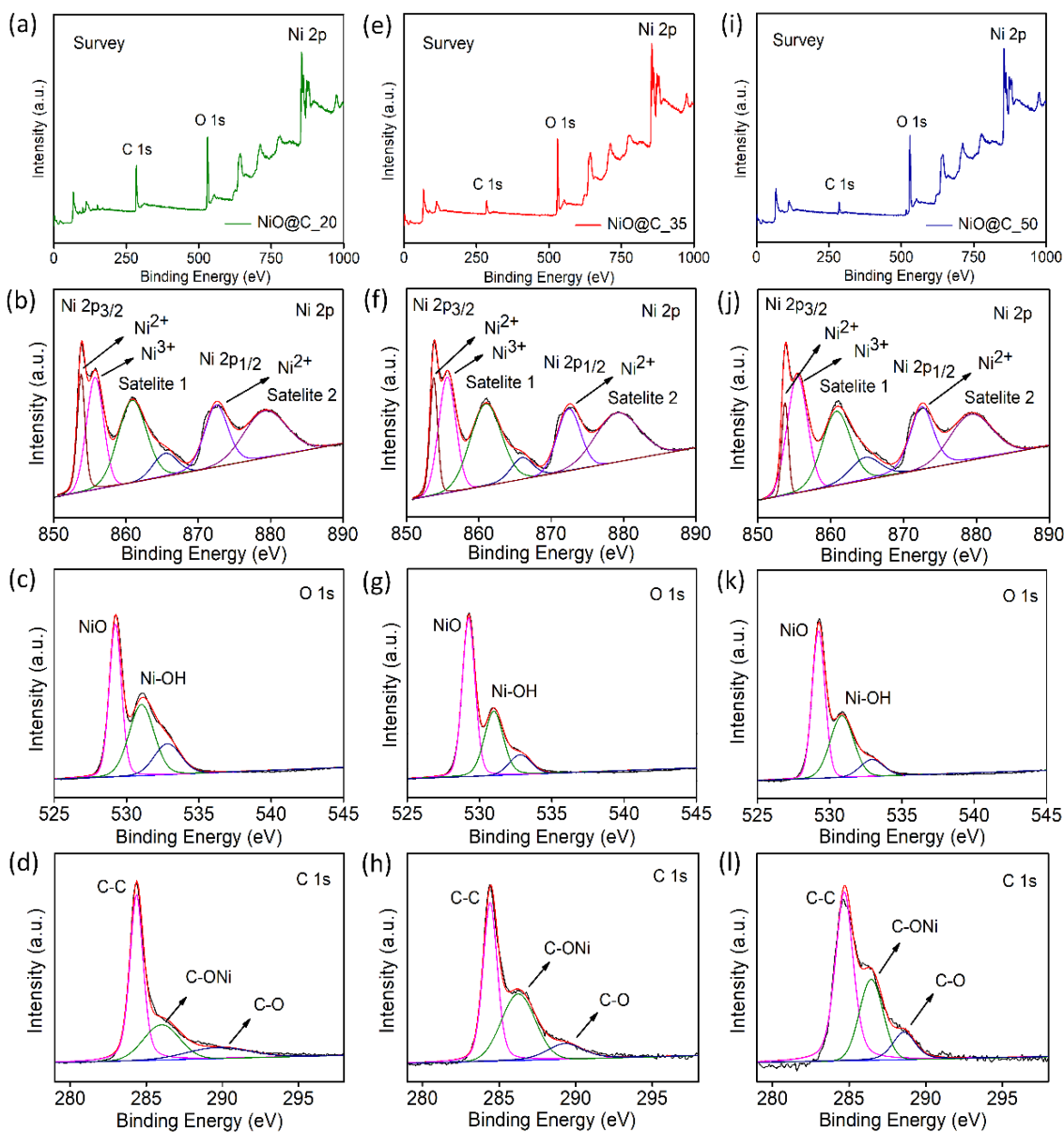


Figure 3.4: XPS data including survey spectrum and de-convoluted spectra for (a)-(d) NiO@C₂₀, (e)-(h) NiO@C₃₅ and (i)-(l) NiO@C₅₀ samples

To further investigate the phase and carbon content of the samples, X-ray photoelectron spectroscopy (XPS) measurements have been performed (Figure 3.4) on all NiO@C samples. High resolution data as presented in Figure 3.4b, 3.4f and 3.4j exhibit the Ni 2P_{3/2} peak which consists of the main peaks at 853.8 eV and 855.8 eV. The peak at 853.8 eV is assigned to the Ni²⁺ oxidation state, which is linked to the Ni-O octahedral bonding of cubic NiO structure.

The second peak at 855.8 eV corresponds to the Ni³⁺ state. The peak at 860.9 eV is related to shakeup processes (satellite peak) of NiO.[18] Similarly, 2P_{1/2} is also comprised of two peaks at 872.5 eV and 879.4 eV, which are related to the Ni²⁺ state and the satellite peak respectively.[19] The binding energy of O 1s spectra can be deconvoluted to 3 oxygen states (Figure 3.4c, 3.4g, 3.4k). The peaks at 529.2 eV, 531.1 eV and 532.9 eV correspond to Ni-O-Ni, Ni-OH and adsorbed water respectively.[18] High resolution C 1s spectrum consists of 3 peaks presented in Figure 3.4d, 3.4h and 3.4l. Peaks observed at 284.5 eV, 285.9 eV and 289.1 eV are assigned to C-C, C-ONi and C-O bonds respectively.[20] According to the XPS study, the carbon contents of NiO@C_20, NiO@C_35 and NiO@C_50 are 44.29%, 23.45% and 20.67% respectively.

3.3.2. Surface area measurements of the samples

Further, N₂ adsorption-desorption measurements at 77 K were performed to check the surface area and the pore size distributions for our NiO@C materials (Figure 3.5). According to IUPAC classification, all the materials show type IV isotherms with hysteresis loops in high

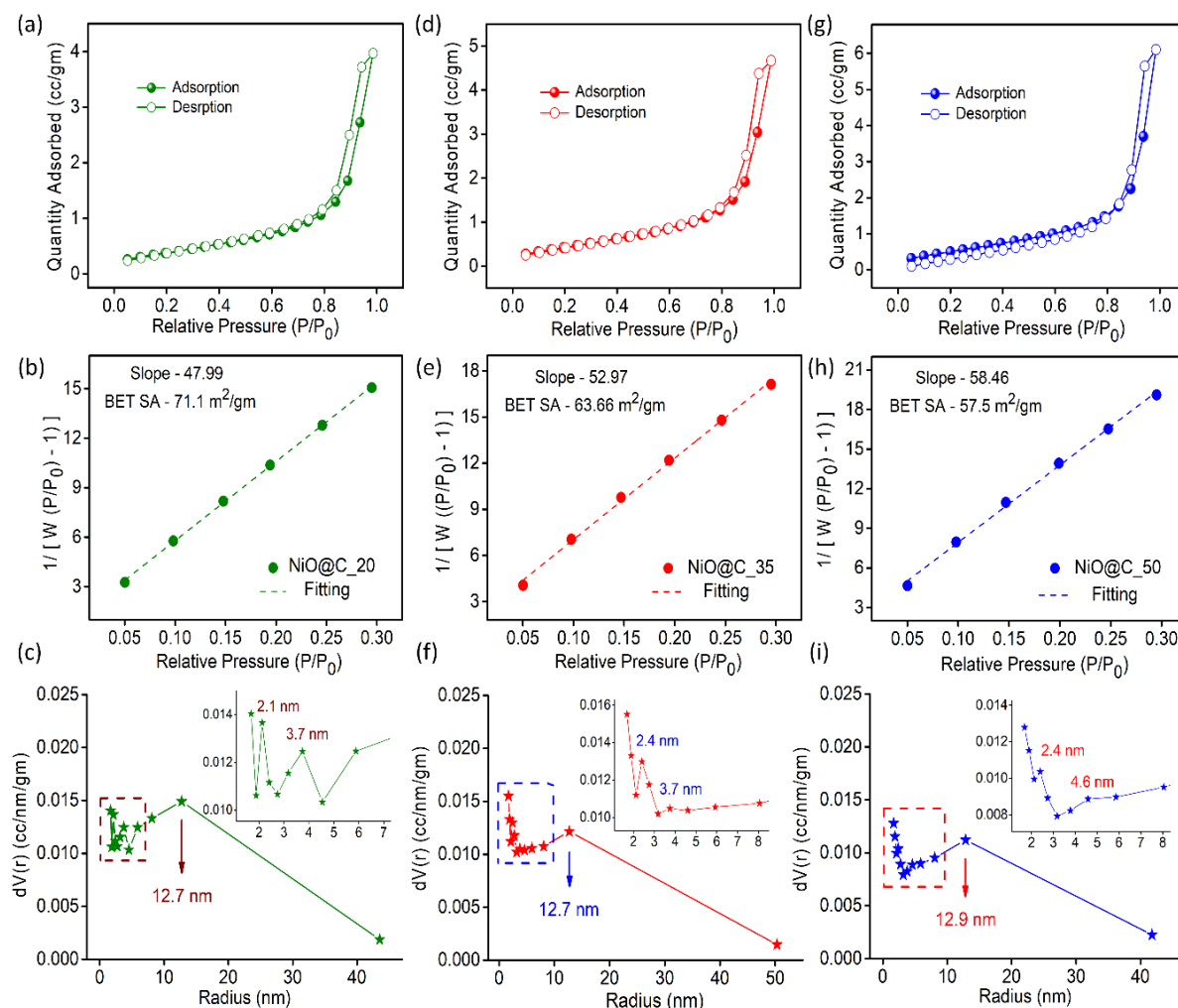


Figure 3.5: N₂ Adsorption desorption isotherms, BET fittings and BJH pore size distribution plots for (a)-(c) NiO@C_20, (d)-(f) NiO@C_35 and (g)-(i) NiO@C_50 respectively

relative pressure region (0.8-0.99) revealing the mesoporous nature of the samples as presented in Figure 3.5a-3.5c.[21] The Brunauer-Emmett-Teller (BET) surface areas are found to be 71.1, 63.66 and 57.5 m²/gm for NiO@C_20, NiO@C_35 and NiO@C_50 samples respectively (Figure 3.5d-3.5f). Barrett-Joyner-Halenda (BJH) method was used to calculate the pore size distributions of the samples. Interestingly, the increase in air annealing time (from 20 to 50 min) resulted in the decrease in specific surface area because of the increase in pore radius from 2.1 nm to 2.4 nm and gradually diminishing pore of radius 3.7 nm (Figure 3.5g-3.5i). Overall, the mesoporous structures of the samples allow faster ion exchange with electrolyte and favor good electrochemical performances.

3.3.3. Electrochromic studies

Electrochromic properties of all the samples were investigated with the help of the spectro-electrochemical technique via a three-electrode setup in presence of 1 M KOH as the electrolyte. Before going into the details of spectro-electrochemical data, let's understand the mechanism behind the colour state switching of NiO, which is attributed to the reversible change of Ni ions in between different valence states. Upon application of bias, the OH⁻ ions present in the KOH electrolyte either intercalates (during anodic scan) or deintercalates (during cathodic scan) which causes the oxidation or reduction reaction of the NiO material between Ni²⁺ and Ni³⁺ oxidation states, given by the following reaction[22]

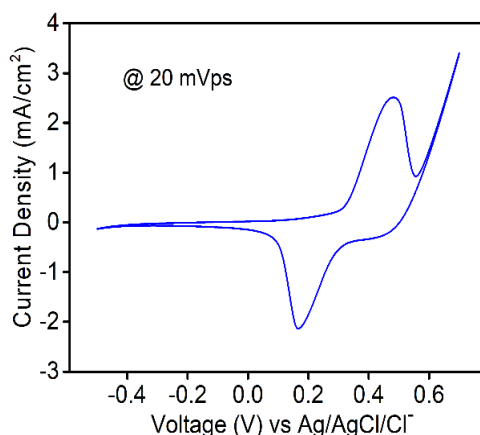


Figure 3.6: Cyclic voltammogram (CV) of NiO@C_35 electrode in three-electrode set-up at 20 mVps scan rate in 1 M KOH electrolyte

The obtained transmission spectra for all NiO@C samples (from 325 nm to 1000 nm) at the two extreme biases (vs Ag/AgCl/Cl⁻) were presented in Figure 3.7a-3.7c. The films reversibly change their colors from transparent (bleached at -0.5 V) to a dark brown state (colored at +0.7 V). Optical modulation (ΔT) is an important property for the electrochromic materials, given by $\Delta T = T_b(\lambda) - T_c(\lambda)$, where T_b and T_c are defined as the transmittances of the bleached and coloured states respectively at a certain wavelength. The blue curves in Figure 3.7a-3.7c present the optical modulation spectra for the NiO@C films. The graphs reveal that the highest ΔT values for the films can be obtained at ~ 525 nm and these are presented in a tabulated form in Table 1. The comparison of the transmittance values in coloured and bleached states along with the transmission modulation values for all 3 samples is presented in Figure 3.7d. With the increase in air annealing times, the gradual increment in the ΔT value can be noticed as a result of the decrease in carbon content in the samples.[16]

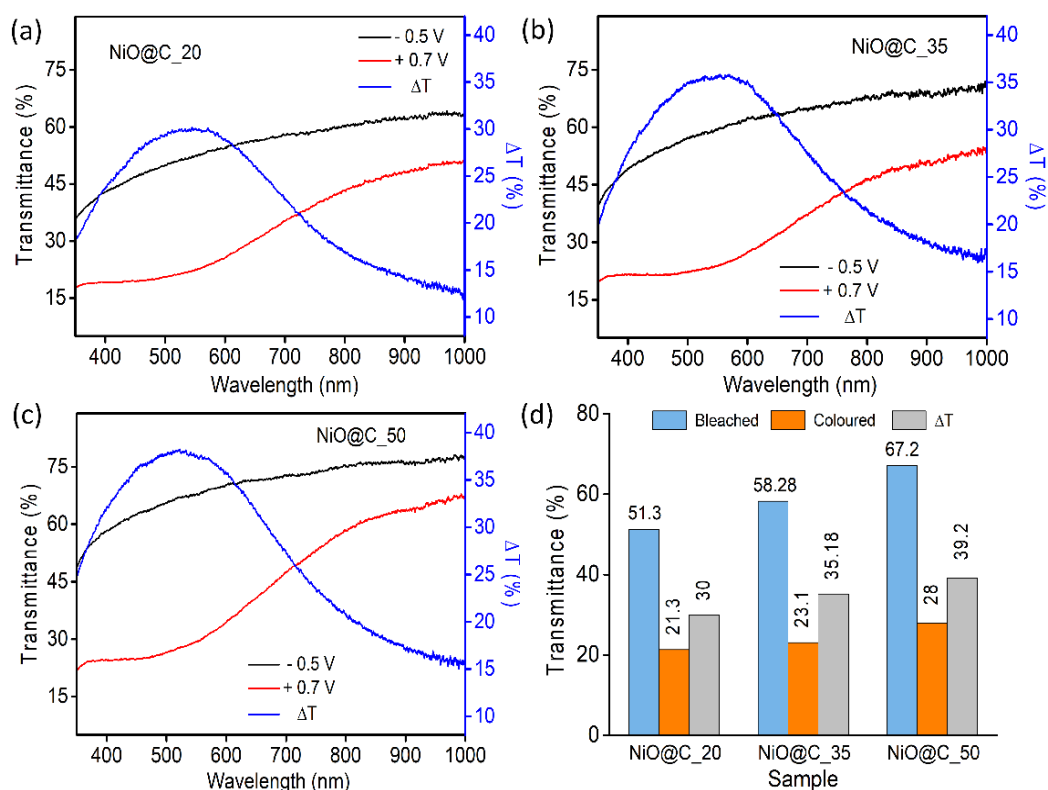


Figure 3.7: (a)-(c) Transmission spectra (coloured and bleached state) and the transmission modulation (ΔT) plots of NiO@C electrodes, (d) comparison of transmittance values (colored and bleached state) and optical modulation values at 525 nm wavelength

Cyclic voltammetry (CV) (solid lines) and in-situ transmittance measurements (dot-dashed lines) were performed for NiO@C_35 electrodes to check the modulation of optical response at a particular wavelength ($\lambda = 525$ nm) with the applied bias (Figure 3.8a). Digital

photographs of a typical NiO@C_35 film at colored and bleached states are also shown in Figure 3.8a. The transmittance of the film changes in a nice dynamical way, consistent with the change in current density. During anodic scan (indicated by blue solid arrow), intercalation of OH⁻ species results in the formation of NiOOH, which leads to the decrement in transmittance (blue dashed arrow) and just the reverse phenomenon occurs at the time of cathodic scan (black dashed arrow).

Figure 3.8b illustrates the temporal spectral response of the films under alternating potentials (-0.5 V and +0.7 V) at 525 nm. Switching time for the electrochromic materials is defined as the time required to achieve 90% of its full optical modulation.[23] Switching times for all the films, which are quite faster are presented in Table 1. Graphitized carbon present in the samples results in the faster response of the films, thus with increasing air annealing time the switching times also elongate as the carbons get oxidized with increase in annealing time. Interestingly here bleaching times for the films are relatively long compared to the coloration times. Two possible statements are there to explain this phenomenon – (a) while ion intercalation takes place, the possible lattice deformation tries to obstruct the movements of incoming ions, but the presence of carbon in the material tries to hasten the process up to a certain level, and (b) during deintercalation of ions, the built-in electric field at the interface works in the opposite direction of ionic movement, resulting the longer bleaching time.[24]

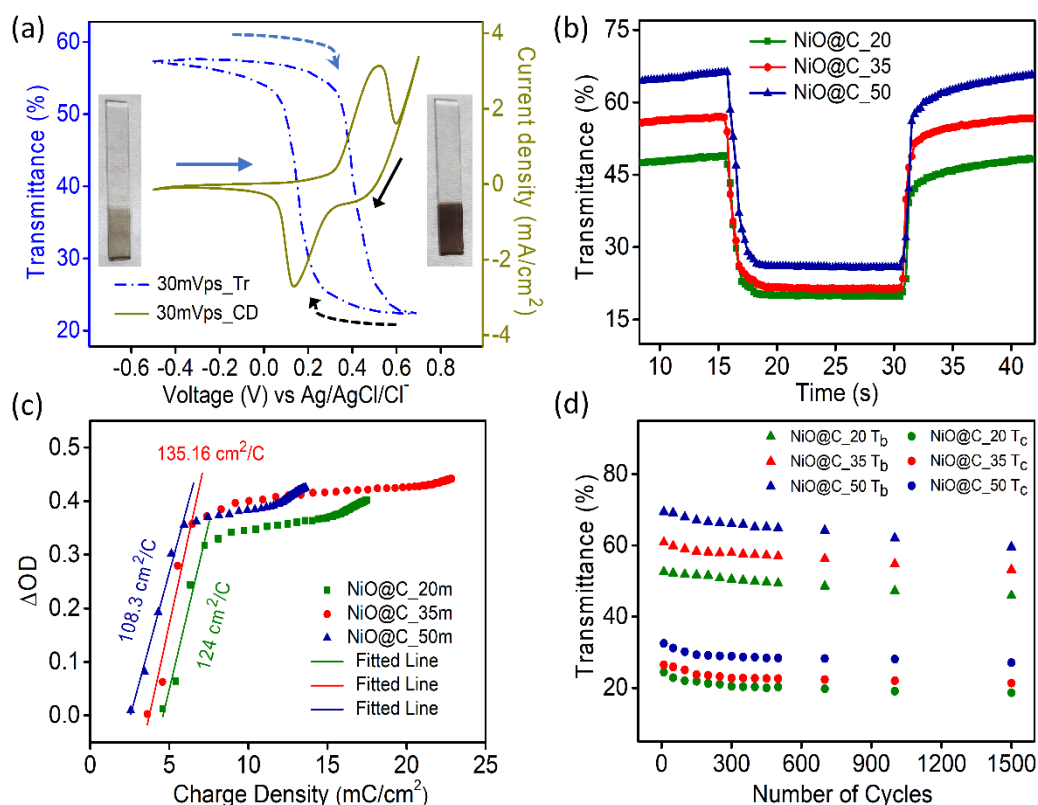


Figure 3.8: (a) CV (solid line) at 30 mVps along with the in-situ spectro-electrochemistry data (dashed line) at 525 nm, (b) switching time data upon application of alternatively with 15 s interval, (c) coloration efficiency plot, (d) stability of electrodes upon cycling

Coloration efficiency (CE) is yet another important analytical parameter for electrochromic materials which tells us about the requirement of power during electrochromic switching. It is defined as the ratio of change in optical density (ΔOD) and injected/extracted charge density per unit area (mC/cm^2). [25] CE can be calculated from the following formula –

$$CE = \log (T_b/T_c) / (Q/A)$$

In this work, CE values for the materials were calculated at $\lambda = 525$ nm from the slope of the ΔOD vs charge density graph, shown in Figure 3.8c. Obtained values are presented in Table 1 and the highest CE value of $135.16 \text{ cm}^2/C$ was obtained for NiO@C_35 films.

Stability measurement of the films is very crucial for electrochromic materials, it's a measure of the degradation of films upon cycling, which mainly depends on the ion trapping and operational conditions. Optical transmittances for all electrodes after certain cycles are presented in Figure 3.8d. Films retain nearly 90% (Table 1) of the initial optical modulation value even after 1500 cycles for NiO@C_20 and NiO@C_35 films. Retained performance after cycling is a little less ($\sim 85.5\%$) in case of NiO@C_50 films.

Table 3.1: Comparison of ΔT values, switching times, coloration efficiency and retained electrochromic performance after 1500 cycles for all the films

Films	ΔT (%) (at 525 nm)	Coloration Time (s)	Bleaching Time (s)	CE (cm^2/C)	Electrochromic stability retained after 1500 cycles
NiO@C_20	30	1.2	3.37	124	90.5%
NiO@C_35	35.18	1.4	3.48	135.16	90%
NiO@C_50	39.2	1.6	3.79	108.3	85.5%

3.3.4. Scan rate dependent cyclic voltammetry measurement

To check the current contributions introduced by Faradaic and non-Faradaic processes, CV at varying sweep rates from 10 to 70 mV/s were performed for all three different electrode materials, presented in Figure 3.9. The peak current densities of CV and the scan rate follow a power law relation, given by $i = av^b$; where, v is the scan rate and a , b are adjustable parameters, which are calculated from the linear plot of $\log(i)$ vs $\log(v)$. The value of the parameter b is 0.5 when the process is diffusion limited Faradaic process and when the process is originated from surface controlled non-diffusion related process, the b value is 1. In our cases, the obtained b

Chapter 3

values are close to 0.55, which specifies the overall process is mostly dominated by diffusion-controlled process. Thus, total current response (i), a combination of two quantities – a_1v and $a_2v^{1/2}$, which correspond to capacitive (electrical double layer capacitance and surface dominated pseudo capacitance) and diffusive processes respectively, can be expressed according to the following formula.[26] From the graph of $i/v^{1/2}$ vs $v^{1/2}$ for NiO@C_35 electrode, the coefficients a_1 and a_2 are calculated as shown in Figure 3.9e and the current responses are separated, as illustrated in the histogram plot in Figure 3.9f. The diffusion current contribution is seen to gradually decrease with increasing scan rate.

$$i = a_1v + a_2v^{1/2}$$

$$\text{or, } i/v^{1/2} = a_1v^{1/2} + a_2$$

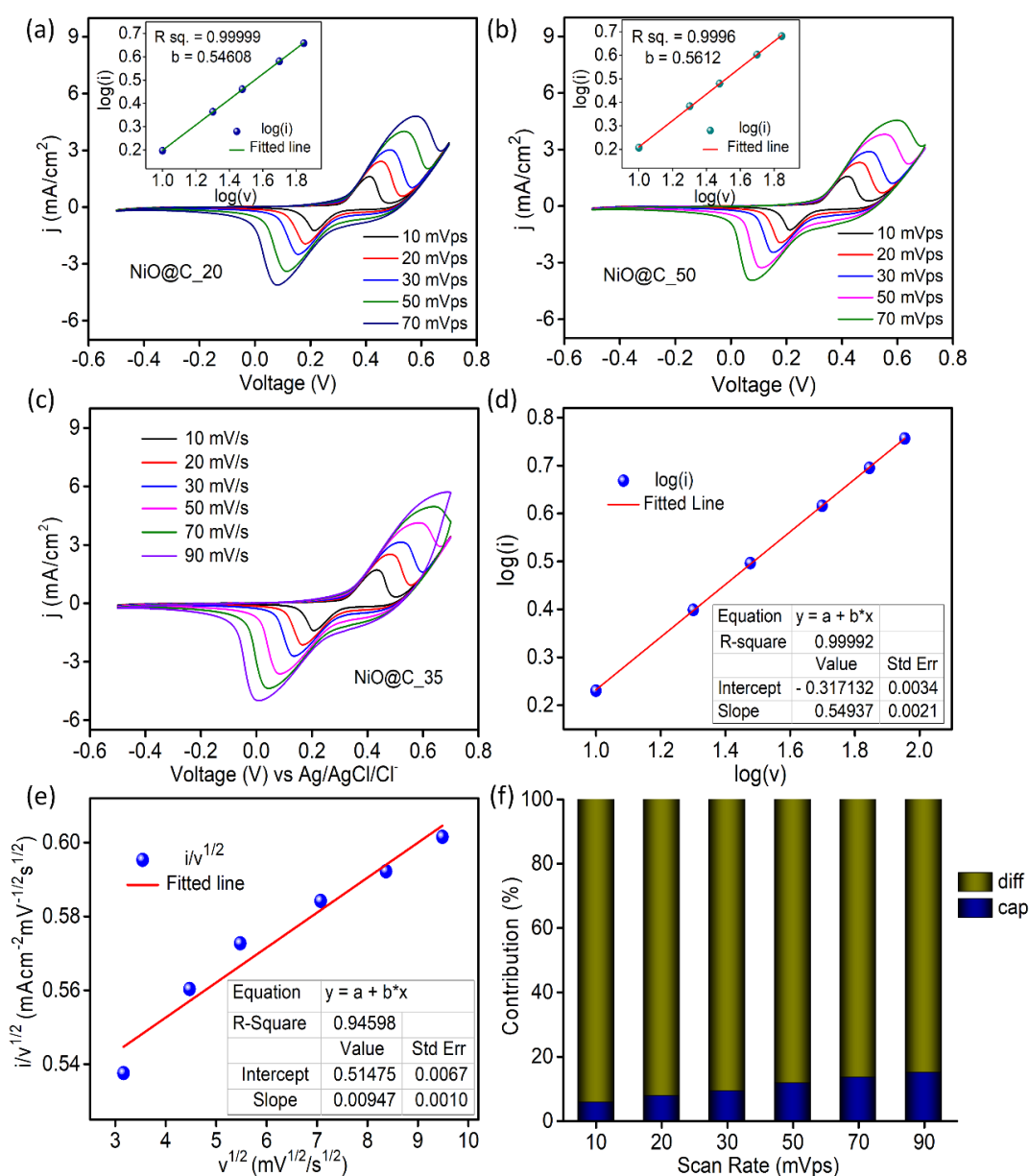


Figure 3.9: Scan rate dependent CV data and $\log(i)$ vs $\log(v)$ plots for (a) NiO@C_20, (b) NiO@C_50; data for NiO@C_35 sample (c) scan rate dependent CV data, (d) $\log(i)$ vs $\log(v)$ plot, (e) $i/v^{1/2}$ vs $v^{1/2}$ plot, (f) histogram plot to show current contributions with scan rate

3.3.5. Impedance measurements on NiO@C electrodes

Further, electrochemical impedance spectroscopy (EIS) measurements were carried out in a three-electrode system using 1 M KOH as electrolyte. Figure 3.10a presents the Nyquist plots and the fitted data for all the samples. Each plot consists of a semicircular part presented in the inset of Figure 3.10a, which is the high frequency-controlled region and the inclined line at low frequency arises due to the ionic diffusion.[27] Impedance data were fitted in ZSimpWin software using an equivalent circuit provided in Figure 3.10b, where R_s is the bulk/solution resistance, R_{ct} is the charge transfer resistance, C_{dl} is the double layer capacitance, W is the Warburg impedance related to ion diffusion process and Q represents the constant phase element. Larger radius of the semicircle refers to a higher R_{ct} value, and a steeper slope points towards a quicker ion-diffusion rate.[28] Lowest R_{ct} value of $21.5 \Omega\text{cm}^2$ was noticed for NiO@C_20. The electrochemical parameters are presented in the following Table 3.2. With the increase in air annealing time of the samples, carbon content gradually decreases, which is very consistent with the trend seen in charge transfer resistances.

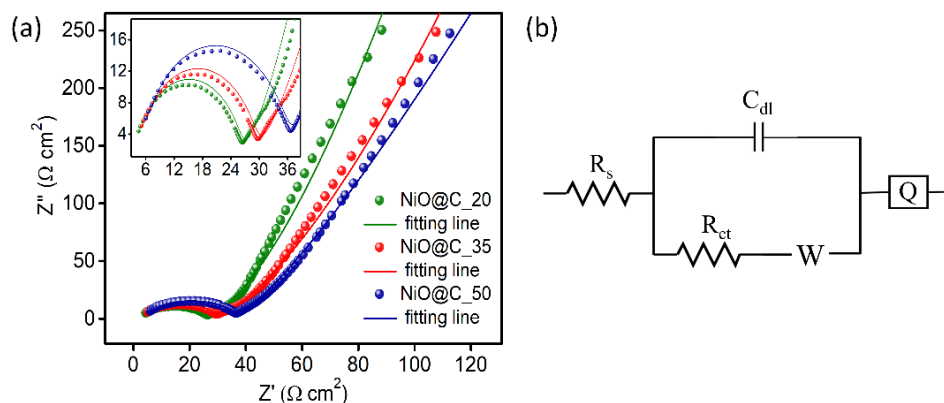


Figure 3.10: (a) EIS study (Nyquist diagrams) for all three NiO@C samples and (b) equivalent circuit diagram used for impedance data fitting

Table 3.2: Fitting parameters for impedance data for all three samples

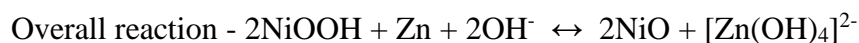
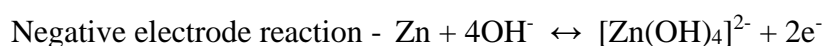
Films	R_s (Ωcm^2)	R_{ct} (Ωcm^2)	C_{dl} (F/ cm^2)	Measurement error (%)
NiO@C_20	4.091	21.5	5.923×10^{-8}	< 4.547
NiO@C_35	4.561	24.12	5.19×10^{-8}	< 4.226
NiO@C_50	5.331	29.81	4.378×10^{-8}	< 3.682

The overall superior performance of these MOF-derived NiO@C samples can be ascribed to the carbon embedded porous structure of the materials which facilitates the facile ion intercalation/deintercalation. It opens up a lot easier access to the active Faradaic sites to ensure better exposure of the active material to the electrolyte, alongwith the improvement in structural stability. It's been noted that due to the presence of more carbon in NiO@C_20, it shows lower charge transfer resistance, high electrochromic stability; but the films fabricated out of it provide less optical transmittance in its pristine and bleached state compared to the other samples and the transmission modulation values obtained from those are also less (Figure 3.7d). From that standpoint, NiO@C_35 is a better candidate than NiO@C_20 and due to the presence of embedded carbon, it also provides better electrode stability besides having lesser charge transfer resistance than NiO@C_50. Thus, further in this work, for electrochromic battery application films made out of NiO@C_35 are deployed as the electrode materials.

3.3.6. Electrochromic battery measurements

Our electrochromic battery is comprised of Zn foil as anode and NiO@C_35 as negative electrode in an alkaline solution of 1 M KOH with an optimized concentration of 10 mM ZnAc₂. All the galvanostatic charge discharge measurements along with in-situ transmission modulation data and cycling test were done in a two-electrode cell. To check the feasibility of this assembly in battery application, prior to all measurements CVs (at 50 mV/s scan rate) for Zn foil and NiO (Figure 3.11a) were separately checked in a 3-electrode system (Ag/AgCl/Cl⁻ as reference and Pt wire as counter electrode) in the above mentioned mixed electrolyte system. Redox peaks originated due to the stripping/plating of Zn corresponding to the conversion of [Zn(OH)₄]²⁻/Zn [29] are located at -1.3/-1.61 V and the peaks located at 0.6/0.17 V represent the Ni³⁺/Ni²⁺ redox couples. A large potential gap of 1.84 V is noticed between Zn and NiO, which allows us to implement this pair as a battery system in our work.

In this system, Zn undergoes oxidation to form Zn²⁺ and simultaneously Ni³⁺ undergoes reduction to turn to Ni²⁺ during electricity generation. The electrode and overall cell reactions are depicted by the following equations [30] –



Chapter 3

The CV data for the assembled 2 electrode system at different scan rates (1 to 70 mVps) at a voltage range of 1.4 to 2.15 V are presented in Figure 3.11b. The calculated b value from $\log(i)$ vs $\log(v)$ plot is 0.61, given in the inset of Figure 3.11b, indicating the overall reaction is guided by diffusion-controlled kinetics. Introduction of ZnAc_2 in KOH electrolyte betters the reversibility of redox reaction of Zn metal and cyclic stability of the whole battery unit.[31]

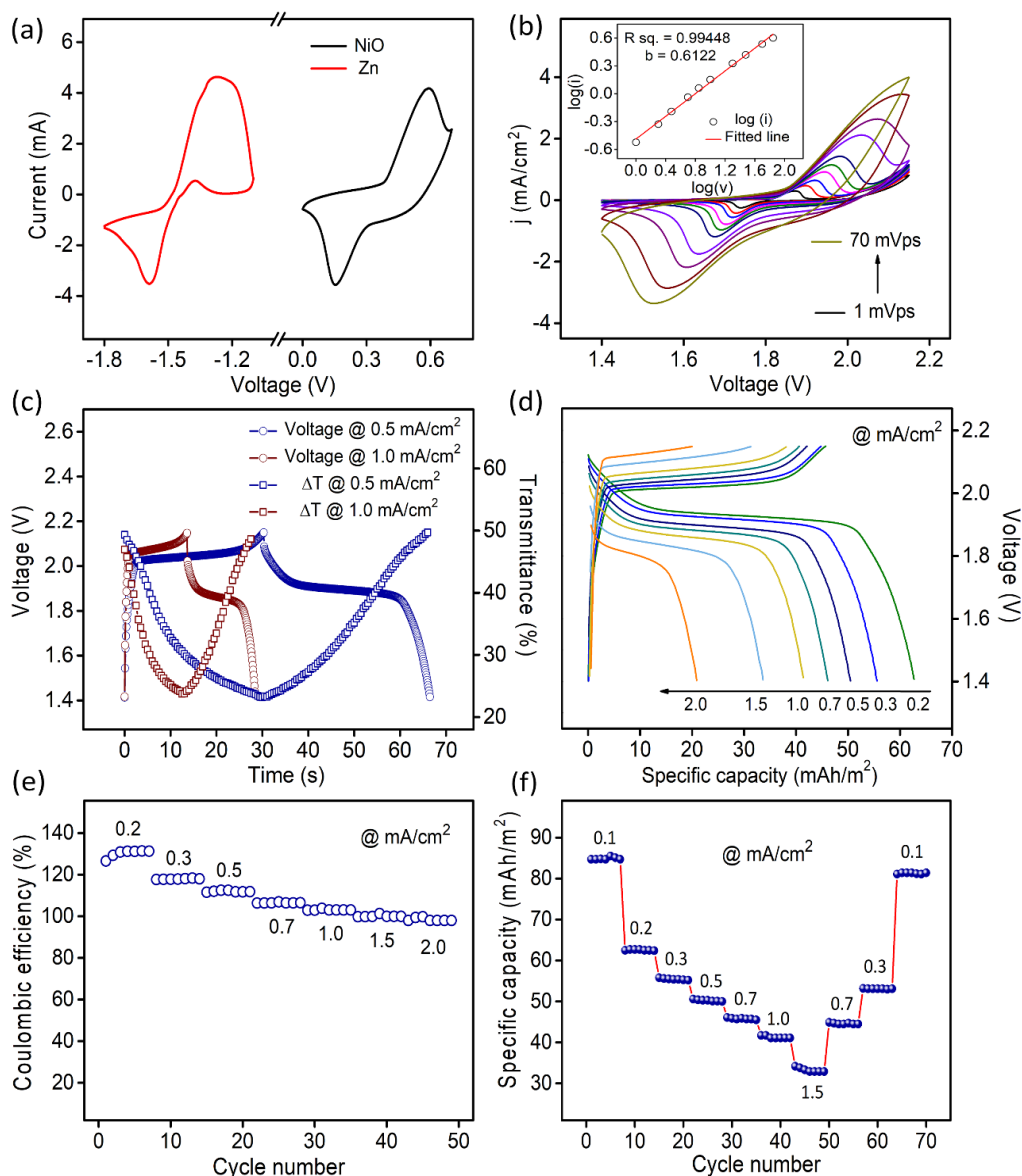
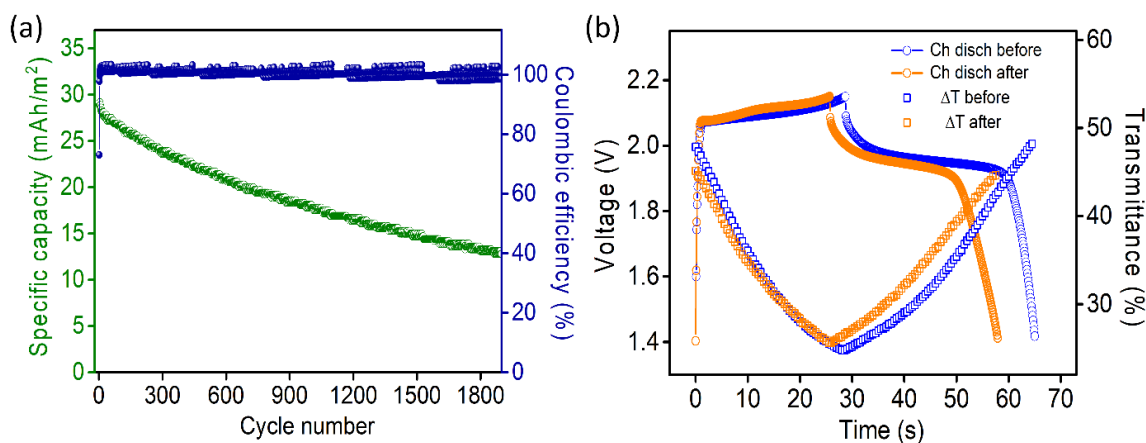


Figure 3.11: (a) CV showing the stripping and plating of Zn and redox reactions of NiO@C₃₅ in a three-electrode set-up with 1 M KOH + 10 mM ZnAc₂ electrolyte, (b) scan rate dependent CV data in 2 electrode system, inset shows $\log(i)$ vs $\log(v)$ plot with corresponding linear fitting (c) charge-discharge profiles at different current densities and the corresponding change in transmission modulation @525 nm (d) galvanostatic charge-discharge profiles at different current densities, (e) coulombic efficiency values at different current densities, (f) rate capability plot

Transmission modulation data at a wavelength of 525 nm, synchronized with the charging-discharging of the battery were collected at 2 different current densities 0.5 and 1 mA/cm², given in Figure 3.11c. The specific capacity of the battery is correlated with its colour. When it is in fully charged state, its opacity increases and looks dark brown in colour. In its discharged state, the colour fades out, corresponding to a transmission modulation of ~ 30%.

To investigate the charge storage capability of the battery, galvanostatic static charge-discharge (GCD) measurements of our system were performed in the same potential range as that of the 2 electrode CV at different current densities ranging from 0.2-2 mA/cm² (Figure 3.11d). At lower current densities the obtained discharge capacity is higher than the charging capacity, similar phenomenon has been observed by other researchers also.[32] This might be due to the reduction of dissolved oxygen or the insertion of cations present in the electrolyte at lower current densities.[32, 33] As a result of this, higher coulombic efficiency at lower current density was observed and when the current density starts to increase the coulombic efficiency gradually reaches the value of 100%. Figure 3.11e presents the coulombic efficiency values at different current densities.

As depicted in the rate capability plot, presented in Figure 3.11f, the specific capacity varies from 85.3 to 33 mAh/m² as the discharge current density varies from 0.1 to 1.5 mA/cm². The reversible discharge capacity of the battery falls slightly from 46 to 44.8 mAh/m² at a current density of 0.7 mA/cm², corresponding to a capacity retention of 97.4%. Similarly at 0.1 mA/cm² discharge current density, capacity drops from 85.3 to 81.4 mAh/m², which is equivalent to 95.4% capacity retention. Thus, it shows good stability of the electrochromic battery. A comparison of our data with other reported literatures is presented in Table 3.3 which shows a decent performance with a relatively high discharge capacity.



Chapter 3

Figure 3.12: (a) Specific discharge capacity (20% decay in capacity after 350 cycles) and coulombic efficiency data with cycling @1 mA/cm² current density, (b) voltage and transmission modulation (at 525nm) with time before and after cycling

Cycling performance of the battery was checked for 1900 cycles (Figure 3.12a) at a current density of 1 mA/cm² and the corresponding average coulombic efficiency is found to be nearly 100% excluding a few initial cycles. 20% decay in capacity is observed after 350 charge-discharge cycles. NiO electrode's stability has been already demonstrated in Figure 3.8d, which is quite decent upto 1500 cycles, but in case of the battery system, comparatively faster capacity degradation is noticed mainly because of the formation of Zn(OH)₂ or ZnO and dendrite growth on the Zn electrode.[30] Charging discharging plots at 0.5 mA/cm² current density along with the in-situ transmission modulation at 525 nm before and after cycling study are presented in Figure 3.12b, where only 4.3% decrement in the transmission modulation value is perceived.

Table 3.3: Comparison of discharge capacity, and transmission modulation with other NiO based electrochromic energy storage works reported in the literature

System	Electrolyte	Storage type	Transmission modulation (%)	Capacity or Capacitance	Reference
NiO/PB // hex-WO ₃	1 M LiClO ₄ /PC	Supercapacitor	67.6% at 630 nm	11.5 mF/cm ² at 0.05 mA/cm ²	Pan et al.[34]
rGO-NiO nanoflake // WO ₃ nanowire	LiClO ₄ - PVA polyelectrolyte	Battery	43% at 750 nm and 62% at 2000 nm	75 mAh/g at 1 A/g	Xia et al.[35]
Li-doped NiO (3 electrode)	1 M LiClO ₄ /PC	Supercapacitor	66.5% at 550 nm	13 mF/cm ² at 0.1 mA/cm ²	He et al.[36]
NiO // MoO ₃ -W _{0.71} Mo _{0.29} O ₃	1 M LiClO ₄ /PC	Battery	41.9% at 632.8 nm	2.33 mAh/m ² at 0.05 mA/cm ²	Li et al.[37]
Hierarchical porous NiO (3 electrode)	1 M KOH	Supercapacitor	41.8% at 650 nm	2.08 F/cm ² at 1 mA/cm ²	Zhou et al.[5]
ITO/NiO (3 electrode)	1 M KOH	Supercapacitor	8.6% at 550 nm	1.99 mF/cm ² at 0.05 mA/cm ²	Dong et al.[38]
NiO-Ag-NiO (3 electrode)	1 M KOH	Supercapacitor	24.3% at 550 nm	9.49 mF/cm ² at 0.05 mA/cm ²	Dong et al.[38]

Chapter 3

NiO nanoflake (3 electrode)	1 M KOH	Supercapacitor	40% at 632.8 nm	74.8 mF/cm ² at 10 mVs	Chen et al.[39]
Co-doped NiO (3 electrode)	1 M KOH	Supercapacitor	52% at 630 nm	88.24 mF/cm ² at 0.4 mA/cm ²	Xue et al.[40]
Co-doped NiO/FTO // Fe ₂ O ₃	Nylon membrane soaked in 1 M KOH	Supercapacitor	---	10.8 mF/cm ² at 0.4 mA/cm ²	Xue et al.[40]
Zn // NiO@C_35	1 M KOH + 10 mM ZnAc ₂	Battery	28.6% at 525 nm	85.3 mAh/m ² at 0.1 mA/cm ²	This work

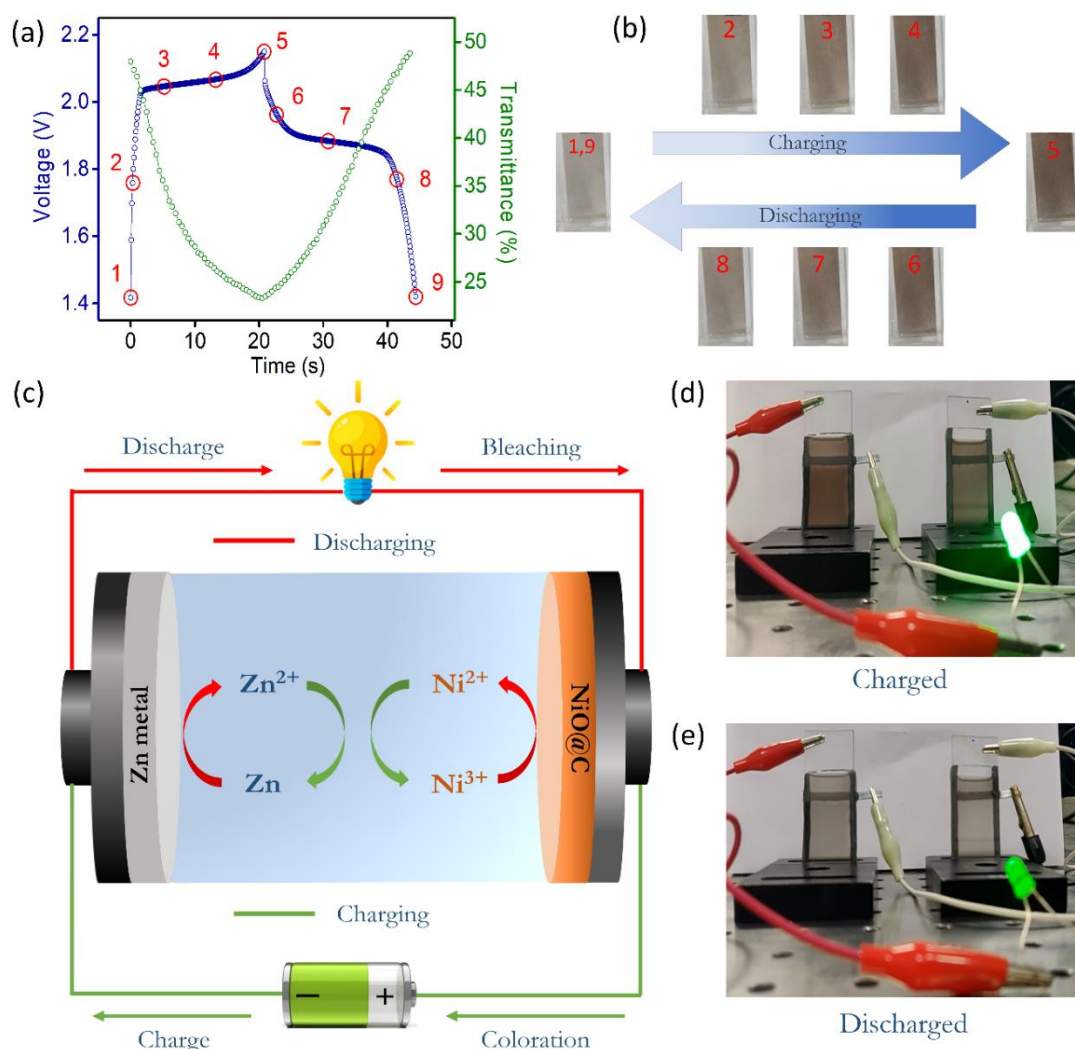


Figure 3.13: (a) GCD profile at 0.7 mA/cm² along with the corresponding transmittance data of the EC battery; (b) photographs of the electrochromic battery at different stages of charging and discharging as designated by red circles in Figure 3.13a; (c) schematic of the Zn-NiO electrochromic battery (red lines show the processes involved during discharging and green

lines show the processes during charging); digital photograph of the device in its (d) charged state and (e) discharged state

Figure 3.13a presents the charge-discharge profile at 0.7 mA/cm^2 synchronized with the transmittance curve at 525 nm and the corresponding pictorial depiction of the electrochromic battery at different stages is illustrated in Figure 3.13b as designated by red circles in the GCD curve of Figure 3.13a. A prototype device ($2.5 \text{ cm} \times 4 \text{ cm}$) is assembled to show its applicability in electrochromic battery displays. The schematic configuration of the device along with the half cell reactions is presented in Figure 3.13c. Two devices connected in series can light up a commercial green LED for about 10 mins. The photograph of the battery in its coloured state with illuminated green LED is presented in Figure 3.13d. Figure 3.13e shows the discharged state of the battery where the window is relatively transparent.

3.4. Conclusion

In summary, MOF-derived NiO@C has been utilized to fabricate electrochromic electrodes and is capable of demonstrating high coloration efficiency ($\sim 135.16 \text{ cm}^2/\text{C}$) with faster switching speeds ($\sim 1.4 \text{ s}$ for coloration and $\sim 3.5 \text{ s}$ for bleaching). The carbon embedded porous structure of this material promotes its charge transfer kinetics which sequentially results in its superior electrochromic performances. Later, this electrochromic NiO is used alongside a Zn foil to construct a smart rechargeable battery, which is capable of storing charge when coloured and provides electrical current while being bleached. Our Zn-NiO electrochromic battery shows a high discharge capacity of 85.3 mAh/m^2 at 0.1 mA/cm^2 current density and retains almost 80% of its capacity after 350 cycles at 1 mA/cm^2 current density. Moreover, the appreciable point of our electrochromic battery is that it consumes power only during coloration. It eliminates the requirement of energy consumption during the bleaching process, whereas current consumption for the traditional electrochromic windows is often both ways, which is a major drawback in present global scenario. Apart from all the merits of this work, there are still some major challenges in this work that can be addressed. Our device needs to provide external bias for coloration (charging) which refrains it from practical application, which can be addressed by integrating a photovoltaic cell with it.[35]

3.5. Bibliography

- [1] D.S. Dalavi, R.S. Devan, R.S. Patil, Y.-R. Ma, M.-G. Kang, J.-H. Kim, P.S. Patil, Electrochromic properties of dandelion flower like nickel oxide thin films, *J. Mater. Chem. A*, 1 (2013) 1035-1039.
- [2] D.S. Dalavi, M.J. Suryavanshi, S.S. Mali, D.S. Patil, P.S. Patil, Efficient maximization of coloration by modification in morphology of electrodeposited NiO thin films prepared with different surfactants, *J. Solid State Electrochem.*, 16 (2012) 253-263.
- [3] G.-f. Cai, J.-p. Tu, J. Zhang, Y.-j. Mai, Y. Lu, C.-d. Gu, X.-l. Wang, An efficient route to a porous NiO/reduced graphene oxide hybrid film with highly improved electrochromic properties, *Nanoscale*, 4 (2012) 5724-5730.
- [4] J.Y. Lee, K. Liang, K.H. An, Y.H. Lee, Nickel oxide/carbon nanotubes nanocomposite for electrochemical capacitance, *Synth. Met.*, 150 (2005) 153-157.
- [5] S. Zhou, S. Wang, S. Zhou, H. Xu, J. Zhao, J. Wang, Y. Li, An electrochromic supercapacitor based on an MOF derived hierarchical-porous NiO film, *Nanoscale*, 12 (2020) 8934-8941.
- [6] F. Zou, Y.-M. Chen, K. Liu, Z. Yu, W. Liang, S.M. Bhaway, M. Gao, Y. Zhu, Metal Organic Frameworks Derived Hierarchical Hollow NiO/Ni/Graphene Composites for Lithium and Sodium Storage, *ACS Nano*, 10 (2016) 377-386.
- [7] A.K. Chaudhari, B.E. Souza, J.-C. Tan, Electrochromic thin films of Zn-based MOF-74 nanocrystals facilely grown on flexible conducting substrates at room temperature, *APL Mater.*, 7 (2019) 081101.
- [8] J. Liu, X.Y.D. Ma, Z. Wang, L. Xu, F. Wang, C. He, X. Lu, Metal–Organic Framework-Based Flexible Devices with Simultaneous Electrochromic and Electrofluorochromic Functions, *ACS Appl. Electron. Mater.*, 3 (2021) 1489-1495.
- [9] C.R. Wade, M. Li, M. Dincă, Facile Deposition of Multicolored Electrochromic Metal–Organic Framework Thin Films, *Angew. Chem. Int. Ed.*, 52 (2013) 13377-13381.
- [10] X. Ju, F. Yang, X. Zhu, X. Jia, Zinc Ion Intercalation/Deintercalation of Metal Organic Framework-Derived Nanostructured NiO@C for Low-Transmittance and High-Performance Electrochromism, *ACS Sustain. Chem. Eng.*, 8 (2020) 12222-12229.
- [11] G. Zhang, S. Hou, H. Zhang, W. Zeng, F. Yan, C.C. Li, H. Duan, High-Performance and Ultra-Stable Lithium-Ion Batteries Based on MOF-Derived ZnO@ZnO Quantum Dots/C Core–Shell Nanorod Arrays on a Carbon Cloth Anode, *Adv. Mater.*, 27 (2015) 2400-2405.

- [12] P. Wang, J. Lang, D. Liu, X. Yan, TiO₂ embedded in carbon submicron-tablets: synthesis from a metal–organic framework precursor and application as a superior anode in lithium-ion batteries, *Chem. Comm.*, 51 (2015) 11370-11373.
- [13] J. Shao, Z. Wan, H. Liu, H. Zheng, T. Gao, M. Shen, Q. Qu, H. Zheng, Metal organic frameworks-derived Co₃O₄ hollow dodecahedrons with controllable interiors as outstanding anodes for Li storage, *J. Mater. Chem. A*, 2 (2014) 12194-12200.
- [14] X. Xu, R. Cao, S. Jeong, J. Cho, Spindle-like Mesoporous α -Fe₂O₃ Anode Material Prepared from MOF Template for High-Rate Lithium Batteries, *Nano Lett.*, 12 (2012) 4988-4991.
- [15] J. Yang, P. Xiong, C. Zheng, H. Qiu, M. Wei, Metal–organic frameworks: a new promising class of materials for a high performance supercapacitor electrode, *J. Mater. Chem. A*, 2 (2014) 16640-16644.
- [16] H. Liang, R. Li, C. Li, C. Hou, Y. Li, Q. Zhang, H. Wang, Regulation of carbon content in MOF-derived hierarchical-porous NiO@C films for high-performance electrochromism, *Mater. Horiz.*, 6 (2019) 571-579.
- [17] A. Carton, A. Mesbah, T. Mazet, F. Porcher, M. François, Ab initio crystal structure of nickel(II) hydroxy-terephthalate by synchrotron powder diffraction and magnetic study, *Solid State Sci.*, 9 (2007) 465-471.
- [18] D. Koushik, M. Jošt, A. Dučinskas, C. Burgess, V. Zardetto, C. Weijtens, M.A. Verheijen, W.M.M. Kessels, S. Albrecht, M. Creatore, Plasma-assisted atomic layer deposition of nickel oxide as hole transport layer for hybrid perovskite solar cells, *J. Mater. Chem. C*, 7 (2019) 12532-12543.
- [19] A. Kotta, E.-B. Kim, S. Ameen, H.-S. Shin, H.K. Seo, Communication—Ultra-Small NiO Nanoparticles Grown by Low-Temperature Process for Electrochemical Application, *J. Electrochem. Soc.*, 167 (2020) 167517.
- [20] E. Duraisamy, E. Sujithkrishnan, K. Kannadasan, P. Prabunathan, P. Elumalai, Facile metal complex-derived Ni/NiO/Carbon composite as anode material for Lithium-ion battery, *J. Electroanal. Chem.*, 887 (2021) 115168.
- [21] Z. Zeng, X. Peng, J. Zheng, C. Xu, Heteroatom-Doped Nickel Oxide Hybrids Derived from Metal–Organic Frameworks Based on Novel Schiff Base Ligands toward High-Performance Electrochromism, *ACS Appl. Mater. Interfaces*, 13 (2021) 4133-4145.
- [22] J. Nagai, Characterization of evaporated nickel oxide and its application to electrochromic glazing, *Sol. Energy Mater. Sol. Cells*, 31 (1993) 291-299.

- [23] G. Bo, X. Wang, K. Wang, R. Gao, B. Dong, L. Cao, G. Su, Preparation and electrochromic performance of NiO/TiO₂ nanorod composite film, *J. Alloys Compd.*, 728 (2017) 878-886.
- [24] J. Guo, X. Guo, H. Sun, Y. Xie, X. Diao, M. Wang, X. Zeng, Z.-B. Zhang, Unprecedented Electrochromic Stability of α -WO_{3-x} Thin Films Achieved by Using a Hybrid-Cationic Electrolyte, *ACS Appl. Mater. Interfaces*, 13 (2021) 11067-11077.
- [25] A. Dewan, S. Haldar, R. Narayanan, Multi-shelled NiO hollow microspheres as bifunctional materials for electrochromic smart window and non-enzymatic glucose sensor, *J. Solid State Electrochem.*, 25 (2021) 821-830.
- [26] M. Sathiya, A.S. Prakash, K. Ramesha, J.M. Tarascon, A.K. Shukla, V₂O₅-Anchored Carbon Nanotubes for Enhanced Electrochemical Energy Storage, *J. Am. Chem. Soc.*, 133 (2011) 16291-16299.
- [27] Z.-J. Sun, H. Ge, S. Zhu, X.-M. Cao, X. Guo, Z.-H. Xiu, Z.-H. Huang, H. Li, T. Ma, X.-M. Song, Versatile template-free construction of hollow nanostructured CeO₂ induced by functionalized carbon materials, *J. Mater. Chem. A*, 7 (2019) 12008-12017.
- [28] G. Cai, X. Wang, M. Cui, P. Darmawan, J. Wang, A.L.-S. Eh, P.S. Lee, Electrochromo-supercapacitor based on direct growth of NiO nanoparticles, *Nano Energy*, 12 (2015) 258-267.
- [29] X. Fan, Z. Yang, W. Long, Z. Zhao, B. Yang, The preparation and electrochemical performance of In(OH)₃-coated Zn-Al-hydrotalcite as anode material for Zn–Ni secondary cell, *Electrochim. Acta*, 92 (2013) 365-370.
- [30] X. Wang, M. Li, Y. Wang, B. Chen, Y. Zhu, Y. Wu, A Zn–NiO rechargeable battery with long lifespan and high energy density, *J. Mater. Chem. A*, 3 (2015) 8280-8283.
- [31] M. Gong, Y. Li, H. Zhang, B. Zhang, W. Zhou, J. Feng, H. Wang, Y. Liang, Z. Fan, J. Liu, H. Dai, Ultrafast high-capacity NiZn battery with NiAlCo-layered double hydroxide, *Energy Environ. Sci.*, 7 (2014) 2025-2032.
- [32] J. Wang, J. Liu, M. Hu, J. Zeng, Y. Mu, Y. Guo, J. Yu, X. Ma, Y. Qiu, Y. Huang, A flexible, electrochromic, rechargeable Zn//PPy battery with a short circuit chromatic warning function, *J. Mater. Chem. A*, 6 (2018) 11113-11118.
- [33] B.N. Grgur, M.M. Gvozdenović, J. Stevanović, B.Z. Jugović, V.M. Marinović, Polypyrrole as possible electrode materials for the aqueous-based rechargeable zinc batteries, *Electrochim. Acta*, 53 (2008) 4627-4632.
- [34] J. Pan, R. Zheng, Y. Wang, X. Ye, Z. Wan, C. Jia, X. Weng, J. Xie, L. Deng, A high-performance electrochromic device assembled with hexagonal WO₃ and NiO/PB composite

nanosheet electrodes towards energy storage smart window, *Sol. Energy Mater. Sol. Cells*, 207 (2020) 110337.

[35] X. Xia, Z. Ku, D. Zhou, Y. Zhong, Y. Zhang, Y. Wang, M.J. Huang, J. Tu, H.J. Fan, Perovskite solar cell powered electrochromic batteries for smart windows, *Mater. Horiz.*, 3 (2016) 588-595.

[36] Y. He, T. Li, X. Zhong, M. Zhou, G. Dong, X. Diao, Lattice and electronic structure variations in critical lithium doped nickel oxide thin film for superior anode electrochromism, *Electrochim. Acta*, 316 (2019) 143-151.

[37] H. Li, L. McRae, C.J. Firby, M. Al-Hussein, A.Y. Elezzabi, Nanohybridization of molybdenum oxide with tungsten molybdenum oxide nanowires for solution-processed fully reversible switching of energy storing smart windows, *Nano Energy*, 47 (2018) 130-139.

[38] W. Dong, Y. Lv, N. Zhang, L. Xiao, Y. Fan, X. Liu, Trifunctional NiO–Ag–NiO electrodes for ITO-free electrochromic supercapacitors, *J. Mater. Chem. C*, 5 (2017) 8408-8414.

[39] Y. Chen, Y. Wang, P. Sun, P. Yang, L. Du, W. Mai, Nickel oxide nanoflake-based bifunctional glass electrodes with superior cyclic stability for energy storage and electrochromic applications, *J. Mater. Chem. A*, 3 (2015) 20614-20618.

[40] J. Xue, W. Li, Y. Song, Y. Li, J. Zhao, Visualization electrochromic-supercapacitor device based on porous Co doped NiO films, *J. Alloys Compd.*, 857 (2021) 158087.

Chapter 4

*A multicolored electrochromic
asymmetric supercapacitor*

Declaration: The work has been published in the following journal:

Nanoscale, 14, 17372-17384 (2022). Copyright. Royal Society of Chemistry.

- **Abstract**

Modern technological trends in smart electronic devices demand more intelligent automation. Simultaneous integration of energy storage and multicolor electrochromism in a single device improves the user-device interfacing based on a salient human-readable output. In this work, primarily a metal organic framework (MOF) derived V_2O_5 was synthesized which as an electrochromic material, shows high optical modulation, with very fast switching speeds. The multiple coloration states of V_2O_5 electrode make it worthy for further integration as a smart negative electrode in a multicolored electrochromic asymmetric supercapacitor, where electrochromic polyaniline electrode serves as the positive and counter electrode. The device demonstrates a high coloration efficiency as well as high areal capacitance and energy density. By virtue of its different chromatic states during charging and discharging, visual tracking of the state of charge of the supercapacitor can be realized more distinctively which was lacking in our previous work on Zn-NiO electrochromic battery, as there the color change was purely monochromatic, from dark brown to colorless. In that context, such energy storage devices where gradual change in color is perceived with different level of charge storage, may have promising practical applications for futuristic smart multifunctional electronic devices.

4.1. Introduction

Electrochemical capacitors or supercapacitors (SC) have gained widespread attention due to their fast charge discharge rate, long life along with important advantages to meet the urgent demand for high power density.[1, 2] With the recent evolution of electronic devices, the applications of SCs are extended to multi-functional and smart devices like self-charging SCs,[3] flexible wearable SCs,[4] shape-memory SC,[5] thermo-responsive SC,[6] self-healable SC,[7] electrochromic SC [8, 9] etc. Exploiting the configuration of an asymmetric SC, these devices could be implemented in different applications including smart windows for indoor light and temperature controls, adaptive camouflages, aesthetic multicolor displays with energy storage functionality etc. Multi-colored electrochromic asymmetric supercapacitors (MECASC) with different chromatic states will allow precise control over the modulation of light along with the real-time monitoring of the charge content of the device for its sustainable use by averting overcharging and over-discharging.[10-12]

Among existing electrochromic materials, the most studied ones are based on TMOs and conducting polymers. Reportedly, conducting polymers such as polyaniline (PANI) are of great interest due to their low cost, ease of synthesis, high electrical conductivity, rich color states, high theoretical capacity etc.[13] On the other hand, among TMOs, V_2O_5 is highly sought after in the field of electrochromism as it is the only TMO that can demonstrate both anodic and cathodic coloration upon reversible intercalation/deintercalation of alkaline cations (e.g., Li^+); which makes it suitable for multicolor displays. In addition, it has high theoretical capacity which makes it a strong contender for a wide variety of electrochemical applications.[14]

However, bulk V_2O_5 often suffers from serious volume expansion over cycling, poor ion diffusion kinetics, long switching times, low electrical conductivity etc.[15] To subdue these limitations, a lot of research has been done to make different micro-nanostructures of V_2O_5 and hybrid materials by incorporation of carbonaceous materials into them.[16, 17] Recently, metal organic frameworks (MOF) are used as a template for the synthesis of TMOs. MOFs are an emerging class of hybrid crystalline materials assembled via the coordination bonds between organic ligand molecules and metal ion centers, with huge chemical and configurational heterogeneities. These materials possess very high surface area and tunable pore sizes. Owing to their long range ordered porous structure with periodically arranged metal clusters, MOFs are used as sacrificial templates in the synthesis of porous metal oxides, sulfides and porous carbon embedded hybrid materials including V_2O_5 . [18-23]

In the present work, a MECASC is shown, that is constructed by stacking MOF-derived V_2O_5 and PANI films as the negative and positive electrodes respectively in propylene carbonate solvent containing 1 M $LiClO_4$ as the electrolyte. The module visually exhibits the stored energy level by different colors as well as demonstrates the feasibility of redemption of the acquired energy during bleaching. MOF-derived V_2O_5 samples are synthesized by two different pyrolysis procedures. Carbon leftovers along with the porous structures of the V_2O_5 samples provide the ions of the electrolyte, a hassle-free access to the reaction sites to enhance the charge transfer kinetics. Thorough electrochemical characterizations of the V_2O_5 electrodes and separately the capacitance measurements of both V_2O_5 and PANI electrodes are carried out in 1 M $LiClO_4/PC$ medium in a three-electrode set-up. In a two-electrode configuration, a functional MECASC device is fabricated having a wide potential window up to 2 V with the option to visually judge the state of charge of the device.

4.2. Experimental section

4.2.1. Chemicals and materials

Vanadium trichloride (VCl_3), p-benzenedicarboxylic acid (PTA), aniline, N,N-dimethylformamide (DMF), propylene carbonate (PC) and lithium perchlorate (LiClO_4) were acquired from Alfa Aesar. Transparent $\text{SnO}_2\text{:F}$ (FTO) coated glass substrates with sheet resistance of $15 \Omega \text{ sq}^{-1}$ were obtained from Sigma Aldrich. All the chemicals were of analytical grade and used as received without any further modification. FTO substrates were washed with soap solution, later rinsed with isopropanol, ethanol and ample amount of water respectively under ultrasonic treatment. During the experiments, aqueous solutions were prepared using reagent grade milli-Q water with $18.2 \text{ M}\Omega \text{ cm}$ resistivity (Millipore Direct Q3 system).

4.2.2. Material synthesis and electrode fabrication

4.2.2.1. Synthesis of negative electrode material (V_2O_5)

MIL-101(V) (Vanadium MOF or V-MOF) was synthesized via a solvothermal reaction route following the report of Carson et al.[24] According to the report, 166 mg of PTA (1 mmol) and 157 mg of VCl_3 (1 mmol) were first added to 5 ml of absolute ethanol. The mixture was then kept on a Tarson 3002 spinix vortex shaker for 10 min until the solution turns green. Then the whole precursor solution was transferred to a 30 ml teflon-lined autoclave. The autoclave was then heated in an oven at $120 \text{ }^\circ\text{C}$ for 48 h. After the reaction got over, the autoclave was very slowly cooled down to room temperature (slow cooling is very important to obtain crystalline MOF). The obtained product was then washed with ethanol and separated by centrifugation. The activation of MOF was performed by heating it in DMF under N_2 gas flow for 3 h at $70 \text{ }^\circ\text{C}$, and subsequent heating in ethanol for 3 h at $70 \text{ }^\circ\text{C}$ under N_2 flow. Finally, obtained green product was dried under vacuum at $120 \text{ }^\circ\text{C}$ for 16 h, which resulted in fluffy green V-MOF powder. Further to obtain V_2O_5 from V-MOF, two different annealing procedures were followed. In the first procedure, according to the report of Liang et al.[25], a two-step pyrolysis technique was followed where in the 1st step V-MOF powder was transferred to a ceramic boat before transferring it to a tube furnace, where it was annealed at $370 \text{ }^\circ\text{C}$ for 1 h under Ar-H_2 (97-3) flow and in the 2nd step, the sample was put through another heat treatment for 30 min under airflow, to obtain the product, designated as $\text{V}_2\text{O}_5\text{-2}$ throughout this chapter. Further, in the second procedure, V-MOF was directly annealed at $370 \text{ }^\circ\text{C}$ for 30 min under air. The product obtained from this process is labelled here as $\text{V}_2\text{O}_5\text{-1}$.

4.2.2.2. Fabrication of V₂O₅ films on FTO

All V₂O₅ films in this work were prepared on FTO using spray coating. The dispersion required for spray coating was prepared by dispersing the samples in isopropanol and milli-Q water mixture. Part of the substrates was covered with scotch tape to fix the geometrical area of electroactive material on the electrode. Subsequently, the dispersion was spray-coated on FTO and kept on a hot plate at 70 °C with an air-brush (ANMSALES AB-130, nozzle diameter ~ 0.3 mm; purchased from Amazon) using Ar as a carrier gas at a fixed pressure. The gap between the FTO and airbrush nozzle was maintained at ~ 12 cm. After each spray, adequate time was provided to dry the FTO.

4.2.2.3. Synthesis of positive electrode material (PANI)

PANI was deposited on FTO substrates by electrodeposition technique following a report of Mohd et al.[26] The electrolyte solution of 0.5 M Aniline in 1 M H₂SO₄ was used for the deposition. Upon application of a positive bias, aniline monomers get oxidized to radical ions triggering the polymerization reaction to occur.[27] All films were deposited for 150 sec at + 0.75 V using a potentiostatic technique in a three-electrode system with Pt wire as counter and Ag/AgCl/Cl⁻ as reference electrode. After deposition, the films were washed with copious amount of milli-Q water and dried under vacuum at room temperature.

4.2.3. Material characterization and electrochemical measurements

The morphological characterizations of the samples were performed by field emission scanning electron microscope (FESEM, Zeiss Ultra Plus) and transmission electron microscope (TEM, JEOL JEM-2200FS operating at 220 kV). Powder XRD measurements were carried out in Bruker D8 Advanced X-ray diffractometer with Cu K α radiation (1.54 Å). Thermogravimetric analysis (TGA) was done on a NETSZCH TGA-DSC system and the samples were heated under ambient atmosphere from room temperature to 600 °C at a rate of 5 °C min⁻¹. Raman spectroscopy experiment was conducted in LabRAM HR 800 (HORIBA Jobin Yvon) set-up, using a He-Ne Laser (632 nm, working at 10 % power). X-ray photoelectron spectroscopy (XPS) measurements of V₂O₅ samples were carried out using monochromatic and micro-focused AlK α radiation with energy of 1486.6 eV (Thermo Kalpha+ spectrometer). BET Surface area was measured using Micrometrics ASAP 2460 volumetric gas adsorption analyzer instrument with liquid N₂ at 77 K temperature. Before measurement, all samples were heated at 120 °C for 12 h under vacuum for removing impurities and pore opening.

The electrochemical measurements were carried out in the CH instrument set-up (CHI760E). For in-situ spectro-electrochemistry data, an Ocean Optics set-up consisting of a Deuterium-Halogen lightsource (DH-2000-BAL), optical fibers (200 μm core diameter) and a spectrometer (FLAME-T-XR1-ES) was used. In all electrochromic and energy storage related measurements, 1 M LiClO_4 in PC was used as electrolyte. For all three-electrode based experiments, FTO plates spray-coated with V_2O_5 or electro-deposited PANI films on FTOs were utilized as working electrodes, platinum (Pt) wire and silver (Ag) wire were employed as the counter and reference electrodes respectively.

4.3. Results and discussion

4.3.1. Negative electrode material (V_2O_5)

4.3.1.1. Structural and morphological properties

The XRD pattern of the activated V-MOF is presented in Figure 4.1a, which matches well with the reported simulated XRD pattern (CCDC no.- 605510).[24, 28, 29] Before going ahead with the samples for further processing, TGA/DSC measurements were performed. As it can be seen from Figure 4.1b, the initial weight loss of the sample between 30-100 $^\circ\text{C}$ was ascribed to the desorption of adsorbed water and solvent molecules. The weight loss of 14.4% in between 100-300 $^\circ\text{C}$ was attributed to the decoordination of H_2O molecules from the vanadium trimers as well as the removal of guest molecules from the pores of the MOF structures. Finally, the weight loss of 52% beyond 300 $^\circ\text{C}$ leads to the decomposition of the structures and removal of carbon skeleton towards the formation of fluffy yellow V_2O_5 samples.[22, 24] In differential scanning calorimetry (DSC) measurement, the said change in the material is also reflected as a strong endothermic peak centered at ~ 370 $^\circ\text{C}$ indicating the structural collapse of the MOF during the formation of V_2O_5 . Figure 4.1c presents the XRD data of V_2O_5 samples. XRD patterns of both 1-step and 2-step annealed samples corresponding to different crystal planes match well with the orthorhombic V_2O_5 phase (JCPDS card no.- 01-072-0433), indicating the crystalline nature of the samples.

Raman spectroscopy measurements were carried out on both samples. Raman spectra (Figure 4.1d) highlight several well-resolved peaks at $\sim 145, 199, 286, 305, 405, 482, 527, 703$ and 995 cm^{-1} which are the characteristic peaks of crystalline V_2O_5 . The vibrational Raman active modes are associated with vanadium-oxygen-vanadium bending vibrations, translational modes and vanadium-oxygen stretching modes. The highest intensity peak centered at 145 cm^{-1} corresponds to the bond deformation between different molecular units in the plane of layers,

also termed skeleton bending vibration. The peak at 995 cm^{-1} is attributed to the stretching mode vibration related to V=O bond.[30]

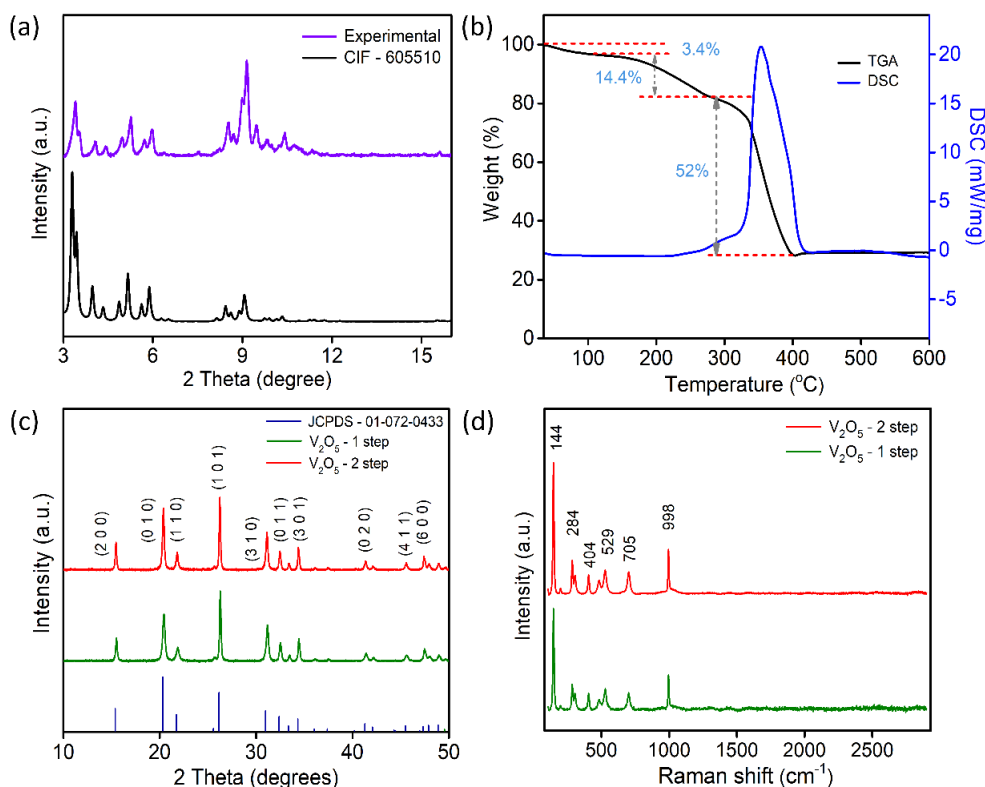


Figure 4.1: (a) XRD pattern of the activated V-MOF (purple) and the reported data CIF – 605510, (b) TGA and DSC data for V-MOF, (c) XRD data of V₂O₅ samples alongwith JCPDS card (01-072-0433) data, (d) Raman data for both V₂O₅ samples

Morphological characterizations of the samples were conducted by FESEM and TEM measurements. Figure 4.2a illustrates the morphology of V₂O₅-1 sample, the sample mainly consists of irregularly shaped V₂O₅ nanoplates of dimensions ranging between 30-90 nm. Lower magnification TEM data is presented in Figure 4.2b, and is concurrent with the FESEM images, exhibiting the presence of very thin nanoplates in the sample. The high-resolution TEM (HR-TEM) data (Figure 4.2c) of the sample depicts the presence of lattice fringes with spacing of 0.35 and 0.6 nm which correspond to the (210) and (200) crystal planes of orthorhombic V₂O₅ respectively. Similar sort of morphology was also observed for V₂O₅-2 sample, as illustrated in Figure 4.2h-4.2j. Further, EDX mapping measurements were performed on both of the samples to check the presence of different elements e.g., elemental carbon alongwith vanadium and oxygen as shown in Figure 4.2d-4.2g (and in Figure 4.2k-4.2n). Carbon mapping images (Figure 4.2g and Figure 4.2n) for both the samples look almost similar and a very small amount of carbon presence was observed. The amount of carbon for both the samples was quantified using XPS measurements as discussed later.

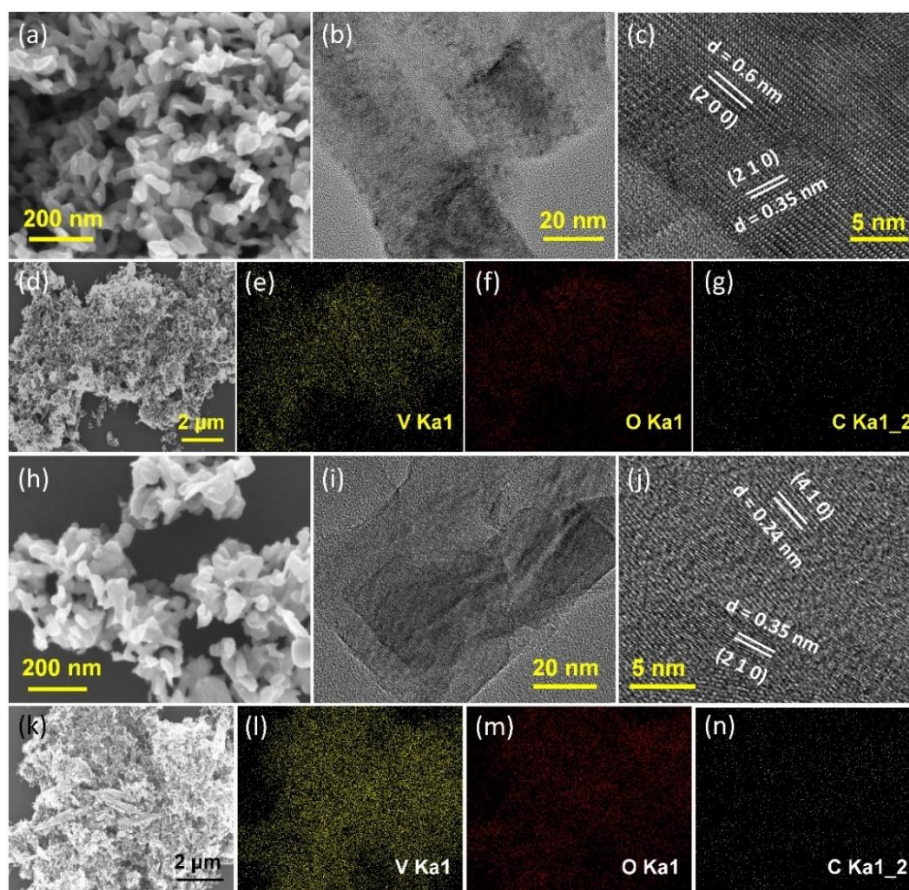


Figure 4.2: FESEM, TEM, HRTEM images and EDX data for elemental mapping of (a)-(g) V_2O_5-1 and (h)-(n) V_2O_5-2 sample

The surface chemical states of the samples were analyzed through XPS measurements as presented in Figure 4.3. Figure 4.3a and Figure 4.3b present the survey spectra for the samples which show the peaks corresponding to the vanadium, oxygen and carbon in the sample in accordance with the EDX mapping data (Figure 4.2d-4.2g and Figure 4.2k-4.2n). From XPS measurement, the carbon content in V_2O_5-2 and V_2O_5-1 samples were quantified and found to be almost in a similar range, 12.47% and 12.43% respectively. Core level spectra of $V2p$ show two major peaks at 517.2 eV and 524.8 eV, which correspond to $V2p_{1/2}$ and $V2p_{3/2}$ (Figure 4.3b and Figure 4.3f). On deconvolution, the weaker and broader peaks at 516.3 eV and 523.6 eV are related to the presence of V^{4+} oxidation states and relatively stronger peaks (at 517.3 and 524.9 eV) are assigned to the V^{5+} states of V_2O_5 . [20, 21, 31] The $O1s$ spectra provided in Figure 4.3c and Figure 4.3g, can be deconvoluted into three peaks. The most intense peak at 530 eV corresponds to the existence of V-O bond in V_2O_5 . The peak that appeared at 531 eV is due to C-O bond and the peak that emerged at 532.6 eV is related to either O=C-O or the adsorbed H_2O molecules. [20, 32-34] Figure 4.3d and Figure 4.3h present asymmetric $C1s$ peaks, which were resolved into three peaks. The dominant peak at 284.5 eV

arises due to the presence of graphitized carbon (C-C and C=C) in the sample generated due to the denaturation of the carbon skeleton during the annealing of the sample. The peak located at 286.1 eV is associated with C-O bonds and the smallest peak at 288.5 eV is related to C=O groups.[33, 35] Therefore, XPS data concludes the presence of graphitized carbon in both the samples almost in similar quantities.

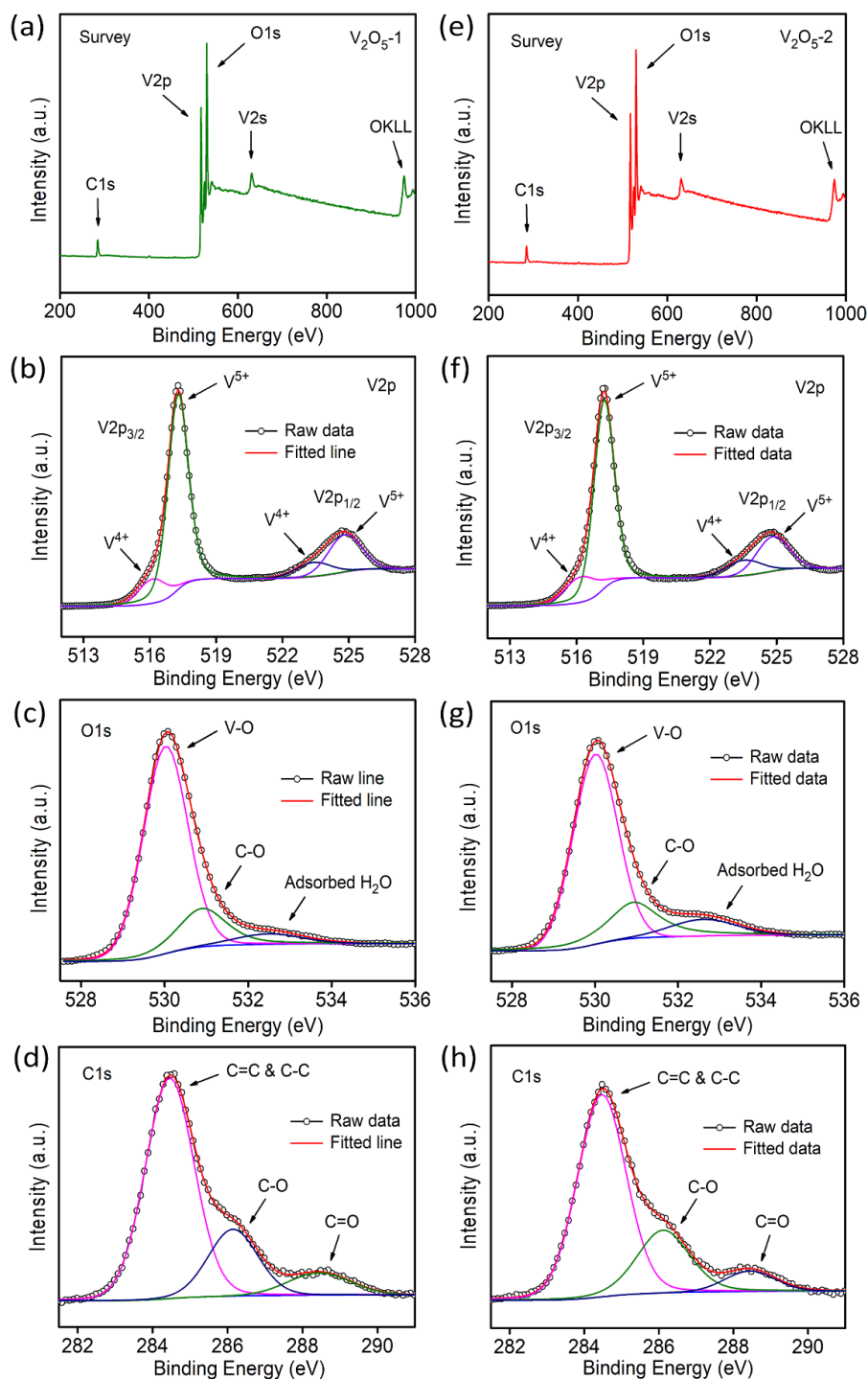


Figure 4.3: XPS data including survey spectra and the deconvoluted spectra of (a)-(d) V_2O_5-1 and (e)-(h) V_2O_5-2 samples

4.3.1.2. Surface area measurements of the V₂O₅ samples

Further, N₂ gas adsorption measurement (Figure 4.4) at 77 K was carried out to check the surface areas and pore size distributions of the V₂O₅ samples. The adsorption isotherms exhibit typical mesoporous nature of the samples. The surface areas of the samples were calculated by BET fitting (Figure 4.4b and Figure 4.4e) and the specific surface area was found to be higher (178 m²/g) for V₂O₅-1 sample than V₂O₅-2 sample (112 m²/g). Non-local pore size distribution (NLDFT) method was used to calculate the pore-size distribution of the samples as shown in Figure 4.4c and Figure 4.4f. Longer annealing time of V₂O₅-2 (because of 2-step annealing process) reduces the pore volume in comparison to only air annealed V₂O₅-1 sample. Overall, the mesoporous structures of the samples are expected to ensue facile ion exchange with the electrolyte towards better electrochemical performance.

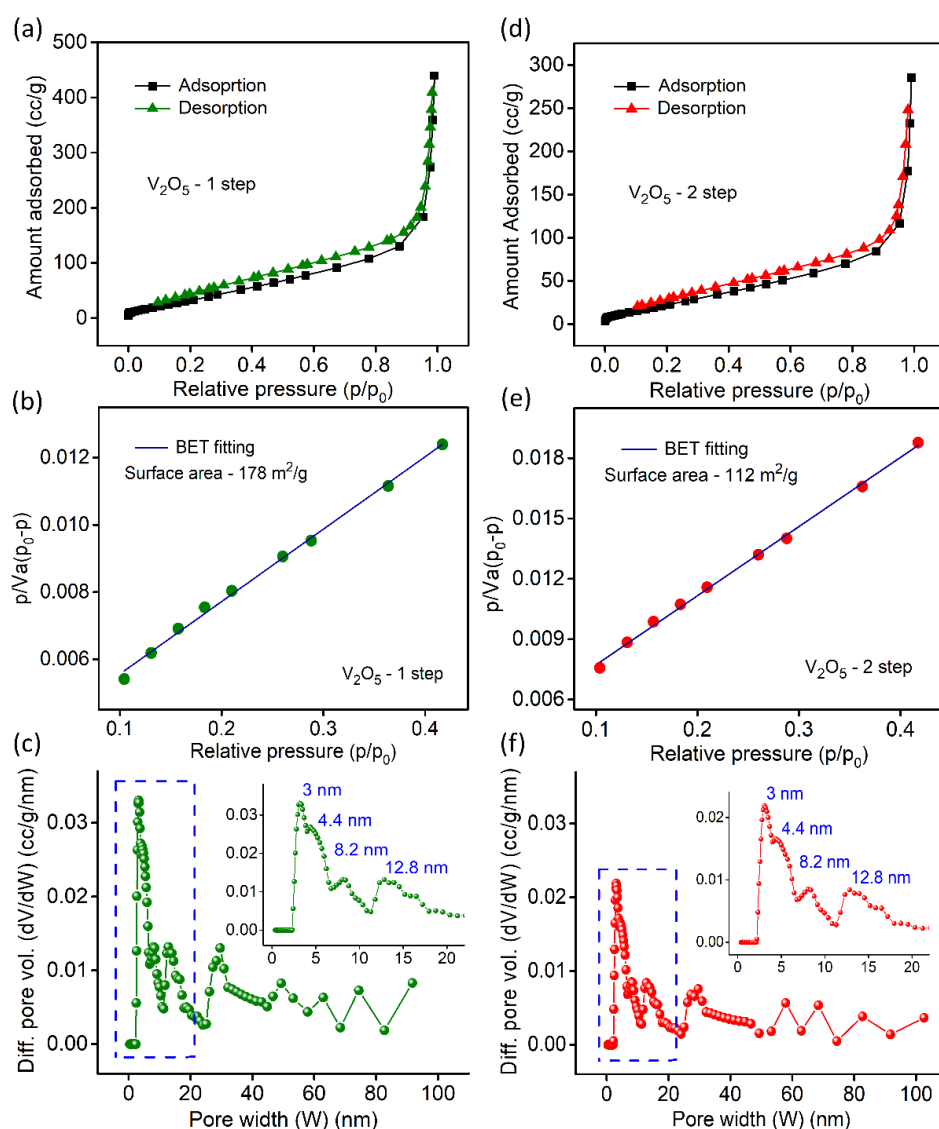
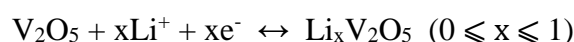


Figure 4.4: N₂ gas adsorption isotherms at 77 K, BET fitting and NLDFT pore size distribution data for (a)-(c) V₂O₅-1 and (d)-(f) V₂O₅-2 samples

4.3.1.3. Electrochromic studies on V₂O₅ electrodes

Electrochromic properties of V₂O₅ electrodes were examined in a three-electrode set-up as mentioned in the experimental section using an in-situ spectroelectrochemical technique. Before analyzing the spectro-electrochemistry data, let's check the electrochemical process, that is responsible for the electrochromism of V₂O₅. The whole process of reversible color change is mostly dependent on the reversible Li⁺ ion intercalation and deintercalation in V₂O₅ electrodes causing a redox reaction that leads to the change in the oxidation state of vanadium and consequently to different chromatic states. In Figure 4.5, the cyclic voltammogram (CV) of a V₂O₅-1 electrode at 7 mVps scan rate features two pairs of redox peaks and the corresponding electrochemical reaction is stated as follows [36] –



where x is the mole fraction of the intercalated Li⁺ ions. Based on the amount of inserted Li⁺ ions, different crystal phases of V₂O₅ are designated. The 1st redox couple corresponds to the change of α-V₂O₅ (0 < x < 0.1) to ε-V₂O₅ (0.35 < x < 0.5) and the 2nd redox couple is ascribed to the conversion of ε-V₂O₅ to δ-V₂O₅ (0.9 < x < 1) and vice versa.[37, 38]

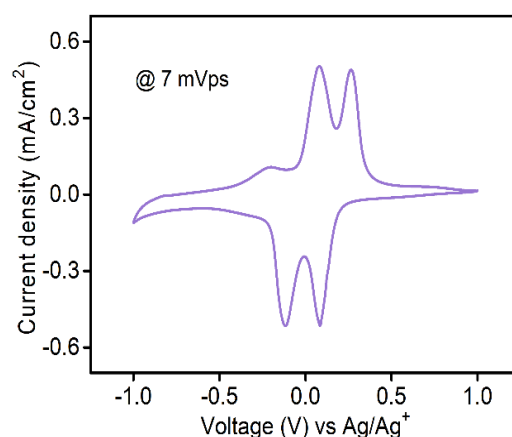


Figure 4.5: Cyclic voltammogram (CV) of V₂O₅-1 electrode in three-electrode set-up at 7 mVps scan rate in 1 M LiClO₄/PC electrolyte

The transmission spectra for V₂O₅ samples were collected during the cathodic scan (+1 V to -1 V vs Ag/Ag⁺ electrode). Figure 4.6a demonstrates the transmission spectra for V₂O₅-2 electrode at the two extreme voltages along with the optical modulation data (blue curve), which is defined as the difference between the transmittance at colored and bleached state of an electrochromic material at a particular wavelength λ (i.e., ΔT = T_b(λ) – T_c(λ)). The analogous data for V₂O₅-1 electrodes is given in Figure 4.6b. Interestingly, it was observed for both the materials that the transmittance in the visible and near-infrared region changes reversibly upon

applying voltages. Higher ΔT values of about 35 % at 485 nm and 26.5 % at 1000 nm were obtained for V_2O_5 -1 electrodes. Figure 4.6c illustrates the transmission spectra for V_2O_5 -1 electrodes at different voltages. Corresponding photographs of the films at different voltages are shown in Figure 4.6d. The film reversibly switches its color from yellow (+1 V) to bluish gray (-1 V). In in-situ spectroelectrochemistry measurement, the transmission modulation of V_2O_5 -1 film was closely monitored at 485 nm and 1000 nm, illustrated in Figure 4.6e (dotted lines). The dynamical changes of transmittances (indicated by arrows) are commensurate to the modulation in current density.

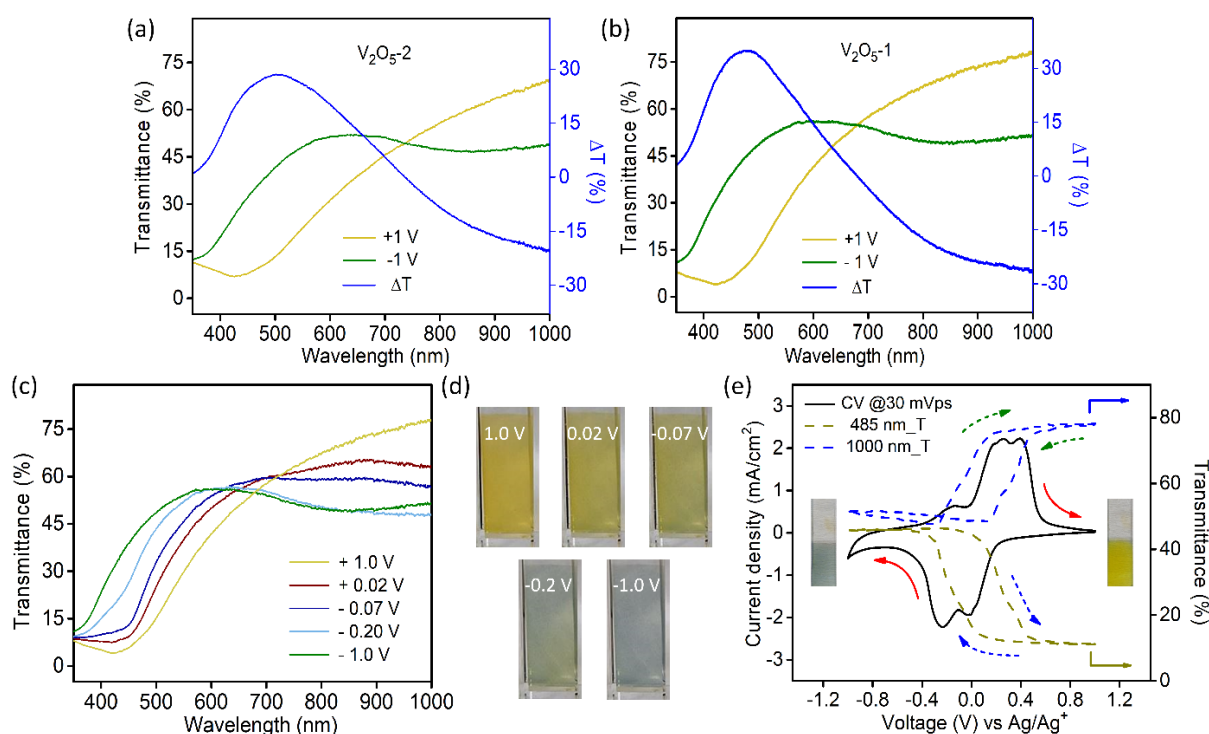


Figure 4.6: Transmission spectra of (a) V_2O_5 -2 and (b) V_2O_5 -1 films at two extreme potentials along with the transmission modulation spectrum (ΔT) (blue lines), (c) transmission spectra of V_2O_5 -1 films under different biases, (d) corresponding film photographs at those potentials, (e) CV data (solid line) of V_2O_5 -1 film with in-situ transmittance data (dashed lines) at 485 nm (dark yellow) and 1000 nm (blue)

Switching time for the electrochromic materials is described as the time required for attaining 90% of the total optical modulation under the application of an alternating potential. Switching times were measured at 485 nm (Figure 4.7a) and 1000 nm (Figure 4.7b) wavelengths separately by applying +1 V and -1 V bias. The data for both samples are presented in Table 1. Although each sample contains graphitized carbon almost in close quantity, because of the higher surface area of V_2O_5 -1 sample, it manifests faster switching times compared to V_2O_5 -2 electrodes. Coloration efficiency (CE) of an electrochromic material

is an important parameter in terms of estimating the power requirement for electrochromic switching. This is defined as the ratio of change in optical density (ΔOD) to the intercalated or deintercalated charge density (mC/cm^2). [39] CE can be calculated from the following formula stated as –

$$CE = \log (T_b/T_c) / (Q/A) \quad (2)$$

CE values were calculated at 485 nm and 1000 nm from the slope of the ΔOD vs charge density graphs, as shown in Figure 4.7c and Figure 4.7d. Achieved CE values for both material electrodes are presented in Table 1. V_2O_5 -1 electrodes excel over V_2O_5 -2 electrodes, since their higher surface area provides a lot more active Faradaic sites for the electrochemical reactions.

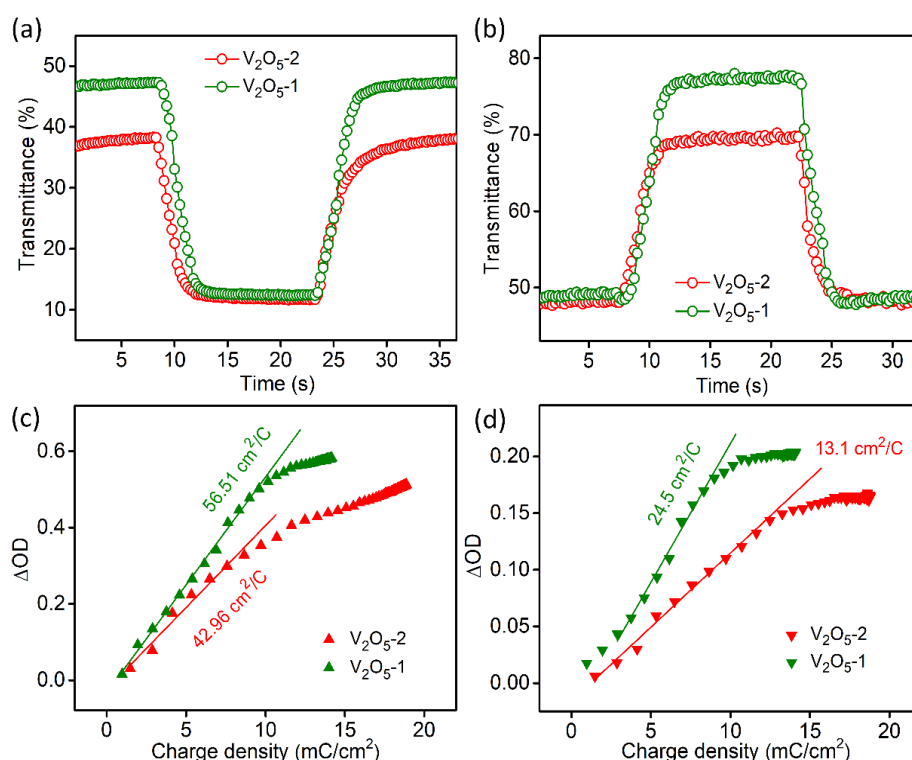


Figure 4.7: Switching times of V_2O_5 -1 and V_2O_5 -2 at (a) 485 nm and (b) 1000 nm under alternating potential with 15 s interval, coloration efficiency plot of both samples (c) 485 nm and (d) 1000 nm

Table 4.1: Comparison of optical modulation values, switching times and coloration efficiency values of V_2O_5 -2 and V_2O_5 -1 electrodes

Sample	ΔT (%)		Coloring time (s)		Bleaching time (s)		Coloration eff. (cm^2/C)	
	485 nm	1000 nm	485 nm	1000 nm	485 nm	1000 nm	485 nm	1000 nm
V_2O_5 -2	28.5	20.4	3	2.4	5.3	3.2	42.96	13.1
V_2O_5 -1	35	26.5	2.9	2.1	3.4	2.6	56.51	24.5

4.3.1.4. Impedance measurement on V_2O_5 electrodes

Electrochemical impedance spectroscopy (EIS) measurements were conducted in a three-electrode set-up for a better understanding of the charge transfer kinetics of V_2O_5 electrodes. The study was performed using an AC signal of 10 mV amplitude with a frequency range of 10 mHz to 100 kHz at the open circuit voltage.

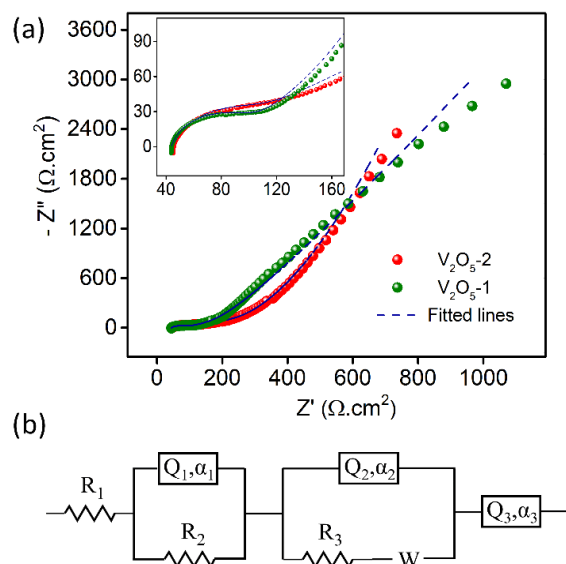


Figure 4.8: (a) Nyquist plots of the V_2O_5 samples, and (b) the equivalent circuit diagram used for fitting impedance data

Figure 4.8a presents the Nyquist plots along with the fitted data. An equivalent circuit was used for modelling the EIS data (Figure 4.8b), where W is the Warburg impedance, 'R's denote resistances and 'Q's denote the constant phase elements (CPE) which refer to the non-ideality of the electrodes. It is defined as $Q = (Q_0 * (j\omega)^\alpha)^{-1}$; where, Q_0 is the pseudo-capacitance and α is a dimensionless parameter, which accounts for the non-ideality, when α is 0, it's purely resistive and for ideal capacitors, α is 1.[40] R_1 in the circuit is attributed to the bulk solution resistance. The depressed semicircle in high and medium frequency regions of the spectra is due to two different types of charge propagation phenomena within the system. The first process, modelled with a resistor (R_2) in parallel to a CPE (Q_1) at high frequency region is either related to the passage of Li^+ ions through a passivation film or through the electrode/electrolyte interface. The resistance R_2 arises due to the mismatch in conductivity at the interface during the charge transfer process. The second process at the medium frequency region is mainly attributed to a Faradaic process limited by the adsorption of Li^+ ions on the surface of V_2O_5 electrodes. In the circuit diagram, it is presented by a parallel combination of a resistor R_3 , which is associated with the resistance of the electro-adsorption process and a

constant phase element Q_2 , related to the redox active surface phenomenon. W corresponds to the solid-state diffusion of Li^+ ions through the pores of V_2O_5 nanoplates. The final circuit element Q_3 is linked to the charging of a crystalline structure by Li^+ ion intercalation at very low frequencies.[41, 42] Additionally, from EIS data analysis, it can also be realized that the overall electrochemical reaction of V_2O_5 electrodes is governed by both diffusion and adsorption processes. Different resistive elements introduced to explain different physical processes are compared in Table 4.2 for the electrodes. Analyzing the impedance data and previous results it can be concluded that the overall reaction kinetics and electrochromic performances of V_2O_5 -1 material are superior to that of V_2O_5 -2 due to its higher surface area. Hence, V_2O_5 -1 electrodes were deployed for further measurements related to energy storage.

Table 4.2: Comparison of resistance values obtained from modelling the Nyquist plots

Films	R_1 (Ωcm^2)	R_2 (Ωcm^2)	R_3 (Ωcm^2)	Measurement error (%)
V_2O_5 -1	43.87	50.2	58.1	< 3.31
V_2O_5 -2	45.31	97.1	60.3	< 2.95

4.3.1.5. Scan rate dependent cyclic voltammetry measurement

Scan rate dependent CV data were collected for both V_2O_5 electrodes for separating the current contributions originating from surface and diffusion-controlled processes. CV measurement performed at varying scan rates from 2 to 100 mVps was presented in Figure 4.9a for V_2O_5 -2 electrode. With the increase in scan rate the anodic and cathodic peaks shift towards more positive and negative potentials respectively, which indicates that there is concentration polarization of Li^+ ions at the electrode-electrolyte interface at a higher scan rate.[43] The peak current densities of CV and the scan rates are connected by a relation; $i = av^b$, where v is sweep rate and a , b are adjustable parameters. When b is close to 1, it suggests the reaction is governed by a surface-controlled process and for the reactions purely influenced by diffusion process, b value is nearly 0.5. Figure 4.9b presents $\log(i)$ vs $\log(v)$ plot and the extracted b value is ~ 0.72 for V_2O_5 -2 electrode, which implies that the reactions are controlled by both surface and diffusion-controlled processes. As presented in Figure 4.9c and Figure 4.9d, a similar measurement was done for V_2O_5 -1 sample also and b value was found to be ~ 0.74 suggesting the involvement of similar reaction mechanisms. The current response (i) depends on surface-controlled (a_1v , includes electrical double layer capacitance and surface controlled redox pseudo-capacitance) and diffusion-controlled processes ($a_2v^{1/2}$), total current can be written as a combination of both, as given below –

Chapter 4

$$i = a_1v + a_2v^{1/2}$$

$$\text{or, } i/v^{1/2} = a_1v^{1/2} + a_2$$

From the slope and intercept of the graph, $i/v^{1/2}$ vs $v^{1/2}$ (Figure 4.9e), a_1 and a_2 coefficients are determined and in the histogram plot of Figure 4.9f, deconvoluted current contributions are presented at different scan rates for V_2O_5-1 sample.[18] With increase in scan rate the contribution of diffusion towards total current gradually decreases as Li^+ ions do not get sufficient time to intercalate into the material.

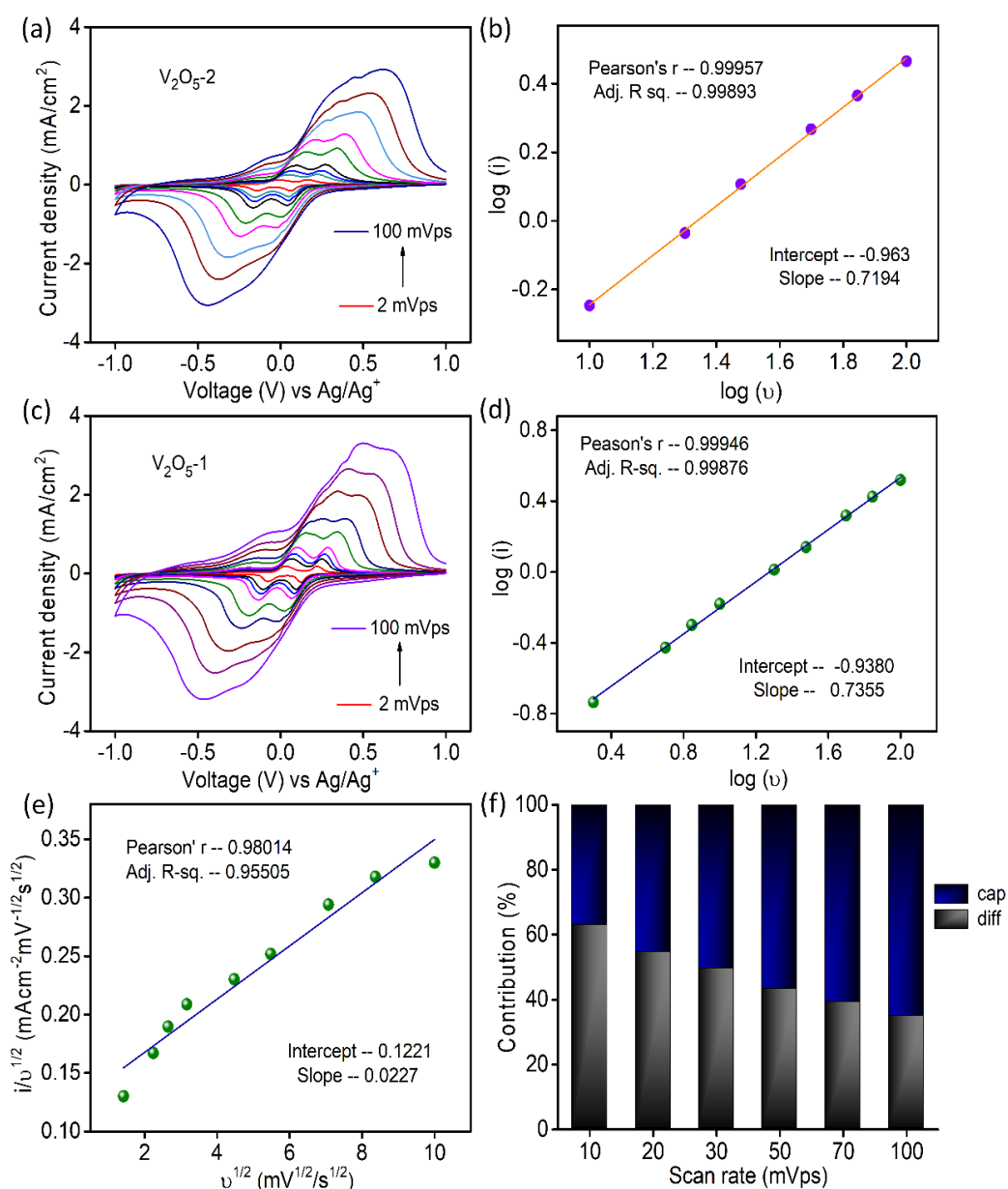


Figure 4.9: Scan rate dependent CV data and $\log(i)$ vs $\log(v)$ plot for (a)-(b) V_2O_5-2 and (c)-(d) V_2O_5-1 samples, (e) $i/v^{1/2}$ vs $v^{1/2}$ plot for V_2O_5-1 electrode and (f) histogram plot shows the decoupling of current contributions with scan rate

4.3.1.6. Electrochromic supercapacitor measurement on V₂O₅ electrode

Galvanostatic charge-discharge (GCD) data (Figure 4.10a) for V₂O₅-1 electrodes were recorded over a potential window of +1 V to -1 V (vs Ag/Ag⁺) at varying current density from 0.02 mA/cm² to 0.7 mA/cm². The non-linear discharge curves consist of different segments – (a) an IR drop at the start of discharge can be seen due to the internal resistance of the system, (b) a steep linear section is due to the electrical double layer formation and (c) the plateau regions in each segment of the GCD profiles, which arise due to the Faradaic reactions, confirming the pseudocapacitive nature of V₂O₅. [44, 45] The areal capacitances were calculated from the charge-discharge data according to the standard formula presented as follows [46]–

$$C_a = (I \cdot \Delta t) / (A \cdot \Delta V)$$

where I is the discharge current density, Δt is the discharge time, A is the geometric area of working electrodes and ΔV is the IR drop corrected potential window. Highest areal capacitance value, obtained from charge-discharge graphs was 13.44 mF/cm² at a discharge current density of 0.02 mA/cm². As the discharge current density increases to 0.7 mA/cm² the areal capacitance value decreases to 11.89 mF/cm², sustaining 88.5% of its capacitance value at 0.02 mA/cm².

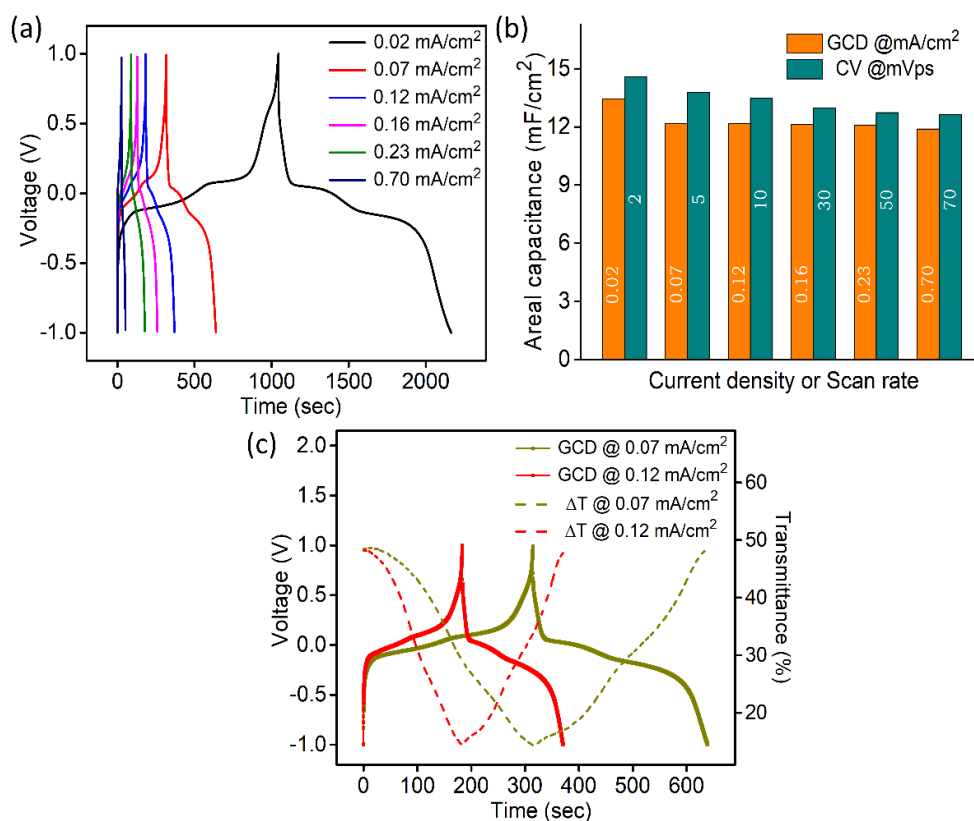


Figure 4.10: (a) GCD plots at different current densities, (b) comparison of areal capacitances calculated from CV and GCD measurements, (c) in-situ transmission data at 485 nm synchronized with the GCD data at different current densities

Capacitance values for V₂O₅-1 electrodes were also extracted from the CV data based on the following equation [47]–

$$C_a = \int idV / (2 * v * A * \Delta v)$$

where $\int idV$ is the area under the curve of a CV at a specific scan rate, v is the scan rate of CV, A is the geometrical area of the electrode and Δv is the potential window in which CV is recorded. The areal capacitance values obtained from CV curves (Figure 4.9c) varies from 14.6 to 12.64 mF/cm² with scan rate ranging from 2 to 70 mVps and these values are presented in Figure 4.10b to confirm the agreement of results derived from both CV and GCD techniques. In-situ optical response at 485 nm synchronized with the GCD curves at two different current densities are presented in Figure 4.10c. During charging the color of the electrode turns yellow and the corresponding transmittance goes down, while the color gradually changes to bluish gray during discharging and the transmittance goes up. Overall, an optical contrast value of ~34% at 485 nm is exhibited by the V₂O₅-1 electrode upon charging and discharging in a three-electrode system.

4.3.2. Positive electrode material (PANI)

PANI is a conducting polymer, which consists of two main repeating units, namely reduced benzenoid and oxidized quinoid rings, relative abundance of which decides the oxidation states and the electrical and optical properties of PANI.[48] PANI exists in three discernible oxidation states. During electrochemical reactions, it switches between these states and gives rise to different colors and properties. These three prominent states are – (i) completely reduced leucoemeraldine base (LB) state containing only benzenoid units, which is nearly transparent or light yellow in color, (ii) fully oxidized pernigraniline base (PEB) state (blue in color) consisting of repeated units of benzenoid and quinoid rings and (iii) partially oxidized emeraldine base (EB) state (green in color) which is the most stable form of PANI in ambient atmosphere.[48, 49] Figure 4.11 presents the typical structures of PANI with different colors, during redox reactions in electrolytes containing X⁻ anions.

Electronic energy bands of a common conducting polymer evolve due to the overlap of π orbitals. In neutral state, their bandgap is defined as the difference between the highest occupied molecular orbital (HOMO) and lowest unoccupied molecular orbital (LUMO),

similar to other semiconducting materials and colors appear due to the intrinsic π - π^* electronic transitions. Removal or addition of electrons along with the movement of charge balancing counter ions causes the structural changes in the polymeric chains, leading to the evolution of positively or negatively charged polaronic and bipolaronic states respectively. Oxidation of conducting polymers leads to the generation of mid-bandgap states as shown in Figure 4.11b, and successively creates new lower energy electronic transitions lying in the near-infrared wavelength range. Electronic transitions involving these mid-bandgap states and HOMO, LUMO levels give rise to the rich variety of hues in conducting polymers.[50, 51]

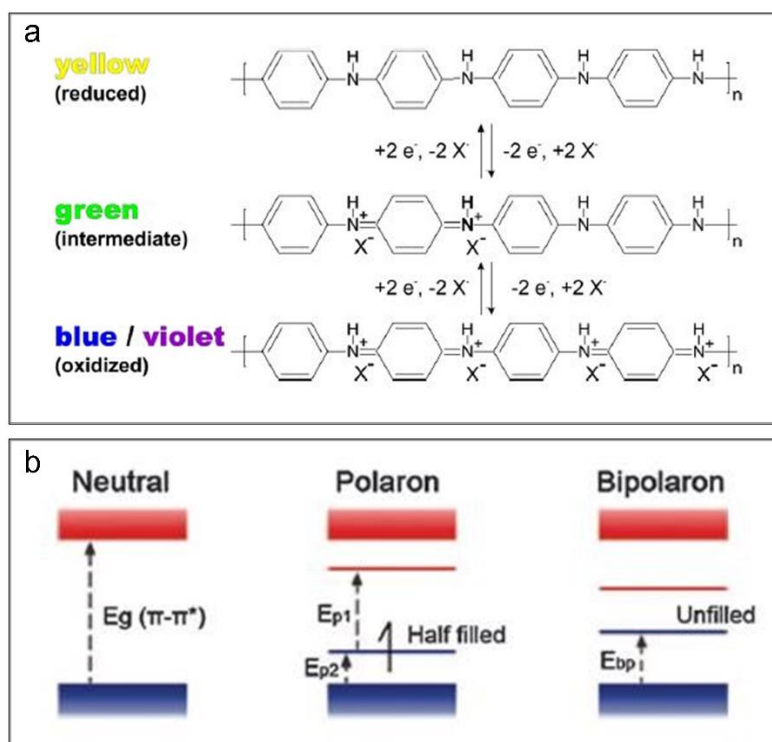


Figure 4.11: (a) PANI structures at their different oxidation states and the corresponding redox reactions, where X is an anion, figure taken from ref. [52], (b) schematic shows the electronic transitions and change in the band gap for a common conducting polymer upon oxidation, figure taken from ref. [51]

4.3.2.1. Morphology and material characterization

As mentioned in the experimental section, PANI films were electrodeposited on FTO substrates. The images of the film at different magnifications, presented in Figure 4.12a-12c, show that the film consists of an array of nanofibers of PANI. This porous nature of the film is conducive to the passage of ions and increases the effective contact area of the electrode material with the electrolyte.

The chemical thumbprints were manifested by ATR-FTIR spectrum as reported in Figure 4.12d. The peak at 790 cm^{-1} is due to out of plane bending vibration of C-H on the benzenoid rings. The absorption peak at 1128 cm^{-1} corresponds to the in plane vibration of C-H present in the aromatic rings. The peaks at 1244 cm^{-1} and 1295 cm^{-1} are attributed to the stretching of C-N bond of aromatic amine. Presence of benzenoid and quinoid ring vibrations of the PANI chains are confirmed by the absorption peaks at 1483 cm^{-1} and 1558 cm^{-1} respectively.[10, 26, 27]

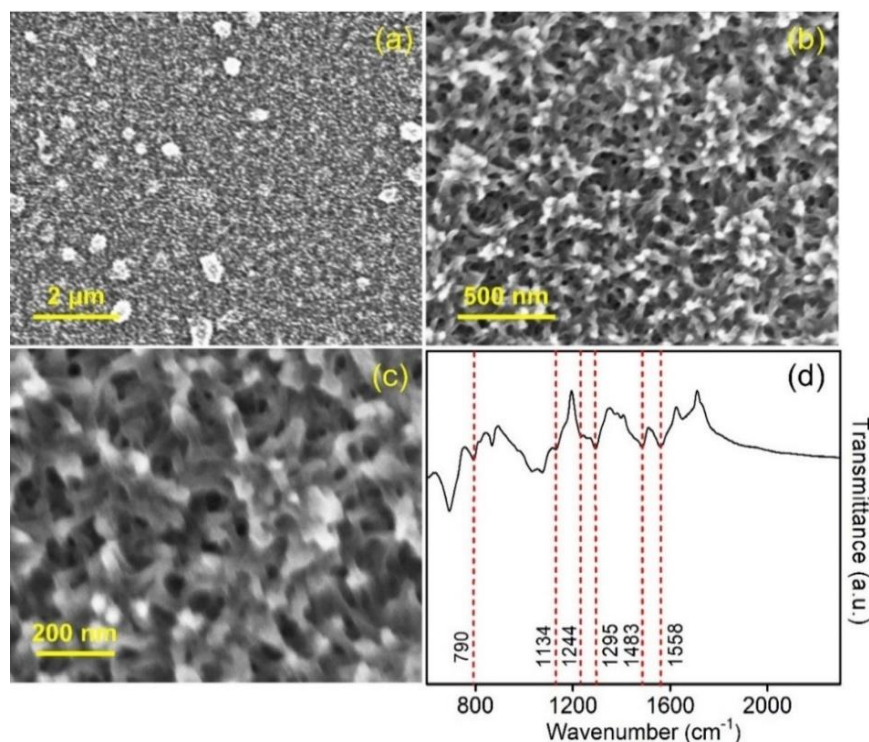
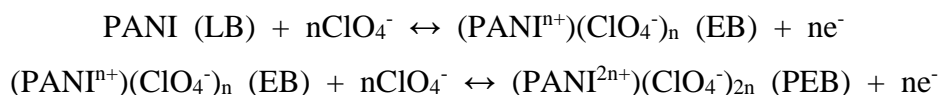


Figure 4.12: (a)-(c) FESEM images and (d) ATR-FTIR data of PANI film

4.3.2.2. Electrochemical measurements on PANI electrodes

Spectroelectrochemical studies of PANI electrodes were performed in 1 M LiClO_4/PC electrolyte in a similar three-electrode set-up like V_2O_5 electrodes. The electrochemical reaction that drives the interchange of PANI within its different forms can be given as [53, 54]–



Two pairs of redox peaks arise in the CV profile of PANI due to the doping/dedoping of anions, as presented in Figure 4.13. The first redox couple at lower potentials is attributed to the transition between LB and EB state and the second pair of peaks is due to the switch between EB and PEB state as described in the above reactions.

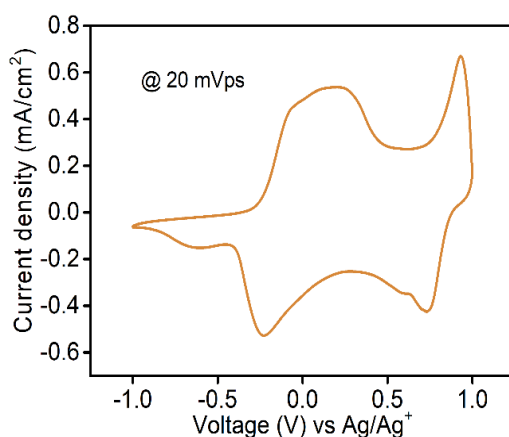


Figure 4.13: CV of PANI film in three-electrode set-up at 20 mVps scan rate in 1 M LiClO₄/PC

Transmission spectra of PANI electrodes at different potentials (during anodic scan from -1 V to +1 V vs Ag/Ag⁺ electrode) are shown in Figure 4.14a. The corresponding film photographs are displayed in Figure 4.14b. The transmission data at two terminal potentials (+1 V and -1 V vs Ag/Ag⁺) and the corresponding optical modulation spectra are plotted in Figure 4.14c. Highest change in transmittance in PANI films was found nearly 75% at 650 nm. In-situ optical modulation of the film at 650 nm was measured by CV at 30 mVps scan rate, presented in Figure 4.14d.

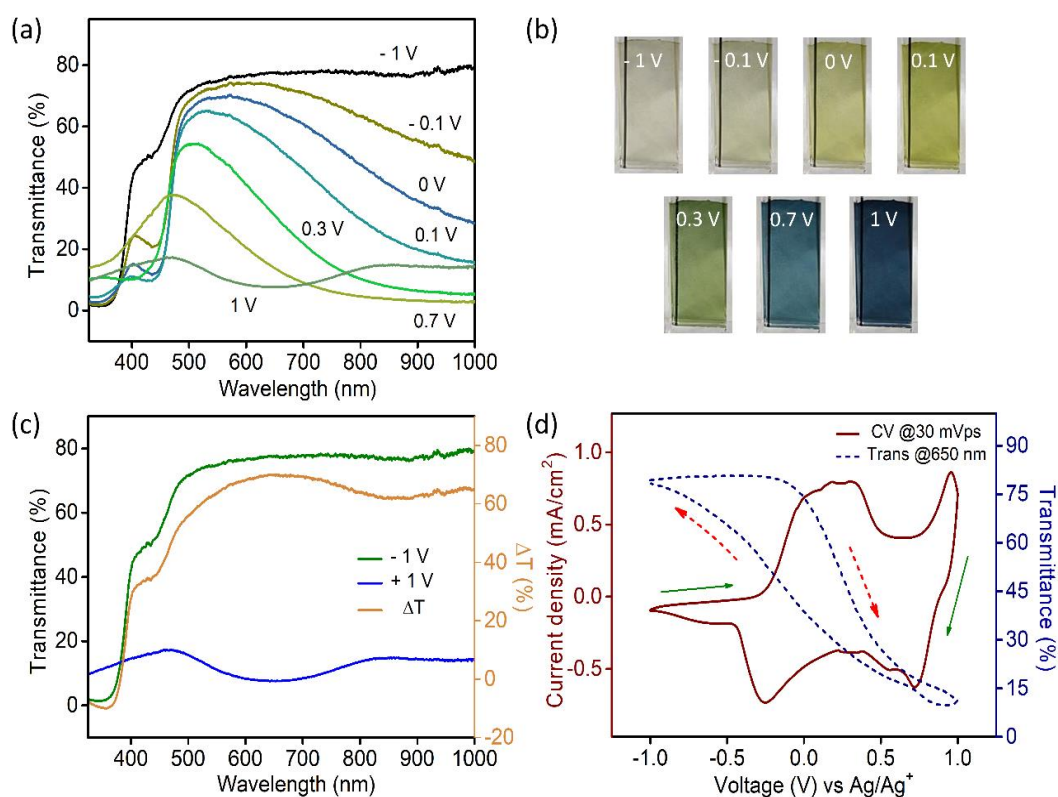


Figure 4.14: Transmission spectra and (b) digital photographs of PANI electrodes at different applied biases; (c) transmission data at +1 V and -1 V along with the optical modulation spectra

(orange curve); (d) CV data of PANI film (wine curve) at 50 mVps scan rate as well as the in-situ change in transmission at 650 nm (blue dotted line).

Scan rate dependent CV data for PANI electrode is shown in Figure 4.15a. Figure 4.15b presents the $\log(i)$ vs $\log(v)$ plot and b value comes out to be nearly 0.9. Further, the plots shown in Figure 4.15d conclude that although the current density of PANI films mostly emerges due to the capacitive process, contribution also comes from the intercalation of ions into the material.

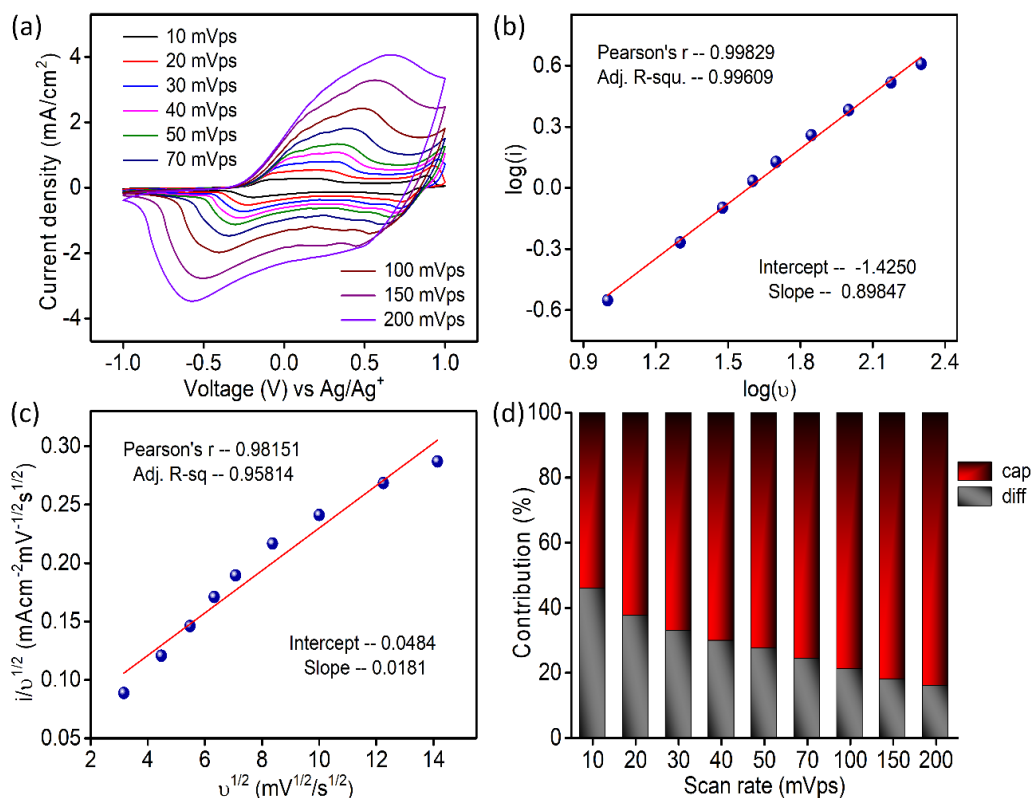


Figure 4.15: (a) Scan rate dependent CV data for PANI electrode, (b) $\log(i)$ vs $\log(v)$ plot, (c) $i/v^{1/2}$ vs $v^{1/2}$ plot and (d) deconvoluting current contributions with scan rate

Figure 4.16a presents the GCD data of PANI film at varying current densities. Areal capacitance value ranges from 13.69 mF/cm² to 11.1 mF/cm² as current density switches from 0.02 mA/cm² to 0.7 mA/cm². Alike the V₂O₅ electrodes, the charge-discharge profiles, in this case, are also non-linear, which point towards the presence of surface-controlled Faradaic processes. The areal capacitance values for PANI films were also extracted from CV curves. Highest value obtained was 12.3 mF/cm² at 10 mV/s scan rate. The obtained values are compared in Figure 4.16b. With the increase in scan rate of CV or the current density in charge-discharge, the areal capacitance value decreases due to the inaccessibility of reaction sites of the active material.[55] The in-situ change in transmittance at 650 nm during charging-

discharging of PANI electrodes at different current densities are presented in Figure 4.16c. During charging, the structural units of PANI get oxidized, which demands the doping of ClO_4^- ions into the film to maintain the charge balance and the process is accompanied by a transmittance drop in PANI films. During discharging, reduction of PANI takes place with the simultaneous return of ClO_4^- ions to the solution and the film gains its transparency again.

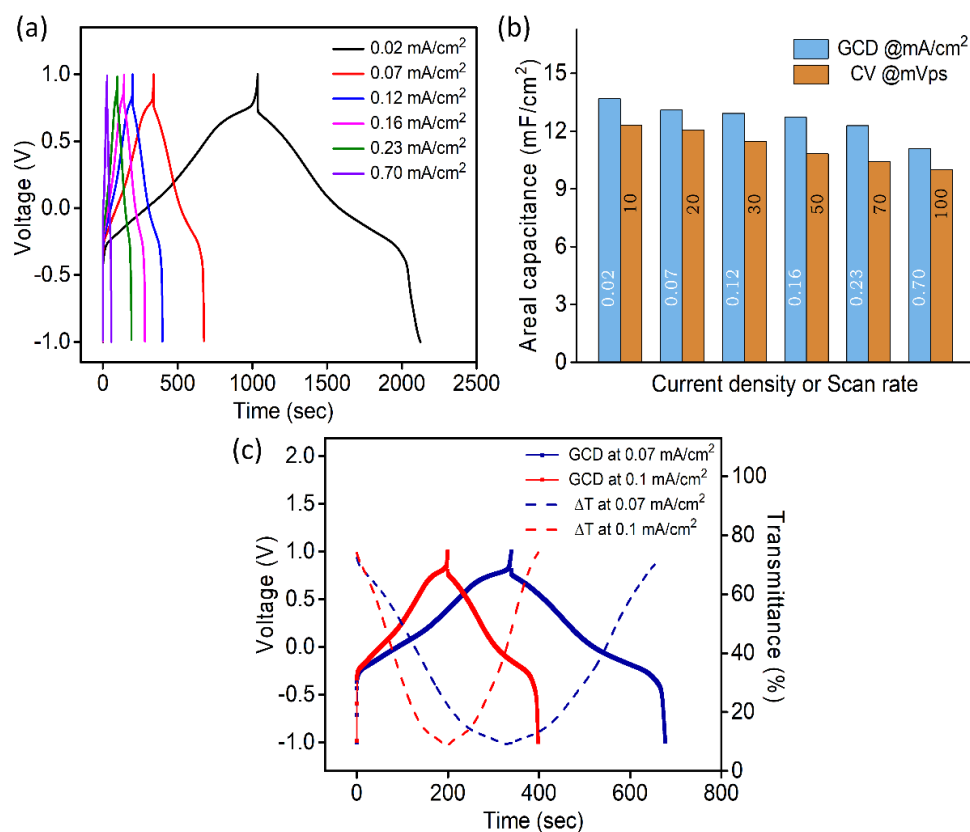


Figure 4.16: (a) GCD curves at different current densities; (b) comparison of areal specific capacitance values obtained from CV and GCD data; (c) in-situ change in transmittance at 650 nm synced with GCD curves at different current densities.

4.3.3. Multicolored electrochromic asymmetric supercapacitor

CV curves collected for both V_2O_5 and PANI electrodes in 1 M LiClO_4/PC electrolyte in three-electrode set-up are presented in Figure 4.17, which sustain our choice of using V_2O_5 as negative electrode and PANI as positive electrode in assembling multicolored electrochromic asymmetric supercapacitor (MECASC) for voltage window up to 2 V.

To obtain better performance from an asymmetric supercapacitor, the charge balance between its two electrodes should be maintained; i.e., $q^+ = q^-$, where q^+ and q^- correspond to the charges of positive and negative electrodes respectively and $q = I \cdot \Delta t$, where I and Δt are as defined earlier. In order to do that, the first step was to take the charge-discharge profile of

V₂O₅ electrode at a fixed current density, then accordingly the electrodeposition time (150 sec) of PANI film was so adjusted that, the PANI film matches the capacity of V₂O₅.

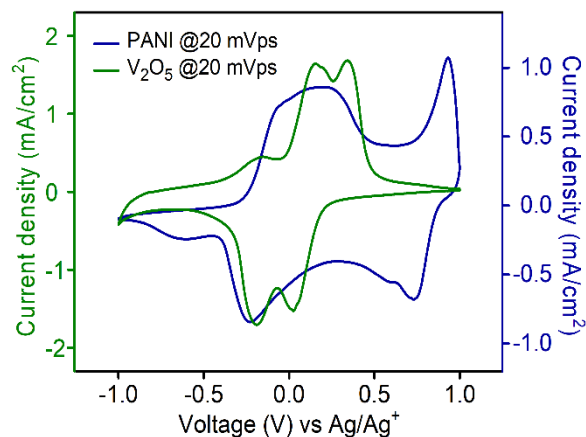
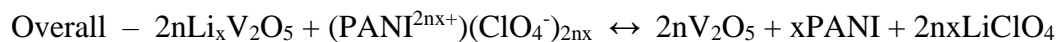
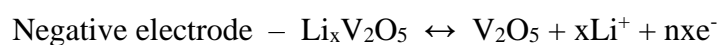


Figure 4.17: CV of PANI and V₂O₅ electrodes separately measured at three-electrode set-up in the identical voltage window (± 1 V vs Ag/Ag⁺) with 1 M LiClO₄/PC electrolyte at 20 mVps scan rate

4.3.3.1. Electrochemical measurements

Two-electrode CVs of the MECASC were performed in a potential window of 0-2 V at varying scan rates from 10 to 100 mVps (Figure 4.18a). Semi-rectangular shape of CV along with the presence of redox peaks affirms the synergistic effect of both double layer capacitance and pseudo-capacitance.[56] During anodic scan, Li⁺ ion intercalates in V₂O₅ electrode and simultaneously ClO₄⁻ ions get doped into PANI film. During discharging, both cations and anions leave the materials and get to the electrolyte besides producing electricity. The half-cell reactions and the overall cell reaction for the whole process can be depicted as –



The contribution of Faradaic and surface controlled processes in current contributions were investigated, as shown in Figure 4.18b-d. The plots of log(i) vs log(v) at different voltages are given in Figure 4.18b and the extracted b values signify that the overall reaction is dominated by surface controlled capacitive process. Separation of capacitive and diffusive contribution in current at different scan rates is presented in Figure 4.18d.

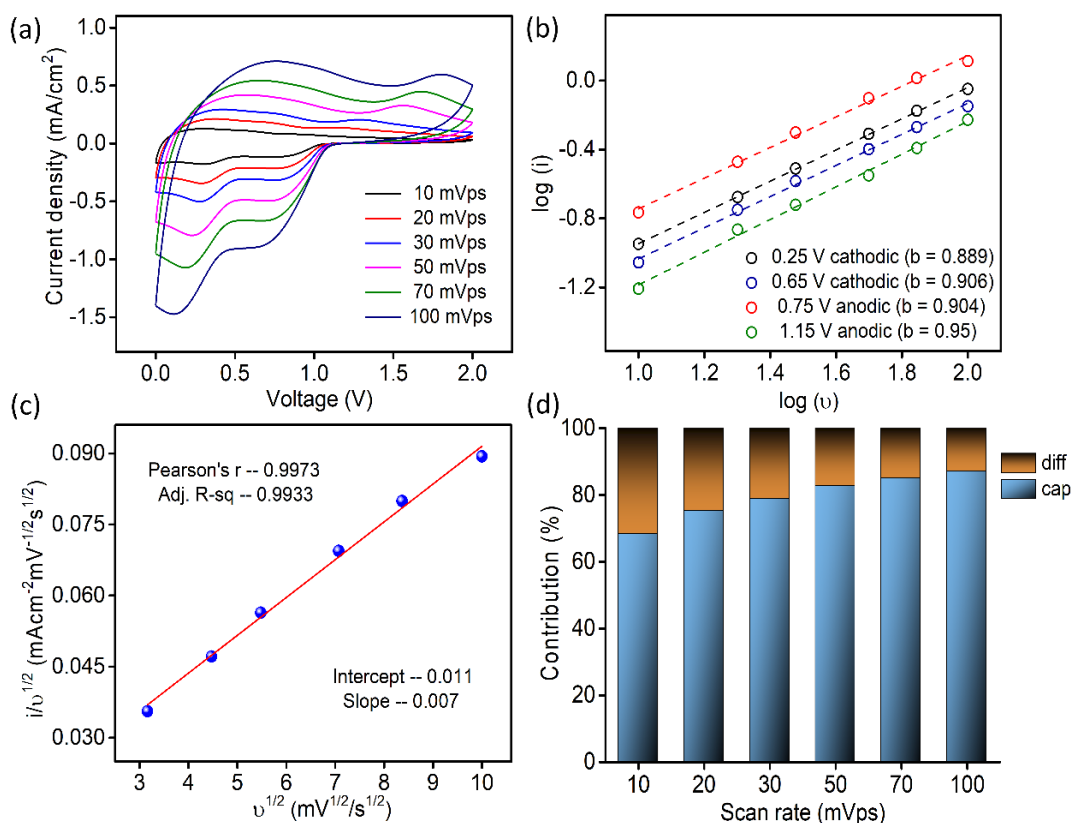


Figure 4.18: (a) CV of MECASC measured in two-electrode set-up at varying scan rates, (b) $\log(i)$ vs $\log(v)$ plot for the asymmetric supercapacitor system at different voltages, (c) $i/v^{1/2}$ vs $v^{1/2}$ graph, (d) separating the current contributions at different scan rates

4.3.3.2. Spectro-electrochemistry and supercapacitor measurements

Transmission spectra of MECASC were taken at different voltages during anodic and cathodic scans within the voltage window of 0-2 V, as presented in Figure 4.19a-b. Transmission spectra at two end voltages and the optical modulation spectra of the system are shown in Figure 4.19c. Transmission modulation reaches the highest value of ~13.5% at 580 nm. At 0 V, the whole system looks yellowish green in color (individually, V₂O₅ and PANI films colors are yellow and yellowish green respectively) and with the increase in applied bias PANI and V₂O₅ gradually get oxidized and reduced respectively. In consequence, the color of the device changes to dark blue (where V₂O₅ and PANI films change to bluish gray and dark blue color respectively). CV profiles (at 30 mVps sweep rate) at different working voltage windows are presented in Figure 4.19d along with the dynamic changes in transmissions at 580 nm; which are well consistent with the change in current density. As the voltage window increases beyond 1 V, surface-redox reactions start to appear prominently, accompanied by the increase in optical modulation value up to 40% of its initial value as depicted in Figure 4.19d.

When operational voltage gradually increases from 1 to 2 V, the energy density calculated according to the equation; $E=1/2*CV^2$ elevates from 1.17×10^{-3} to 2.93×10^{-3} mWh/cm².

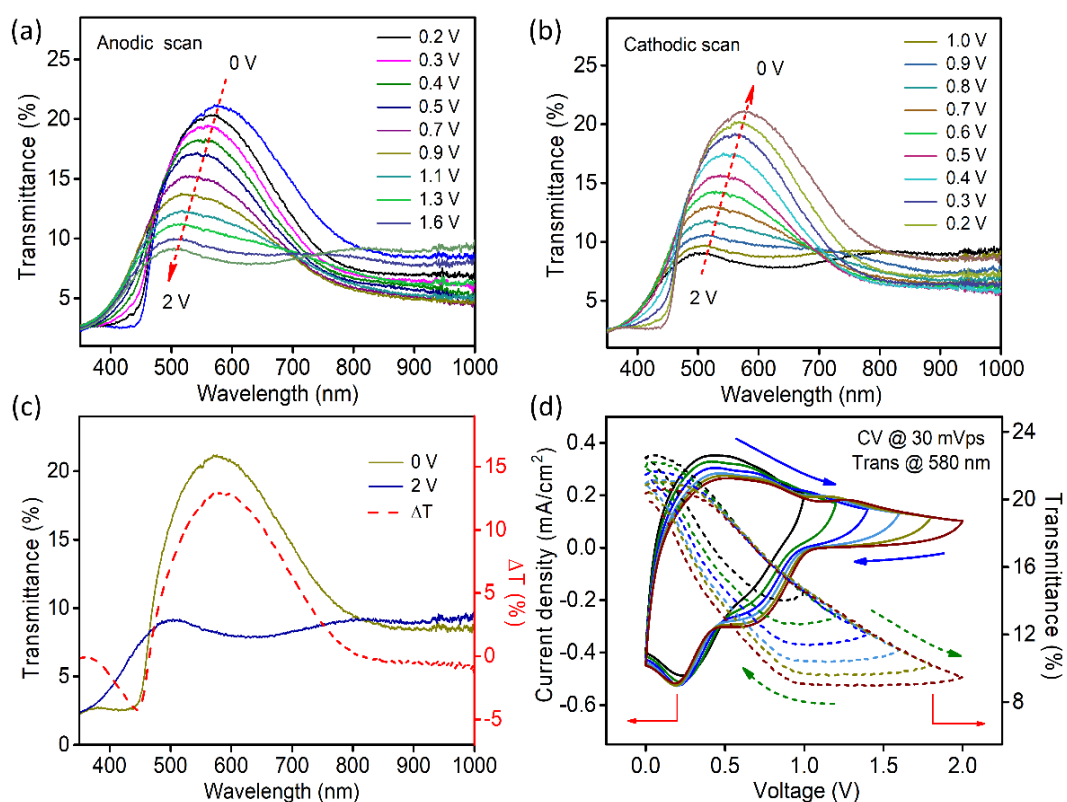


Figure 4.19: Gradual change in transmission spectra of MECASC during (a) anodic and (b) cathodic scan; (c) Transmission spectra of the device at two terminal voltages and the optical modulation spectra (dotted line), (d) CV at varying potential windows with the simultaneous in-situ transmission changes at 580 nm

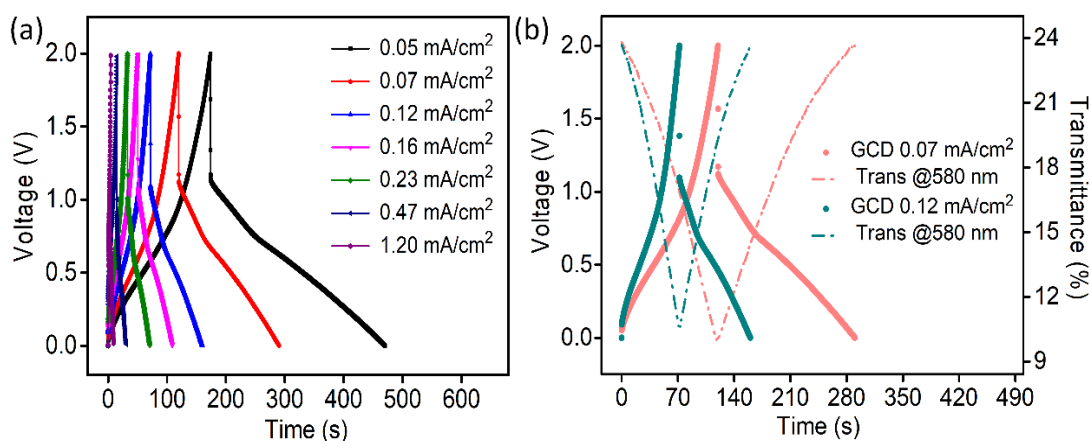


Figure 4.20: (a) GCD profiles at different current densities, (b) in-situ transmission changes at 580 nm in harmony with GCD profiles at two different current densities.

GCD measurements (Figure 4.20a) for the MECASC module were performed at different current densities ranging from 0.05 to 1.2 mA/cm² within the operational voltage

window of 2 V. Presence of nonlinearity in GCD profiles indicates the existence of Faradaic reactions in PANI and V₂O₅. Areal capacitance touches a maximum value of 12.27 mF/cm² at 0.05 mA/cm² current density with an energy density of 2.21x10⁻³ mWh/cm². At 24 times higher current density of 1.2 mA/cm², 58.2% areal capacitance value i.e., 7.14 mF/cm² can be retained compared to that at 0.05 mA/cm² and the energy density decreases to 5.7x10⁻⁴ mWh/cm². Figure 4.20b presents the optical modulation synced with GCD profiles at two different current densities. Optical modulation at 580 nm reduces from 13.7% to 12.9% with the increase in current density from 0.07 to 0.12 mA/cm² with a simultaneous decrement in areal capacitance from 10.63 to 9.52 mF/cm². The probable reason behind this is the inaccessibility of active electrode materials for charge storage as there is a limitation in the migration of ionic species with the increase in current density.[57]

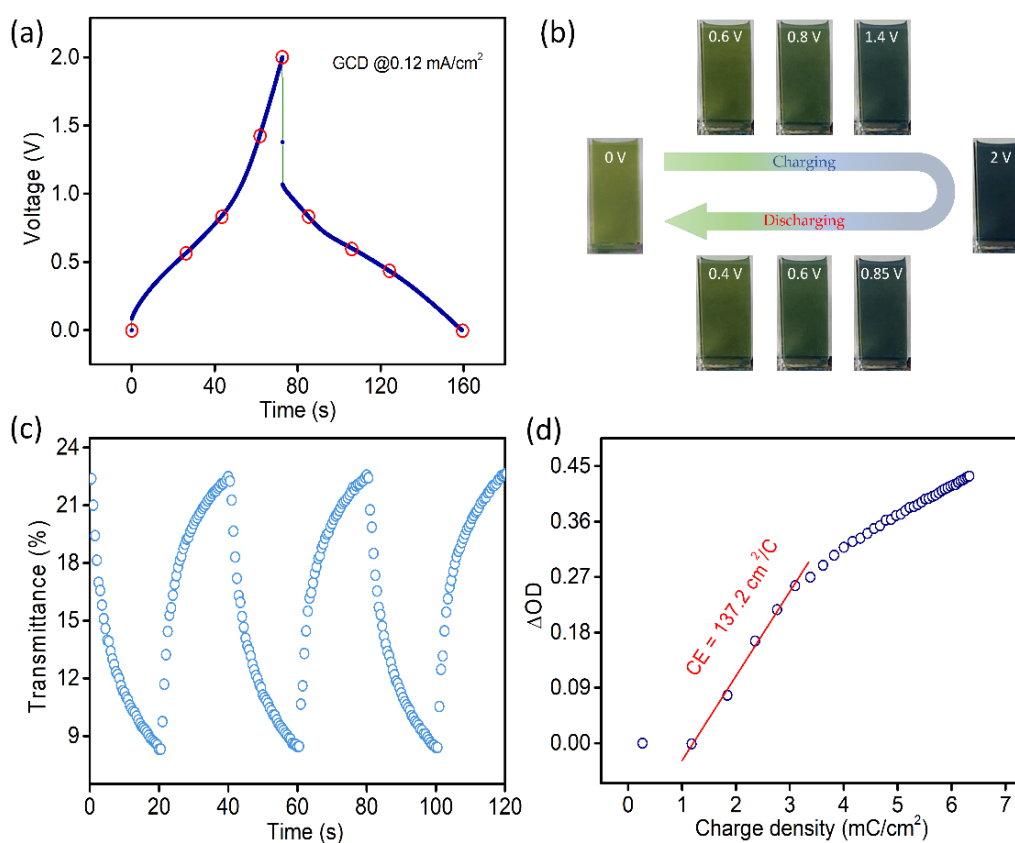


Figure 4.21: (a) GCD profile of MECASC at 0.12 mA/cm² current density, (b) photographs of the system at different voltages during charging and discharging as assigned by the red circles in Figure 4.20a; (c) switching times of the module at 580 nm by applying 0 V and 2 V potential alternatively with 20 s interval; (d) coloration efficiency of the system at 580 nm.

Figure 4.21a shows the GCD profile of MECASC at 0.12 mA/cm² current density. The photographs of the module are presented in Figure 4.21b at different instants of charging and discharging as shown by the red circles in the GCD curve in Figure 4.21a. This well coordinated

behavior of color changes (yellowish green, dark green, greenish blue, blue and dark blue) during charging-discharging of the electrodes helps to uniquely identify the state of charge of the system. Further to understand the performance of MECASC system, the switching times and the coloration efficiency were calculated. Switching times were determined according to the description previously given in section 3.1.2, by applying potentials alternating between 0 V and 2 V. Calculated coloration and bleaching times for the system were 16.4 s and 12.9 s respectively. Further, coloration efficiency (CE) was calculated at 580 nm wavelength according to Equation 2 and a high CE value of $137.2 \text{ cm}^2/\text{C}$ was obtained for the module.

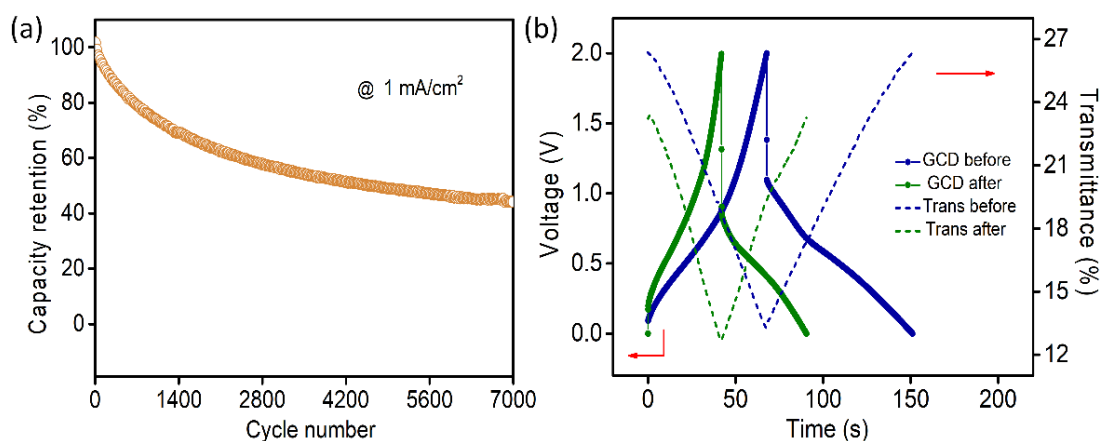


Figure 4.22: (a) Cycling performance of MECASC up to 7000 cycles; (b) GCD profiles of the system at $0.12 \text{ mA}/\text{cm}^2$ and dynamic in-situ transmission modulations at 580 nm before and after cycling.

Cycling performance is a measure of the life span of a device for practical applications. By conducting the cyclic stability measurement at a high current density of $1 \text{ mA}/\text{cm}^2$, it is observed that the supercapacitor can sustain nearly 50 % of its initial capacitance value after 7000 cycles (Figure 4.22a). This kind of capacity decay is quite common among V_2O_5 electrodes.[35, 38, 58, 59] The galvanostatic charge-discharge (GCD) curves of the module at $0.12 \text{ mA}/\text{cm}^2$ current density alongwith the dynamic change of its transmission at 580 nm wavelength before and after cycling are presented in Figure 4.22b. After cycling, transmission modulation value at 580 nm reduces by $\sim 18.47 \%$ of its initial value. There is lowering in transmittance of the bleached state, which may be caused due to the trapped charge inside the electrodes because of repeated cycling.[60, 61]

The morphology of both V_2O_5 and PANI films were examined by FESEM technique. Figure 4.23 and Figure 4.24 present the FESEM images of V_2O_5 and PANI electrodes respectively at different magnifications ($10 \mu\text{m}$ and $1 \mu\text{m}$) before and after cycling.

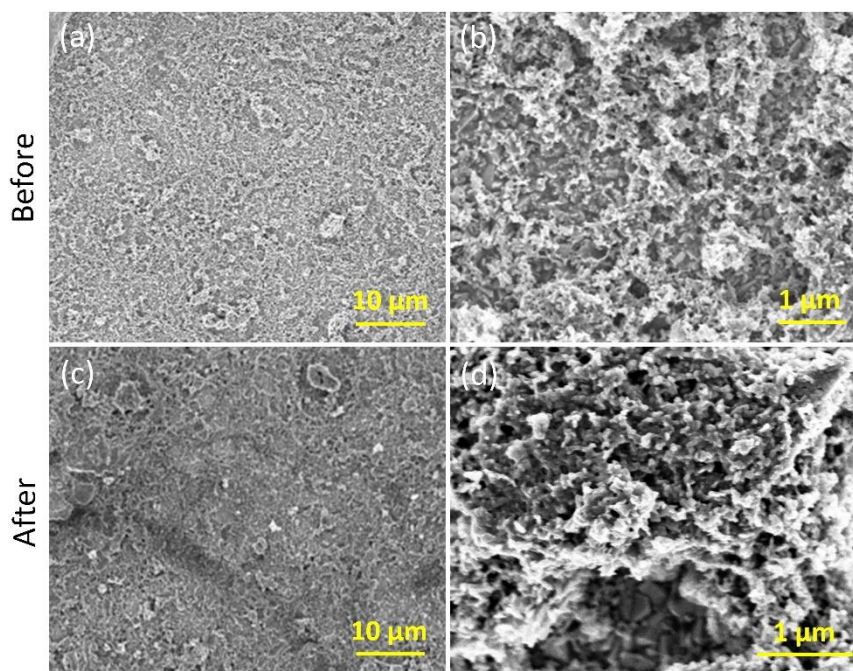


Figure 4.23: Morphology of V_2O_5 films before (a)-(b) and after (c)-(d) cycling in 2-electrode system at different magnifications

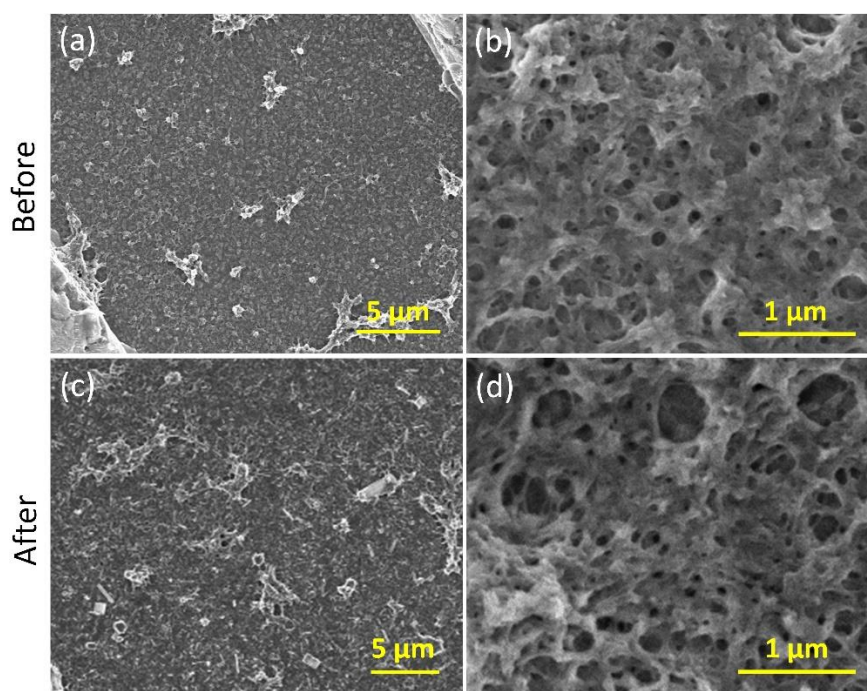


Figure 4.24: Morphology of PANI films before (a)-(b) and after (c)-(d) cycling in 2-electrode system at different magnifications.

For the V_2O_5 electrode, dark patches were noticed on the films after cycling as presented in Figure 4.23c and Figure 4.23d, which are absent in the image, illustrated in Figure 4.23a and Figure 4.23b before cycling. The patches could be the portions of the electrode from where chunks of electrode materials were peeled off during cycling. Figure 4.23b and Figure

4.23d illustrate these aspects with better clarity. This is occurred due to the mechanical stress generated during ion intercalation-deintercalation,[62] causing the capacity fading for V_2O_5 -based materials as mentioned in previous reports.[15, 63, 64] Additionally, no visible color change of the electrolyte was noted after the cycling test. According to other reported literatures, V_2O_5 tends to dissolve in aqueous electrolyte during cycling;[32, 36] on the contrary organic electrolytes effectively decreases the dissolution of V_2O_5 and increase the stability of the electrodes. From Figure 4.24a and 4.24c, not much change in PANI electrode is observed before and after cycling. Closer inspection reveals that the diameters of the pores in the PANI film increased after cycling as presented in Figure 4.24b and 4.24d.

Prototypes of the MECASC (2.5 cm x 4 cm) were assembled to demonstrate the practical applicability. The devices were connected in series, which lit up the green LED for almost 7 mins. The photograph of the devices is presented in Figure 4.25a in their charged states with green LED glowing. Figure 4.25b shows the discharged state of the devices with yellowish green color and LED in off state.

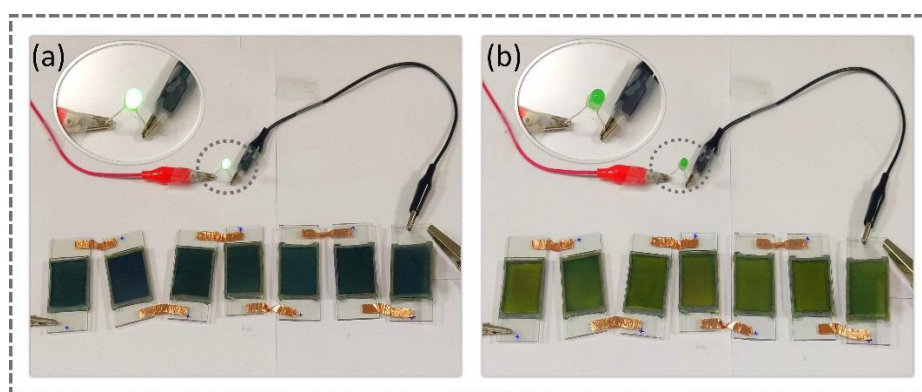


Figure 4.25: photographs demonstrate (a) charged and (b) discharged states of the devices, connected in series; insets show the state of LED in both cases

4.4. Conclusion

MOF-derived V_2O_5 has been successfully synthesized and employed as an electrochromic electrode, which shows large optical modulations with very fast switching times and descent coloration efficiencies. Later the V_2O_5 film was used as the negative electrode for the fabrication of a multicolored electrochromic asymmetric supercapacitor alongside an electrodeposited PANI film, which was deployed as the positive electrode. Owing to its multiple-colored states at different stages of charging and discharging, it enables the direct determination of its energy storage level by naked eye. As an electrochromic energy storage device, it demonstrates a high coloration efficiency of $137.2 \text{ cm}^2/\text{C}$ and an areal capacitance of

12.27 mF/cm² with an energy density of 2.21x10⁻³ mWh/cm² at 0.05 mA/cm² current density. Moreover, this operates as an energy-efficient electrochromic device by eliminating the requirement of energy during bleaching as it recycles the energy stored during charging. In a nutshell, this work resolves the issue of monochromatic color change of a smart energy storage device by its voltage dependent distinct colored states and it is a new stride towards the intelligent automation of the energy storage devices.

4.5. Bibliography

- [1] L.J. Wang, M.F. El-Kady, S. Dubin, J.Y. Hwang, Y. Shao, K. Marsh, B. McVerry, M.D. Kowal, M.F. Mousavi, R.B. Kaner, Flash Converted Graphene for Ultra-High Power Supercapacitors, *Adv. Energy Mater.*, 5 (2015) 1500786.
- [2] P. Simon, Y. Gogotsi, Materials for electrochemical capacitors, *Nat. Mater.*, 7 (2008) 845-854.
- [3] T. Zhu, Y. Yang, Y. Liu, R. Lopez-Hallman, Z. Ma, L. Liu, X. Gong, Wireless portable light-weight self-charging power packs by perovskite-organic tandem solar cells integrated with solid-state asymmetric supercapacitors, *Nano Energy*, 78 (2020) 105397.
- [4] P. Xie, W. Yuan, X. Liu, Y. Peng, Y. Yin, Y. Li, Z. Wu, Advanced carbon nanomaterials for state-of-the-art flexible supercapacitors, *Energy Storage Mater.*, 36 (2021) 56-76.
- [5] Y. Huang, M. Zhu, Z. Pei, Q. Xue, Y. Huang, C. Zhi, A shape memory supercapacitor and its application in smart energy storage textiles, *J. Mater. Chem. A*, 4 (2016) 1290-1297.
- [6] Y. Jiang, M. Cheng, R. Shahbazian-Yassar, Y. Pan, Direct Ink Writing of Wearable Thermoresponsive Supercapacitors with rGO/CNT Composite Electrodes, *Adv. Mater. Technol.*, 4 (2019) 1900691.
- [7] X. Liang, L. Zhao, Q. Wang, Y. Ma, D. Zhang, A dynamic stretchable and self-healable supercapacitor with a CNT/graphene/PANI composite film, *Nanoscale*, 10 (2018) 22329-22334.
- [8] Q. Guo, X. Zhao, Z. Li, D. Wang, G. Nie, A novel solid-state electrochromic supercapacitor with high energy storage capacity and cycle stability based on poly(5-formylindole)/WO₃ honeycombed porous nanocomposites, *Chem. Eng. J.*, 384 (2020) 123370.
- [9] J. Chen, Z. Wang, Z. Chen, S. Cong, Z. Zhao, Fabry–Perot Cavity-Type Electrochromic Supercapacitors with Exceptionally Versatile Color Tunability, *Nano Lett.*, 20 (2020) 1915-1922.

- [10] Y. Zhong, Z. Chai, Z. Liang, P. Sun, W. Xie, C. Zhao, W. Mai, Electrochromic Asymmetric Supercapacitor Windows Enable Direct Determination of Energy Status by the Naked Eye, *ACS Appl. Mater. Interfaces*, 9 (2017) 34085-34092.
- [11] Q. Guo, J. Li, B. Zhang, G. Nie, D. Wang, High-Performance Asymmetric Electrochromic-Supercapacitor Device Based on Poly(indole-6-carboxylic acid)/TiO₂ Nanocomposites, *ACS Appl. Mater. Interfaces*, 11 (2019) 6491-6501.
- [12] Q. Guo, X. Zhao, Z. Li, B. Wang, D. Wang, G. Nie, High Performance Multicolor Intelligent Supercapacitor and Its Quantitative Monitoring of Energy Storage Level by Electrochromic Parameters, *ACS Appl. Energy Mater.*, 3 (2020) 2727-2736.
- [13] S.B. Singh, D.T. Tran, K.-U. Jeong, N.H. Kim, J.H. Lee, A Flexible and Transparent Zinc-Nanofiber Network Electrode for Wearable Electrochromic, Rechargeable Zn-Ion Battery, *Small*, 18 (2022) 2104462.
- [14] L. Zhao, J. Kuang, W. Zhuang, J. Chao, W. Liao, X. Fu, C. Li, L. Ye, H. Liu, Studies on transmittance modulation and ions transfer kinetic based on capacitive-controlled 2D V₂O₅ inverse opal film for electrochromic energy storage application, *Nanotechnology*, 33 (2021) 054001.
- [15] S. Zhang, S. Chen, Y. Luo, B. Yan, Y. Gu, F. Yang, Y. Cao, Large-scale preparation of solution-processable one-dimensional V₂O₅ nanobelts with ultrahigh aspect ratio for bifunctional multicolor electrochromic and supercapacitor applications, *J. Alloys Compd.*, 842 (2020) 155882.
- [16] D. Majumdar, M. Mandal, S.K. Bhattacharya, V₂O₅ and its Carbon-Based Nanocomposites for Supercapacitor Applications, *ChemElectroChem*, 6 (2019) 1623-1648.
- [17] M.M. Margoni, S. Mathuri, K. Ramamurthi, R.R. Babu, V. Ganesh, K. Sethuraman, Hydrothermally grown nano and microstructured V₂O₅ thin films for electrochromic application, *Appl. Surf. Sci.*, 449 (2018) 193-202.
- [18] A. Dewan, S. Sur, R. Narayanan, M.O. Thotiyl, MOF-Derived Carbon Embedded NiO for an Alkaline Zn–NiO Electrochromic Battery, *ChemElectroChem*, 9 (2022) e202200001.
- [19] R.R. Salunkhe, Y.V. Kaneti, Y. Yamauchi, Metal–Organic Framework-Derived Nanoporous Metal Oxides toward Supercapacitor Applications: Progress and Prospects, *ACS Nano*, 11 (2017) 5293-5308.
- [20] Y.-S. Hsiao, C.-W. Chang-Jian, W.-L. Syu, S.-C. Yen, J.-H. Huang, H.-C. Weng, C.-Z. Lu, S.-C. Hsu, Enhanced electrochromic performance of carbon-coated V₂O₅ derived from a metal–organic framework, *Appl. Surf. Sci.*, 542 (2021) 148498.

- [21] T.Q. He, J.H. Li, Z.Z. Luo, Y.Q. Zhang, Y.Y. Zhao, X.T. Zhang, Y.J. Chen, MIL-47(V) Derived V_2O_5 @Carbon Core-Shell Microcuboids with Oxygen Vacancies as Advanced Conversion Cathodes for High-Performance Zinc-Ion Batteries, *Chemelectrochem*, 9 (2022).
- [22] Y. Ding, Y. Peng, W. Chen, Y. Niu, S. Wu, X. Zhang, L. Hu, V-MOF derived porous V_2O_5 nanoplates for high performance aqueous zinc ion battery, *Appl. Surf. Sci.*, 493 (2019) 368-374.
- [23] T. Kim, H. Kim, T.-S. You, J. Kim, Carbon-coated V_2O_5 nanoparticles derived from metal-organic frameworks as a cathode material for rechargeable lithium-ion batteries, *J. Alloys Compd.*, 727 (2017) 522-530.
- [24] F. Carson, J. Su, A.E. Platero-Prats, W. Wan, Y. Yun, L. Samain, X. Zou, Framework Isomerism in Vanadium Metal–Organic Frameworks: MIL-88B(V) and MIL-101(V), *Cryst. Growth Des.*, 13 (2013) 5036-5044.
- [25] H. Liang, R. Li, C. Li, C. Hou, Y. Li, Q. Zhang, H. Wang, Regulation of carbon content in MOF-derived hierarchical-porous NiO@C films for high-performance electrochromism, *Mater. Horiz.*, 6 (2019) 571-579.
- [26] Y. Mohd, R. Ibrahim, M.F. Zainal, Electrodeposition and characterization of Polyaniline films, 2012 IEEE Symposium on Humanities, Science and Engineering Research, IEEE, Kuala Lumpur, 2012, pp. 1301-1306.
- [27] P. Yilmaz, M. Magni, S. Martinez, R.M. Gonzalez Gil, M. Della Pirriera, M. Manca, Spectrally Selective PANI/ITO Nanocomposite Electrodes for Energy-Efficient Dual Band Electrochromic Windows, *ACS Appl. Energy Mater.*, 3 (2020) 3779-3788.
- [28] G. Férey, C. Mellot-Draznieks, C. Serre, F. Millange, J. Dutour, S. Surblé, I. Margiolaki, A Chromium Terephthalate-Based Solid with Unusually Large Pore Volumes and Surface Area, *Science*, 309 (2005) 2040-2042.
- [29] S. Biswas, S. Couck, M. Grzywa, J.F.M. Denayer, D. Volkmer, P. Van Der Voort, Vanadium Analogues of Nonfunctionalized and Amino-Functionalized MOFs with MIL-101 Topology – Synthesis, Characterization, and Gas Sorption Properties, *Eur. J. Inorg. Chem.*, 2012 (2012) 2481-2486.
- [30] W.-C. Fang, Synthesis and Electrochemical Characterization of Vanadium Oxide/Carbon Nanotube Composites for Supercapacitors, *J. Phys. Chem. C*, 112 (2008) 11552-11555.
- [31] Y. Chen, K. Muthukumar, L. Leban, J. Li, Microwave-assisted high-yield exfoliation of vanadium pentoxide nanoribbons for supercapacitor applications, *Electrochim. Acta*, 330 (2020) 135200.

- [32] H. Liu, W. Zhu, D. Long, J. Zhu, G. Pezzotti, Porous V_2O_5 nanorods/reduced graphene oxide composites for high performance symmetric supercapacitors, *Appl. Surf. Sci.*, 478 (2019) 383-392.
- [33] M. Sathiya, A.S. Prakash, K. Ramesha, J.M. Tarascon, A.K. Shukla, V_2O_5 -Anchored Carbon Nanotubes for Enhanced Electrochemical Energy Storage, *J. Am. Chem. Soc.*, 133 (2011) 16291-16299.
- [34] C.Y. Foo, A. Sumboja, D.J.H. Tan, J. Wang, P.S. Lee, Flexible and Highly Scalable V_2O_5 -rGO Electrodes in an Organic Electrolyte for Supercapacitor Devices, *Adv. Energy Mater.*, 4 (2014) 1400236.
- [35] M. Li, G. Sun, P. Yin, C. Ruan, K. Ai, Controlling the Formation of Rodlike V_2O_5 Nanocrystals on Reduced Graphene Oxide for High-Performance Supercapacitors, *ACS Appl. Mater. Interfaces*, 5 (2013) 11462-11470.
- [36] H. Zhang, X. Han, R. Gan, Z. Guo, Y. Ni, L. Zhang, A facile biotemplate-assisted synthesis of mesoporous V_2O_5 microtubules for high performance asymmetric supercapacitors, *Appl. Surf. Sci.*, 511 (2020) 145527.
- [37] B.D. Boruah, B. Wen, M. De Volder, Light Rechargeable Lithium-Ion Batteries Using V_2O_5 Cathodes, *Nano Lett.*, 21 (2021) 3527-3532.
- [38] J. Yang, T. Lan, J. Liu, Y. Song, M. Wei, Supercapacitor electrode of hollow spherical V_2O_5 with a high pseudocapacitance in aqueous solution, *Electrochim. Acta*, 105 (2013) 489-495.
- [39] A. Dewan, S. Halder, R. Narayanan, Multi-shelled NiO hollow microspheres as bifunctional materials for electrochromic smart window and non-enzymatic glucose sensor, *J. Solid State Electrochem.*, 25 (2021) 821-830.
- [40] M. Holzappel, A. Martinent, F. Alloin, B. Le Gorrec, R. Yazami, C. Montella, First lithiation and charge/discharge cycles of graphite materials, investigated by electrochemical impedance spectroscopy, *J. Electroanal. Chem.*, 546 (2003) 41-50.
- [41] S.K. Meher, P. Justin, G. Ranga Rao, Nanoscale morphology dependent pseudocapacitance of NiO: Influence of intercalating anions during synthesis, *Nanoscale*, 3 (2011) 683-692.
- [42] V. Lvovich, Selected Examples of Impedance-Analysis Applications, *Impedance Spectroscopy: Applications to Electrochemical and Dielectric Phenomena*, John Wiley & Sons 2012, pp. 281-318.

- [43] H. Lee, V.S. Kumbhar, J. Lee, Y. Choi, K. Lee, Highly reversible crystal transformation of anodized porous V_2O_5 nanostructures for wide potential window high-performance supercapacitors, *Electrochim. Acta*, 334 (2020) 135618.
- [44] Y. Zhang, J. Zheng, Y. Zhao, T. Hu, Z. Gao, C. Meng, Fabrication of V_2O_5 with various morphologies for high-performance electrochemical capacitor, *Appl. Surf. Sci.*, 377 (2016) 385-393.
- [45] B. Pandit, D.P. Dubal, P. Gómez-Romero, B.B. Kale, B.R. Sankapal, V_2O_5 encapsulated MWCNTs in 2D surface architecture: Complete solid-state bendable highly stabilized energy efficient supercapacitor device, *Sci. Rep.*, 7 (2017) 43430.
- [46] J. Pan, R. Zheng, Y. Wang, X. Ye, Z. Wan, C. Jia, X. Weng, J. Xie, L. Deng, A high-performance electrochromic device assembled with hexagonal WO_3 and NiO/PB composite nanosheet electrodes towards energy storage smart window, *Sol. Energy Mater. Sol. Cells*, 207 (2020) 110337.
- [47] M. Qiu, P. Sun, L. Shen, K. Wang, S. Song, X. Yu, S. Tan, C. Zhao, W. Mai, WO_3 nanoflowers with excellent pseudo-capacitive performance and the capacitance contribution analysis, *J. Mater. Chem. A*, 4 (2016) 7266-7273.
- [48] M. Beygisangchin, S. Abdul Rashid, S. Shafie, A.R. Sadrolhosseini, H.N. Lim, Preparations, Properties, and Applications of Polyaniline and Polyaniline Thin Films—A Review, *Polymers*, 13 (2021).
- [49] S.F. Kuchena, Y. Wang, Superior Polyaniline Cathode Material with Enhanced Capacity for Ammonium Ion Storage, *ACS Appl. Energy Mater.*, 3 (2020) 11690-11698.
- [50] A.L. Dyer, A.M. Österholm, D.E. Shen, K.E. Johnson, J.R. Reynolds, Conjugated electrochromic polymers: structure-driven colour and processing control, in: R.J. Mortimer, D.R. Rosseinsky, P.M.S. Monk (Eds.) *Electrochromic Materials and Devices*, Wiley-VCH Verlag GmbH & Co. KGaA2015, pp. 113-184.
- [51] W.T. Neo, M.H. Chua, J.W. Xu, *Fundamentals of Electrochromic Materials and Devices, Electrochromic Smart Materials: Fabrication and Applications; Smart Materials Series*2018, pp. 22-50.
- [52] A. Kraft, *Electrochromism: a fascinating branch of electrochemistry*, *ChemTexts*, 5 (2018) 1.
- [53] X. Wu, Q. Wang, W. Zhang, Y. Wang, W. Chen, Preparation of all-solid-state supercapacitor integrated with energy level indicating functionality, *Synth. Met.*, 220 (2016) 494-501.

- [54] K. Xu, Q. Zhang, Z. Hao, Y. Tang, H. Wang, J. Liu, H. Yan, Integrated electrochromic supercapacitors with visual energy levels boosted by coating onto carbon nanotube conductive networks, *Sol. Energy Mater. Sol. Cells*, 206 (2020) 110330.
- [55] K. Zhou, H. Wang, J. Jiu, J. Liu, H. Yan, K. Suganuma, Polyaniline films with modified nanostructure for bifunctional flexible multicolor electrochromic and supercapacitor applications, *Chem. Eng. J.*, 345 (2018) 290-299.
- [56] K. Subramani, N. Sudhan, R. Divya, M. Sathish, All-solid-state asymmetric supercapacitors based on cobalt hexacyanoferrate-derived CoS and activated carbon, *RSC Adv.*, 7 (2017) 6648-6659.
- [57] G. Cai, P. Darmawan, M. Cui, J. Wang, J. Chen, S. Magdassi, P.S. Lee, Highly Stable Transparent Conductive Silver Grid/PEDOT:PSS Electrodes for Integrated Bifunctional Flexible Electrochromic Supercapacitors, *Adv. Energy Mater.*, 6 (2016) 1501882.
- [58] F. Azadian, A.C. Rastogi, Energy storage performance of thin film nanocrystalline vanadium oxide with fluorinated tin oxide current carrier electrode for solid-state transparent supercapacitors based on ionic liquid gel electrolyte, *Electrochim. Acta*, 330 (2020) 135339.
- [59] B. Saravanakumar, K.K. Purushothaman, G. Muralidharan, Interconnected V₂O₅ Nanoporous Network for High-Performance Supercapacitors, *ACS Appl. Mater. Interfaces*, 4 (2012) 4484-4490.
- [60] J. Guo, M. Wang, X. Diao, Z. Zhang, G. Dong, H. Yu, F. Liu, H. Wang, J. Liu, Prominent Electrochromism Achieved Using Aluminum Ion Insertion/Extraction in Amorphous WO₃ Films, *J. Phys. Chem. C*, 122 (2018) 19037-19043.
- [61] E. Hopmann, H. Li, A.Y. Elezzabi, Rechargeable Zn²⁺/Al³⁺ dual-ion electrochromic device with long life time utilizing dimethyl sulfoxide (DMSO)-nanocluster modified hydrogel electrolytes, *RSC Adv.*, 9 (2019) 32047-32057.
- [62] B. Saravanakumar, K.K. Purushothaman, G. Muralidharan, High performance supercapacitor based on carbon coated V₂O₅ nanorods, *J. Electroanal. Chem.*, 758 (2015) 111-116.
- [63] W. Zhang, H. Li, M. Al-Hussein, A.Y. Elezzabi, Electrochromic Battery Displays with Energy Retrieval Functions Using Solution-Processable Colloidal Vanadium Oxide Nanoparticles, *Adv. Optical Mater.*, 8 (2020) 1901224.
- [64] E. Umeshbabu, G. Ranga Rao, Vanadium pentoxide nanochains for high-performance electrochemical supercapacitors, *J. Colloid Interface Sci.*, 472 (2016) 210-219.

Chapter 5

Summary

and

Future perspectives

5.1. Summary

To date, electrochromic technology has significantly evolved with ample number of researches. In recent days, clubbing electrochromism with other advanced technologies has further fostered it towards various technological excellences in terms of multifunctional devices. However, there are still plenty of rooms for development in this field. Considering the impending environmental concerns, current researches are largely devoted to energy saving, alternative energies and energy storage. This thesis mainly dealt with the electrochromism in transition metal oxide nanostructures and highlighted its application in energy saving smart windows and electrochromic energy storage devices.

Three research works are put forward in this dissertation. The first project explored the synthesis of hollow microspheres of NiO with multiple self-supported shells, composed of NiO nanoparticles and later its application in electrochromic smart windows. This work also showed how the change in morphology of a material influences its electrochromic performances. For featuring the practicability of the material as an electrochromic electrode, a polymer gel electrolyte-based quasi-solid state smart window prototype was demonstrated in this work.

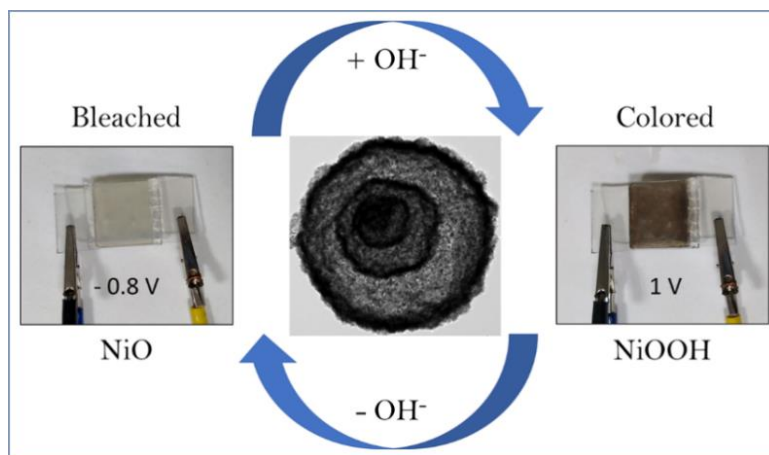


Figure 5.1: Graphical abstract for the work presented in Chapter 2

Next, carbon-embedded porous NiO was synthesized from a nickel MOF with improved charge transfer kinetics and electrochromic performances, compared to the previous work. The material was later integrated as a positive electrode in an electrochromic Zn-NiO battery, where the device's color dynamically changes with its state of charge. It consumes power only during coloration and eliminates the requirement of energy consumption during bleaching process with an energy retrieval function. The colour changes from dark brown to colourless in due course of discharging. Electrochromic smart windows with energy storage

functionalities can also be used as back-up power sources in energy efficient buildings in absence of sunlight.

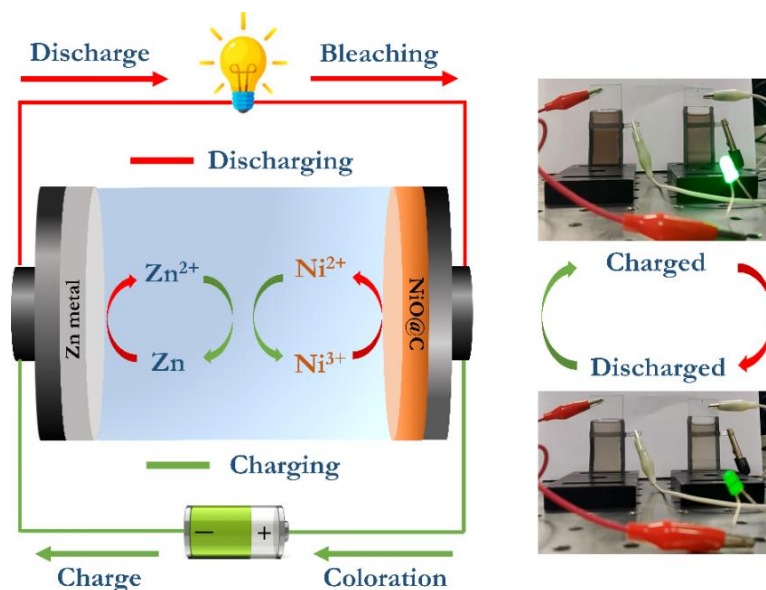


Figure 5.2: Graphical abstract for the work presented in Chapter 3

The color change of the Zn-NiO electrochromic battery was perceived to be monochromatic. But, an electrochromic energy storage device with multiple shades undoubtedly assists in better visual determination of its energy storage level. Therefore, the final section of this thesis dealt with that issue. A porous V_2O_5 material was synthesized from a vanadium MOF. As an electrochromic electrode, it demonstrated decent performance with more than one chromatic state. This V_2O_5 electrode was later used as the smart negative electrode to assemble a multicolored electrochromic asymmetric supercapacitor module with PANI as the positive electrode.

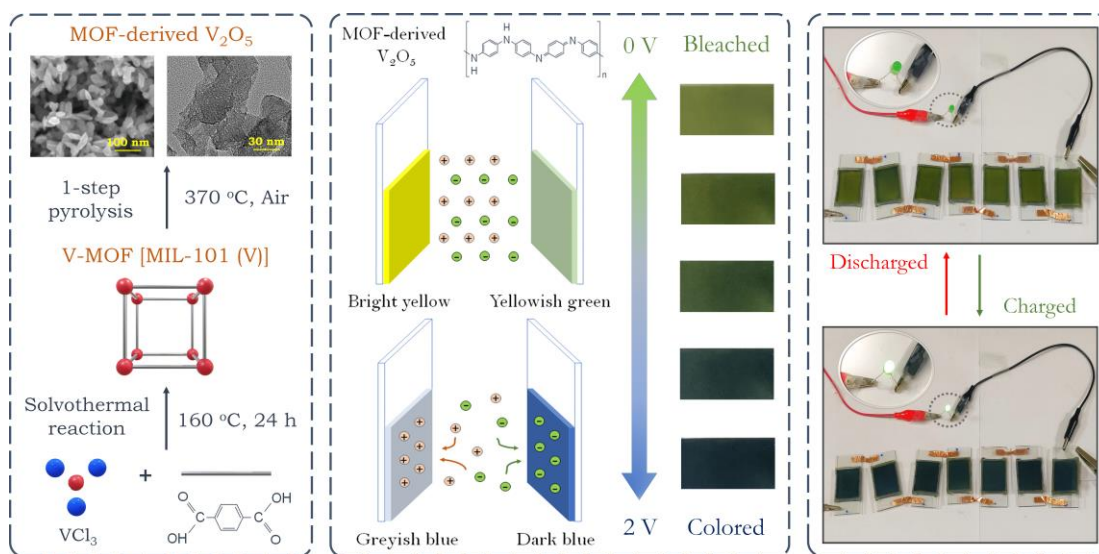


Figure 5.3: Graphical abstract for the work presented in Chapter 4

5.2. Future perspectives

Smart windows and electrochromic energy storage devices both have witnessed remarkable development in past few years and have great scopes in future technological applications. The research works performed in this thesis are confined to laboratory scale. For advancement to commercial applications, further research is required on different aspects of device engineering which often remain unnoticed due to the high-end technology requirements. At the same time, development of high performing electrochromic materials is undoubtedly important too. In the last few years, a fascinating field of dual-band electrochromism has emerged with the aid of the plasmonic colloidal oxide nanocrystals. Due to the creation of localized surface plasmon resonance absorption in the near-infrared region, plasmonic electrochromism evolves in transparent metal oxide nanocrystals. Thus, the control over both visible and near-infrared regions of the electromagnetic spectrum will play a key role in next generation smart windows.[1]

Additionally, in comparison to the commercially available lithium-ion batteries and supercapacitors, electrochromic energy storage devices are still far from significant market entry as considerable improvements are required in this field. Self-rechargeable and self-powered electrochromic energy storage devices bring new prospects in this field of futuristic smart electronic devices and energy-efficient self-sustainable smart windows.[2] Development of cost-effective and environmentally safe electrolytes and electrode materials with novel structures, rational designs and superior performances is highly needed alongside the integration of advanced technologies with electrochromics to achieve high performing multifunctional electrochromic energy storage devices.[3] Fundamental researches are extremely important for the advancement in material synthesis routes (like reversible metal electrodeposition [4]), to have the basic structural understanding of the materials, as well as to understand the electrochemistry at the electrode-electrolyte interfaces for promoting the sustainable growth of this domain.[5]

5.3. Bibliography

- [1] E.L. Runnerstrom, A. Llordés, S.D. Lounis, D.J. Milliron, Nanostructured electrochromic smart windows: traditional materials and NIR-selective plasmonic nanocrystals, *Chem. Commun.*, 50 (2014) 10555-10572.
- [2] W. Wu, M. Wang, J. Ma, Y. Cao, Y. Deng, Electrochromic Metal Oxides: Recent Progress and Prospect, *Adv. Electron. Mater.*, 4 (2018) 1800185.
- [3] Z. Wang, X. Wang, S. Cong, F. Geng, Z. Zhao, Fusing electrochromic technology with other advanced technologies: A new roadmap for future development, *Mater. Sci. Eng. R Rep.*, 140 (2020) 100524.
- [4] J. Song, J.Y. Park, K. Kim, J.-L. Lee, High-Vacuum Annealed Al-Doped ZnO Nanorods for Fast-Switching Electrochromic Windows with High-Optical Contrast and Long-Term Stability, *ACS Appl. Nano Mater.*, 5 (2022) 3946-3956.
- [5] Z. Lu, X. Zhong, X. Liu, J. Wang, X. Diao, Energy storage electrochromic devices in the era of intelligent automation, *Phys. Chem. Chem. Phys.*, 23 (2021) 14126-14145.

List of publications

- ✚ A multi-chromic supercapacitor of high coloration efficiency integrating a MOF-derived V₂O₅ electrode
Anweshi Dewan, Remya Narayanan, Muhammed Musthafa*
Nanoscale, 14, 17372-17384 (2022)
- ✚ MOF-derived carbon embedded NiO for an alkaline Zn-NiO electrochromic battery
Anweshi Dewan, Soumodip Sur, Remya Narayanan, Muhammed Musthafa*
ChemElectroChem, 9, e202200001 (2022)
- ✚ Multi-shelled NiO hollow microspheres as bifunctional materials for electrochromic smart window and non-enzymatic glucose sensor
Anweshi Dewan, Sattwick Haldar, Remya Narayanan*
J. Solid State Electrochem., 25, 821-830 (2021)
- ✚ Synthesis and optical properties of colloidal M₃Bi₂I₉ (M = Cs, Rb) perovskite nanocrystals
Jaya Pal*, Amit Bhunia, Sudip Chakraborty, Suman Manna, Shyamashis Das, *Anweshi Dewan*, Shouvik Datta* and Angshuman Nag*
J. Phys. Chem. C, 122, 19, 10643--10649 (2018)
- ✚ Complimentary effects of annealing temperature on optimal tuning of functionalized carbon-V₂O₅ hybrid nanobelts for targeted dual applications in electrochromic and supercapacitor devices
Remya Narayanan*, *Anweshi Dewan*, Debanjan Chakraborty
RSC Adv., 8, 8596–8606 (2018)

Rights and permissions

SPRINGER NATURE

Thank you for your order!

Dear Mr. Anweshi Dewan,

Thank you for placing your order through Copyright Clearance Center's RightsLink® service.

Order Summary

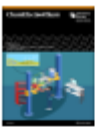
Licensee: Mr. Anweshi Dewan
Order Date: Jul 24, 2022
Order Number: 5355441254130
Publication: Journal of Solid State Electrochemistry
Title: Multi-shelled NiO hollow microspheres as bifunctional materials for electrochromic smart window and non-enzymatic glucose sensor
Type of Use: Thesis/Dissertation
Order Total: 0.00 USD

View or print complete [details](#) of your order and the publisher's terms and conditions.

Sincerely,
Copyright Clearance Center

Tel: +1-855-238-3415 / +1-978-646-2777
customerservice@copyright.com
<https://myaccount.copyright.com>

CCC RightsLink



Thank you for your order!

Dear Mr. Anweshi Dewan,

Thank you for placing your order through Copyright Clearance Center's RightsLink® service.

Order Summary

Licensee: Mr. Anweshi Dewan
Order Date: Jul 24, 2022
Order Number: 5355450276888
Publication: ChemElectroChem
Title: MCP-Derived Carbon Embedded NiO for an Alkaline Zn-NiO Electrochromic Battery
Type of Use: Dissertation/Thesis
Order Total: 0.00 USD

View or print complete [details](#) of your order and the publisher's terms and conditions.

Sincerely,
Copyright Clearance Center

Tel: +1-855-238-3415 / +1-978-646-2777
customerservice@copyright.com
<https://myaccount.copyright.com>

CCC RightsLink